UNIVERSITÀ DEGLI STUDI DI CATANIA

Dipartimento di Ingegneria Elettrica Elettronica e Informatica

Ph.D. Course in Systems Engineering (XXVI cycle)

Ph.D. Thesis

MEMRISTORS AND NETWORKS: NEW STRUCTURES FOR COMPLEXITY

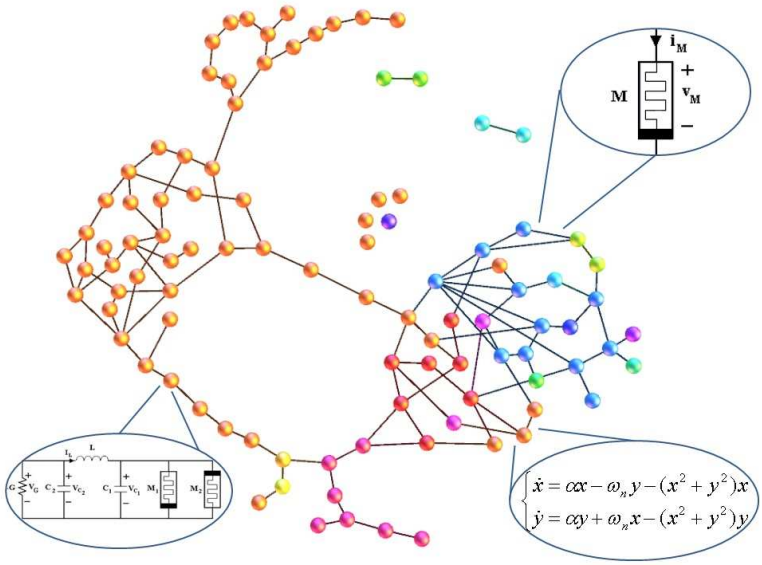

Lucia Valentina Gambuzza

TUTOR: PROF. MATTIA FRASCA

COORDINATOR: PROF. LUIGI FORTUNA

To my mom

"*...but it was only fantasy*
the wall was so high, as you can see..."

Synopsis

One of the most interesting aspects of complexity is that it occurs at different levels. It may occur at the level of interactions among the agents that compose a complex network: despite the relatively simple behavior of each single unit, the whole network may exhibit holistic collective dynamics, such self-organization, synchronization, robustness to failure, and so on; and it may occur, in the form of an aperiodic irregular behavior, at the level of a system described by a low-order set of ordinary differential equations, three, for instance, in the case of continuous-time systems. This thesis focuses on both levels of complexity.

The first part, in particular, deals with complexity at the level of a single dynamical system. The main contributions of the work summarized in this thesis refer to the use of a new electronic component for the design of chaotic circuits. This new component, the memristor, is at the same time a memory element and a nonlinear element and for this reason has been regarded in literature as an effective block to reduce the minimum number of components needed to build a chaotic circuit. The original aspect of this thesis is the focus on a realistic model of

memristor, that is a model derived starting from the analysis of the real memristor device discovered in the HP laboratories. The use of such approach introduces constraints in the design that are not considered in idealized models such as piece-wise linear ones. The main results were: i) the introduction of a configuration of two memristors in antiparallel which has been used as the fundamental block to design a gallery of autonomous and non-autonomous nonlinear circuits exhibiting a rich dynamics, including chaos; ii) the design of a hybrid circuit which takes from the characterization methodology of real memristors the idea of using a simple digital linear control circuitry which allows chaos to be observed with the driving of a single memristor.

The second part of the thesis focuses on synchronization on complex networks. In particular, the onset of a new form of synchronization, named remote synchronization, in complex networks has been investigated. Remote synchronization appears in star-like networks of coupled Stuart-Landau oscillators, where the hub node is characterized by an oscillation frequency different from that of the leaves, as a regime in which the peripheral nodes are synchronized each other but not with the hub. In this thesis we have investigated if similar conditions can be observed in more general frameworks. We have found that networks of not homogeneous nodes may display many pairs of nodes that, despite the fact that are not directly connected nor connected through chains of synchronized nodes, are phase synchronized. We have introduced measures to characterize this phenomenon and found that it is common both in scale-free and Erdos-Renyi networks. Furthermore, this is

an important mechanism to form clusters of synchronized nodes in a network. Finally, we have linked the appearance of pairs of remotely synchronized nodes to a topological condition of inhibition of direct paths or paths through chains of synchronized nodes, thus elucidating a mechanism which has lead to the definition of a series of topologies where remote synchronization is found.

Finally, we have explored the use of memristor as a synapse for complex networks. Also in this case, we have used a configuration of two HP memristors and shown that such configuration provides an adaptation rule for the links of a complex network, enabling the emergence of a set of weights leading to synchronization.

Contents

Part I

Memristors

1

The memristor

In this chapter a brief overview on memristor models will be given. The properties of the memristor, from the mathematical model introduced by L. Chua, to the device realized in the HP laboratories, will be introduced and the use of the memristor as nonlinear element in the design of chaotic circuits will be discussed.

1.1 The memristor: the theoretical postulation

First theoretically postulated in 1971 by Leon O. Chua [1], a memristor, crasis for memory-resistor, is the fourth basic circuital element. It can be defined as a dynamical resistor in which the resistance $R(w)$ is a function of the internal state variable w or, equivalently, in which there is a relationship between charge and magnetic flux linkage. The memristor fundamental equation is a generalization of the Ohm's law $v = M(q)i$, where the memristance $M(q)$, unlike constant resistances, is function of the quantity of charge that has passed through the device.

Unlike the resistor, where the voltage is proportional to the current and the $v-i$ characteristic is a straight line of slope R, in a memristor the relation is nonlinear and the $v-i$ characteristic is a curve where the slope varies point by point. The curve takes a form of an hysteresis loop pinched in the origin, in fact whenever the voltage is zero, so is the current. In this curve the same voltage can yield to two different current values.

An important property of memristors is that the $v-i$ characteristic depends on the frequency and the pinched hysteresis loop shrinks when the frequency increases. In the theoretical limit of infinity frequency, the memristor acts as a linear resistor.

The memristor is a nonlinear element with memory. For this reason, memristors are gaining an increasing interest in the scientific community for their possible applications, e.g. high–speed low–power processors or new biological models for associative memories. Due to the intrinsic nonlinear characteristic of memristive devices, it is also possible to use them in the design of new dynamical circuits able to show complex behavior, like chaos, which is the main interest of the use of memristor in this thesis.

In its seminal paper, Leon O. Chua [1] followed arguments based on the symmetry between the four fundamental circuital variables, current i, voltage v, charge q and magnetic flux φ, and the corresponding three basic circuital components, resistor, capacitor and inductor. Chua predicted the existence of a further basic element modeling a relationship $\varphi = \varphi(q)$ between flux and charge (*charge-controlled* model) or a rela-

tionship $q = q(\varphi)$ between charge and flux (*flux-controlled* model). The notable property of memristor is that, if its constitutive relationship is represented in terms of the voltage across its terminal (which is the integral of the flux) and the current (i.e., the integral of the charge), one obtains a nonlinear relationship which depends on an internal variable (the charge or the flux), i.e., it acts as a nonlinear resistor (or a nonlinear conductance) with memory. In this way the fourth basic circuital element can be defined as a dynamical resistor in which its resistance $R(w)$ is a function of the internal state variable w, that is a relation between charge and magnetic flux.

In terms of the $v - i$ relationship a memristor can be conveniently defined following [1]. This passive two–terminal circuital element is described by:

$$v = M(q)i, \text{ or } i = W(\varphi)v, \tag{1.1}$$

where v, i, q, and φ are the voltage, the current, the charge and the flux associated to the device, $M(q)$ is the memristance and $W(\varphi)$ is the memductance defined as:

$$M(q) = \frac{d\varphi(q)}{dq}, \tag{1.2}$$

and

$$W(\varphi) = \frac{dq(\varphi)}{d\varphi}. \tag{1.3}$$

Hence, the constitutive relations $\varphi(q)$ and $q(\varphi)$ define the behavior of the charge–controlled and flux–controlled memristor, respectively.

The concept of memristor was then generalized (again by Chua) in [2],introducing the class of *memristive system* defined as:

$$\begin{aligned} v_M &= R(x) i_M \\ \dot{x} &= f(x, i_M) \end{aligned} \tag{1.4}$$

where $R(x)$ is the memristance and $f(x, i_M)$ the internal state function of the memristor.

The memristive device has a state variable, w, describing the physical properties of the device in any time, and characterized by the two Eq. (1.4). In the first equation current and voltage are related through the memristance, and in the second equation the state variable varying as function of itself and the current flowing into the device. As results of this extension, any electronic circuit element whose resistance depends on the internal state of the system and the relation between current and voltage is a pinched hysteresis loop, could be modeled by the Eq. (1.4). The knowledge of the dependence of the state variable on the current or on the voltage is important to describe the dynamical behavior of the device. Following this generalization the memristor is a particular case of the memristive systems.

Furthermore, in [3], it was shown that the concept of memory device is not related only to the resistance, but it can be generalized to capacitive and inductive systems; the authors have introduced two new classes of memory devices, the *memcapacitative systems* and the *meminducitve systems*. The first class (charge-controlled memcapacitor)

is defined by a relationship between charge and voltage:

$$\begin{aligned} q(t) &= C(x, v_c, t)v_c \\ \dot{x} &= f(x, v_c, t) \end{aligned} \tag{1.5}$$

where q is the charge on the capacitor, C the memcapacitance, function of the internal state of the system, and v_c the voltage across the capacitor. In the plane $q - v_c$ the system shows a pinched hysteresis loop passing through the origin. The memcapacitor changes its behavior depending on the frequency, in fact acts as linear capacitor at high frequency, as nonlinear capacitor at low frequency.

The meminductor systems (flux-controlled) are defined by the following equations:

$$\begin{aligned} \varphi(t) &= L(x, I_l, t)I_l \\ \dot{x} &= f(x, I_l, t) \end{aligned} \tag{1.6}$$

where φ is the flux of the meminductor, L the meminductance, and I_l the current flowing in the meminductor. Also in this case, when a sinusoidal signal is applied to the terminal of the device, a pinched loop in the flux-current plane appears; increasing the frequency the memory effect decreases and the loop disappears.

1.2 The memristor: the discovery in Hewlett-Packard labs

For many years the memristor was considered just as a mere theoretical curiosity, until the first physical realization of a two–terminal memris-

tive integrated device that has been reported in the seminal paper by the researchers of HP labs [4]. After this first device based on a TiO_2 thin film, several other memristive devices based on the same principle of the TiO_2 memristor have been fabricated with different materials and techniques (see for instance [5, 6, 7, 8, 9]). In these memristors the state depends on the oxygen vacancies that, under the effect of external bias, move from one layer to the other one, changing the resistance and the state of the device.

Memristors based on other mechanisms have been also introduced. For instance, in spin-based memristive systems [10] the memristive behavior depends on the degree of freedom in the electron spin. In these devices the level of the electron spin polarization changes by the influence of an external control parameter. As result, there is a magnetic domain wall, i.e. a boundary between two states, that moves as a function of the external control parameter. The memristive behavior is found in a semiconductor/half-metal junction where a flow of only spin-up electrons may form, since spin-down electrons cannot enter the half-metal and form a cloud of spin-down electrons. Attention has been also devoted to develop spintronic memristors [11, 12]. In this type of device there are two ferromagnetic layers (one is the reference layer, the other one is the free layer). The free layer is divided in two parts magnetized with opposite directions creating a domain wall. The resistance of the device is determined by the position of the barrier between the two layers with opposite electron spin directions which in turns is controlled by the external control parameter.

The HP memristor is a TiO_2 thin film, of thickness D, doped with oxygen vacancies and sandwiched between two metal (Platinum) contacts as schematically represented in Fig. 1.1. The width of the doped region is indicated as w and changes as a function of the current injected in the device.

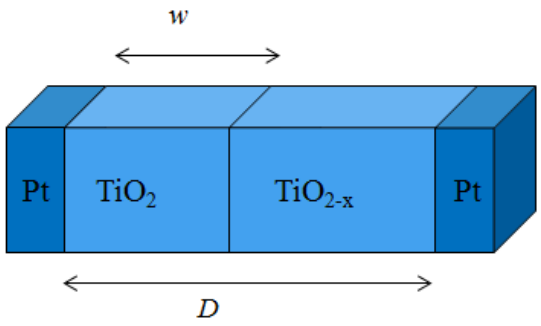

Fig. 1.1. Schematic representation of the TiO_2 memristor.

The doped region and the undoped one have different resistivity values (the doped region has a typical low value, while the undoped one an high value). When the width of the doped region is equal to the whole thickness (i.e., $w = D$), the memristor has a resistance equal to R_{ON}, while, in the opposite case, when the undoped region covers the whole thickness of the device (i.e., $w = 0$), the memristor has a resistance equal to R_{OFF}. In all the other intermediate cases, the HP memristor is modelled as the series of two resistances, one corresponding to the region with a high concentration of dopants (of value $\frac{w}{D}R_{ON}$) and the other to the region with a low concentration of dopants (of value $(1 - \frac{w}{D})R_{OFF}$). In summary, the HP memristor is modelled in terms

of a dynamical resistor whose value of resistance $R(w)$ is a function of the internal state variable w.

The width w of the doped region changes under the application of an external bias $i(t)$ in the device: when a positive current is applied, the oxygen vacancies in the doped region move towards the undoped region, in this way the boundary between the two layer moves, causing an increase of the width of the conducting layer and decreasing the resistance of the device. When a negative current is applied, the oxygen vacancies move out from the undoped region increasing the resistance of the device. When the current is turned-off the boundary between doped and undoped region stays in its new position.

The relation between voltage and current of the HP memristor is described by the following equation:

$$v(t) = \left(R_{ON} \frac{w(t)}{D} + R_{OFF}(1 - \frac{w(t)}{D}) \right) i(t) \tag{1.7}$$

The variable $w(t)$ is limited to values between zero and D and is linked to the charge q by:

$$w(t) = \eta \frac{\mu_v R_{ON}}{D} q(t) \tag{1.8}$$

or equivalently to the current i by:

$$\dot{w}(t) = \eta \frac{\mu_v R_{ON}}{D} i(t) \tag{1.9}$$

where the parameter η characterizes the polarity of the memristor, $\eta = 1$ if the doped region in memristor is expanding, $\eta = -1$ otherwise. This is known as the *linear drift model*.

However, according to what experimentally observed in the HP memristor, a few volts causes a large electric field in the nano-scale device, thus producing a high nonlinearity in the ionic-drift transport. This nonlinearity becomes more evident at the boundaries, where $w \to 0$ or $w \to D$. To include this into the model, an additional term, called window function $F(w)$, has to be inserted in the right side of the equation (1.8):

$$w(t) = \eta \frac{\mu_v R_{ON}}{D} F(\frac{w(t)}{D}) q(t) \tag{1.10}$$

or

$$\dot{w}(t) = \eta \frac{\mu_v R_{ON}}{D} F(\frac{w(t)}{D}) i(t) \tag{1.11}$$

In [4] the proposed window function depends only on the state variable and it is defined as:

$$F_S(x) = x(1-x)/D^2 \tag{1.12}$$

where $F_S(0) = 0$ and $F_S(D) = \frac{1-D}{D} \approx 0$, so that it takes into account the boundary conditions and $x = w/D$ is the normalized state variable.. When the memristor reaches one of the boundary, $x = 0$ or $x = D$, $\frac{dw}{dt} = 0$ and no external field can change the state. This window function approximates the nonlinear behavior in the active layer of the device. Joglekar and Wolf [13] proposed the following window function:

$$F_J(x, p) = 1 - (2x - 1)^{2p} \tag{1.13}$$

where p is a positive integer which controls the nonlinearity. The function $F(x)$ is equal to zero at the boundaries, and reaches its maximum value at $x = 0.5$, as it can be observed in Fig. 1.2.

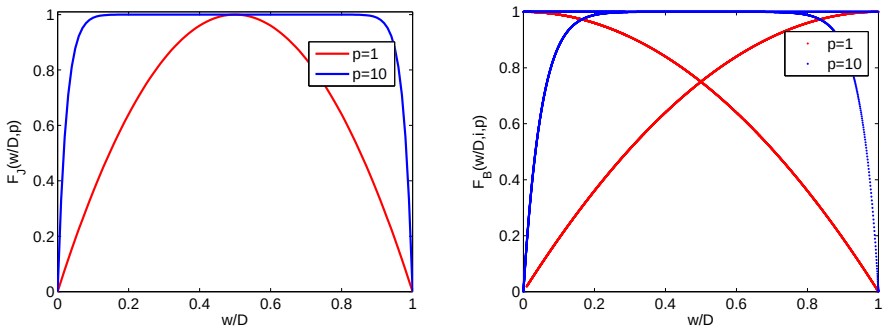

(a) (b)

Fig. 1.2. Two examples of memristor window function: (a) $F_J(x,p) = 1-(2x-1)^{2p}$ for $p = 1, 5$ and $p = 10$; (b) $F_B(x,p) = 1-(x-stp(i))^{2p}$ for $p = 1, 5$ and $p = 10$.

The problem at the terminal state remains and, when the state variable reaches one of the edges, its value remains unchanged for any external signal. To overcome this drawback, Biolek and colleagues [14] introduced another window function, displayed in Fig. 1.2(b), that also depends on the sign of the memristor current i:

$$F_B(x,i,p) = 1-(x-stp(-i))^{2p} \tag{1.14}$$

where $stp(i) = 1$ when $i >= 0$, and $stp(i) = 0$ when $i < 0$. With this window function when $x = 0$, the function $F_B(0) = 1$, and when $x = D$, the function $F_B(D) = 0$. Changing the current direction, the function immediately switches its value, $F_B(D) = 1$ and, when x decreases to 0, the function also $F_B(0) = 0$.

Where not differently specified, all the simulations in this thesis have been done by assuming a window function as in Eq. (1.14) with $p = 1$,

and the value of the technological parameters as in [4] ($D = 10nm$, $\mu_v = 10^{-14} cm^2 s^{-1} v^{-1}$, $\frac{R_{OFF}}{R_{ON}} = 100$).

The way in which a two–terminal circuital element is shown to be memristive is to test if its $v - i$ characteristic exhibits a pinched hysteresis loop [1, 4]. This can be tested by applying an external bias (a sinusoidal voltage $v(t)$) across the device terminals and monitoring the current flowing into it (Fig. 1.3). We considered as in [14] $R_{OFF}/R_{ON} = 100$ and used as in [4] normalized time units $\tau = t/t_0$ where $t_0 = D^2/\mu v_0$ and $v_0 = 1V$.

The behavior of the memristor depends on the frequency of the applied signal. If the frequency is comparable to the time scale of the memristor dynamics, the $v-i$ characteristic is a symmetrical hysteresis loop pinched at the origin as shown in Fig. 1.4(a). If the frequency of the applied voltage input is larger, the pinched hysteresis shrinks into a straight line as shown in Fig. 1.4(b). However, if the frequency is smaller with respect to the time scale of the memristor dynamics, the internal state variable w may saturate to its boundary values. If such input is applied to the HP memristor, then a characteristic which is not symmetrical with respect to the applied input appears as in Fig. 1.4(c) - 1.4(d), since for $w = 0$ the memristor shows a resistance equal to R_{OFF}, while for $w = D$ the memristor shows a resistance equal to R_{ON}. At the same time, this is the most interesting behavior for chaotic circuit design, since it represents a highly nonlinear behavior that can be exploited to generate chaotic dynamics.

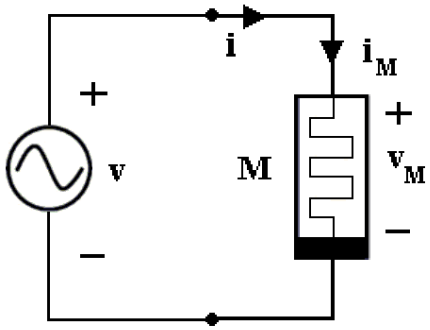

Fig. 1.3. Schematic of the circuit used to test the pinched hysteresis behavior of a single HP memristor.

1.3 Memristive device models

In the model proposed in [4] and briefly recalled in Section 1.2, the memristor properties have been attributed to the motion of oxygen vacancies activated by current flow in a TiO_2 thin film device. This model assumes that the device is constituted by two regions with different concentrations of dopants, represented by two resistors in series. The linear drift model satisfies the characteristic of a memristive system but, even in the presence of the window function, does not fully capture the real nonlinear behavior of memristor devices.

To account for this, in [5] the authors have proposed to model the relationship between current and voltage as:

$$i = w(t)^n \beta sinh(\alpha v(t)) + \chi[e^{\gamma v(t)} - 1] \tag{1.15}$$

where n is a parameter that regulates the influence of the state variable on the current, the other are fitting parameters. When $w = 1$ the device

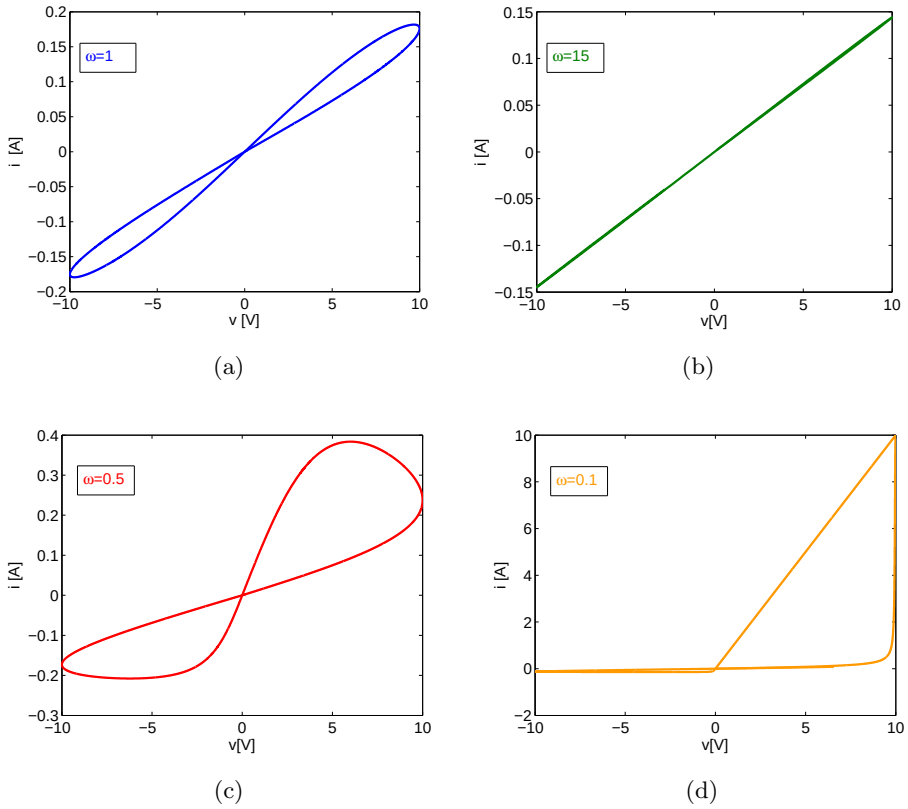

Fig. 1.4. Behavior in the $v - i$ plane of a single HP memristor subjected to a sinusoidal input of amplitude $A = 10V$ and frequency ω: (a) $\omega = 1$; (b) $\omega = 15$; (c) $\omega = 0.5$; (d) $\omega = 0.1$.

is in ON state and the main contribution to the current is given only by the first term in the Eq.(1.15). Otherwise in the OFF state, the current is due to the second term and $w = 0$.

A more detailed model has been proposed in [15] where a nonlinear and asymmetric switching behavior is adopted. A schematic view of the physical model is reported in Fig. 1.5.

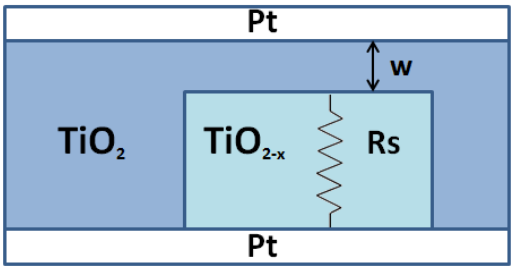

Fig. 1.5. Schematic representation of the switching model proposed in [15].

The electroforming process, that is the application of an high voltage or current producing a significant change of electronic conductivity in the TiO_2 structure, creates a conducting channel and a tunneling gap between this channel and one of the electrodes. In Fig: 1.5 w is the tunneling barrier width and R_s the resistance of the electroformed channel. The width of this gap w represents the state variable of the system, that is modulated when a voltage signal is applied to the device, inducing a motion of the oxygen vacancies. The current i that flows into the device can be modeled with Simmons tunneling equation [16]and taking into account a channel resistor, R_s, in series.

Defining as v the voltage across the whole device, v_g the voltage of the tunnel barrier, and v_R the voltage across the resistance of the channel, the relationship between the voltage v and the current i in the device is given by:

$$\begin{aligned} i &= \tfrac{j_0 A}{\Delta w^2}[\varphi_I e^{-B{\varphi_I}^{1/2}} - (\varphi_I + e v_g)e^{-B(\varphi_I + e{v_g}^{1/2}}] \\ v_g &= v - v_R = v - iR_S \end{aligned} \tag{1.16}$$

where $j_0 = e/(2\pi h)$, $\Delta w = w_2 - w_1$, $w_1 = \frac{1.2\lambda w}{\varphi_0}$, $w_2 = w_1 + w(1 - \frac{9.2\lambda}{3\varphi_0 + 4\lambda - 2e|v_g|})$. φ_I, B and λ are function of w, w_1, w_2, and φ_0 is the barrier height in electron volts.

The oxygen vacancy drift velocity is represented by the following nonlinear functions of i and w:

$$\frac{dw}{dt} = \begin{cases} f_{off} sinh(\frac{i}{ioff}) exp[-exp(\frac{w - a_{off}}{w_c} - \frac{|i|}{b}) - \frac{w}{w_c}] \; i > 0 \\ f_{on} sinh(\frac{i}{ion}) exp[-exp(-\frac{w - a_{on}}{w_c} - \frac{|i|}{b}) - \frac{w}{w_c}] \;\; i < 0 \end{cases} \tag{1.17}$$

where all the parameters in the equations are fitting parameters. Experiments on memristive devices have shown that ON and OFF switching speed are different and dependent on the polarity and on the amplitude of the applied voltage, with the OFF switching being slower. Following this model a positive voltage applied to the device produces an increase of the tunneling gap w, due to the fact that positive charged oxygen vacancies are repelled towards the conducting channel. This model provides a physical explanation for the ionic transport and the switching dynamics of the TiO_2 memristive devices.

This model is very accurate but of not simple use due to the exponential dependance of the movement of the ionized dopants and to the presence of many fitting parameters.

1.4 Memristors and flexible electronics

Recently there has been a considerable increase in the interest towards the study of chaotic circuits, thanks to the growing number of possible

fields of application in which they can be used especially for the improvement of already existing technologies which can benefit from the peculiarities of chaos and results in improved performance.

Most of the phenomena occurring in nature, but also some human behaviors, do not proceed with rhythms that are repeated, but suddenly show bifurcations, critical points turbulence and emergent behaviors. This is a phenomenon that gives rise to so-called strange attractors. In nature there are few linear phenomena, while almost all the existing systems are nonlinear. There are some common natural phenomena such as the variation of weather and the formation of clouds that are chaotic, the heartbeat is also chaotic, an healthy heart has a chaotic rhythm, whereas in a diseased heart the rhythm is more regular. These phenomena which are the subject of of chaos theory, belong to complex nonlinear dynamical systems and share some peculiar characteristics:

- sensitivity to initial conditions;
- unpredictability;
- evolution of the system characterized by many orbits that remain confined within a finite space, called attractor.

One of the most interesting aspects of the study of the dynamics of nonlinear systems is the organization that emerges spontaneously from the interaction of many elementary components. Complex systems respond to the changes of the external environment, reorganizing themselves to exhibit novel properties. Self-organization is not imposed

from the external but naturally emerges from the evolution of the system as a function of its dynamics.

Many physical systems exhibit chaotic behavior. One of the most important is the Lorenz system obtained by discretization of Navier-Stokes fluid dynamics equations [17]. Chaos appear also in electronic chaotic circuits, either as an undesired behavior or as the result of an intentional design. The first circuit exhibiting chaos was the Chua's circuit built in 1983. The implementations of integrated chaotic circuits are in a limited number, despite the significant benefits arising from the availability of integrated chaotic circuits. Until a few years ago the production of integrated circuits was based only on silicon devices. The processes used to create these ICs are not cheap. To address these issues, the tendency was to miniaturize the devices even more, so that they can integrate a larger number of transistors on a single wafer.

For about a decade, an alternative and efficient answer to the request a low-cost technology has been searched for. In this context the use of organic materials for the manufacturing of electronic devices has been recently proposed. The devices using organic semiconductors as the active element are no longer an inorganic semiconductor like silicon or gallium arsenide, but a series of molecular materials such as conjugated polymers or small molecules. The organic electronics is economically advantageous because the active substances, based on organic compounds of carbon, have important properties, including those to be flexible and easy to deposit over large areas. This can be done

at lower cost, both in liquid solution as inks or through evaporation processes.

Methods typical of the printing industry, such as screen printing or ink jet printing for the manufacture of electronic components can be therefore used for the realization of these devices. The ability to create devices through simple and low cost realization processes is one of the unique aspects of organic electronics. Another important advantage is the possibility to produce large-area devices with consequent reduction of production costs and reducing time. Despite the significant benefits of organic electronics, the science in this field still faces problems such as low mobility of charge carriers, which in turn requires a too high operating voltage, and the strong interaction of these materials with the environment (moisture, oxygen, light) which alters the basic properties.

In the context of organic electronics, it is interesting to explore the possibility to design circuits able to generate chaos. Organic chaotic circuits in fact could be applied to the production of food packaging, which will have the opportunity to include in the package, instead of labels with a bar code or in addition to the standard bar code tag, active labels that can monitor the status of the product by controlling volatile organic compounds (odors) present in the box, typical of a certain food. If over time the product were modified (so for example if the smell would change because of the deterioration of the product), the circuit would respond immediately by signaling the event [18]. The organic chaotic circuits, thanks to the characteristics of chaos, in such labels could provide a secure key to prevent product counterfeits.

Organic chaotic circuit can be used in the product identification step for product traceability. The instruments most used in practice are alphanumerical labels, bar codes and radiofrequency identification tags (RFID). Actually, products are mostly identified through bar codes which also allow to reconstruct the history of the product and its localization in order to trace the product itself.

The idea is to integrate the techniques based on traditional tools for product identification with organic circuits that show chaotic dynamics when activated by an external generator. Such circuits have intrinsic safe identificability properties, since only a copy of this circuit is able to identify it. Therefore, the information encoded in this chaotic tag can be decoded only in the presence of a circuit which can be synchronized to it. In this way, a chaotic key to make safe the identification procedure can be added. In particular, several possibilities arise for the development of chaotic circuits in organic technology and some of them are currently being explored.

As memristors in organic, or more generally in flexible, electronics have been already fabricated, the basic idea of this thesis is to exploit the nonlinearity plus memory capabilities of such devices for designing chaotic circuits in organic/flexible electronics. For this reason in the next two Chapters we will focus on electronic oscillators where the source of nonlinearity is provided by memristors.

2

Chaotic circuits based on HP memristor

In this Chapter the design of chaotic circuits based on memristors modelled with the nonlinear drift model is dealt with. This physical model, being representative of real devices, introduces constraints in the design that reduce the gap to the final implementation of the circuit. We propose a configuration based on two memristors in antiparallel as the nonlinear element for chaotic oscillators and discuss a series of nonlinear, autonomous and non-autonomous, circuits derived from existing topologies of chaotic circuits by replacing the nonlinearity with such configuration.

2.1 Introduction

The availability of memristive devices, being nonlinear elements, is useful to design circuits able to show complex dynamics like chaos. In particular, if we consider the Chua's circuit, the first example of electronic circuit able to show chaos [19], the memristor can be used as

a two–terminal nonlinear element substituting the usual nonlinearity implemented by the Chua's diode.

The same consideration hold for the canonical Chua's oscillator: in particular in [20], the Chua's diode in the canonical Chua's oscillator is replaced assuming for the memristor a piecewise-linear (PWL) function:

$$\varphi(q) = bq + \frac{1}{2}(a-b)(|q+1| - |q-1|), \tag{2.1}$$

or

$$q(\varphi) = d\varphi + \frac{1}{2}(c-d)(|\varphi+1| - |\varphi-1|). \tag{2.2}$$

If at least one of the two slopes of the constitutive relations, a and b for the charge–controlled memristor (or c and d for the flux–controlled memristor), is negative then the memristor is active. Otherwise, the memristor is passive. In this case, a negative resistance in parallel with the memristor is needed to guarantee that at least one active device is in the circuit, that is a well-known necessary condition for the onset of chaotic dynamics.

There are other examples of memristor-based chaotic circuits that assume an ideal characteristic for the memristor, in [21] it is shown that a chaotic circuit can be obtained with only three elements: a capacitor, an inductor and an active memristive system, whose memristance is defined as $R(x) = \beta(x^2 - 1)$, while in [22] a memristor with a cubic $q - \varphi$ characteristic is considered.

Concerning circuital implementations of memristor-based oscillators, several approaches based on the use of discrete-component circuits mimicking ideal memristor features have been introduced. To this aim, mutators [1], multipliers [22], micro-controllers [23] or Cellular Nonlinear Networks [24] have been used.

Most of the memristor-based oscillators, assume ideal characteristics of the memristor such as, for instance, cubic or PWL nonlinearities. Here, we introduce a different approach. We start from the model of the HP memristor ([4]) and not considered in the papers mentioned above, and introduce a gallery of chaotic circuits exploiting this device model. The HP memristor is a passive non-symmetrical element having a nonlinearity different from that more frequently investigated (often symmetrical), so that its use for chaotic circuit design is not trivial. We show that using two HP memristors in antiparallel a symmetrical nonlinearity can be recovered and suitably adapted to become the nonlinear element of canonical topologies for chaos generation. We discuss such topologies and show the chaotic attractors obtained and the bifurcation scenarios with respect to some constitutive parameters of the memristor. The analysis of the $i - v$ characteristics of the two HP memristors in antiparallel is carried out by using the so-called Biolek's window function.

2.2 The fundamental brick: two HP memristors in antiparallel

We have already shown that, when the period of the input signal, applied to the memristor, is large with respect to the time scale of the memristor dynamics, the internal state variable w may saturate to its boundary values. If such input is applied to the HP memristor, then a characteristic which is not symmetrical with respect to the applied input appears, since for $w = 0$ the memristor shows a resistance equal to R_{OFF}, while for $w = D$ the memristor shows a resistance equal to R_{ON}. At the same time, this is the regime to which we are interested to, since it represents a highly nonlinear behavior that can be exploited to generate chaotic dynamics.

We now show that a symmetrical characteristic can be recovered by connecting two memristors in antiparallel, i.e., with the two terminals shortened but with opposite polarities (Fig. 2.1). In such configuration the voltage across each memristor is equal to the voltage of the resulting two-terminal device, $v = v_{M1} = v_{M2}$, while the current is the sum of the current through each memristor $i = i_{M1} + i_{M2}$. Fig. 2.2 illustrates the behavior of this configuration (we assume as in [14] $R_{OFF}/R_{ON} = 100$ and use as in [4] normalized time units $\tau = t/t_0$ where $t_0 = D^2/\mu v_0$ and $v_0 = 1V$). A sinusoidal voltage input is applied to the HP memristor model. The amplitude $A = 10V$ and the frequency $\omega = 0.1rad/s$ are such that the state variable w oscillates between its boundary values. Fig. 2.2(a) shows the resistance of memristor 1, clearly exhibiting a

non-symmetrical behavior. Fig. 2.2(b) shows the trend of the state variables w_1 and w_2 associated to the two memristors (they oscillate at opposite phases). A symmetrical behavior is obtained in the equivalent resistance ($R_e = \left(\frac{1}{R_1(w_1)} + \frac{1}{R_2(w_2)}\right)^{-1}$), as shown in Fig. 2.2(c). The same behavior can be observed in terms of pinched hysteresis. The hysteresis curve of each of the two memristors is not symmetrical, but when they are considered together the symmetry is recovered.

Fig. 2.3 shows the pinched hysteresis at different values of ω. Fig. 2.3(a) represents the case when the input period is comparable to the time scale of the memristor dynamics. If the frequency of the applied voltage input increases, also in this case, the pinched hysteresis shrinks into a straight line as shown in Fig. 2.3(b). Figs. 2.3(c) and 2.3(d) represent the case when the input period is larger with respect to the time scale of the memristor dynamics. In particular, when $\omega = 0.1$ an highly nonlinear behavior is obtained, since the internal state variable w saturates to its boundary values (zero and D). This is clearly the most interesting case for the design of chaotic circuits. It is worth noticing that in this latter case, even if the pinched hysteresis of each memristor is not symmetrical, as shown in Fig. 1.4(d), when the two HP memristors are considered together the symmetry is recovered. This configuration will be used to design a series of nonlinear circuits able to generate chaos starting from Chua's oscillators and replacing the Chua's diode with two HP memristors in antiparallel. For this reason it will be considered as the fundamental brick for the design of chaotic circuits based on HP memristors.

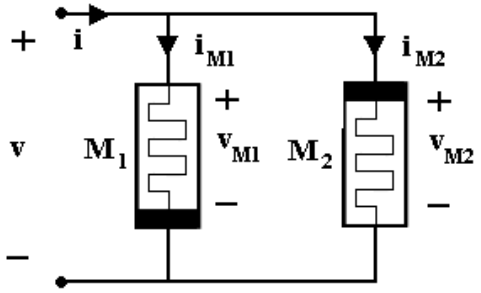

Fig. 2.1. Two memristors connected in antiparallel.

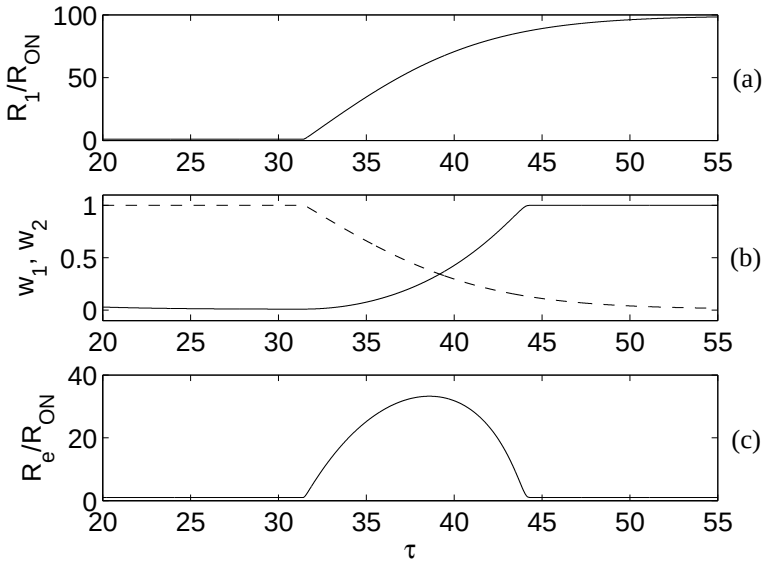

Fig. 2.2. Behavior of two memristors in antiparallel when a sinusoidal input $v(\tau) = 10sin(0.1\tau)$ is applied: (a) trend of R_1/R_{ON}; (b) trend of w_1 (dashed line) and w_2 (continuous line); (c) trend of R_e/R_{ON}.

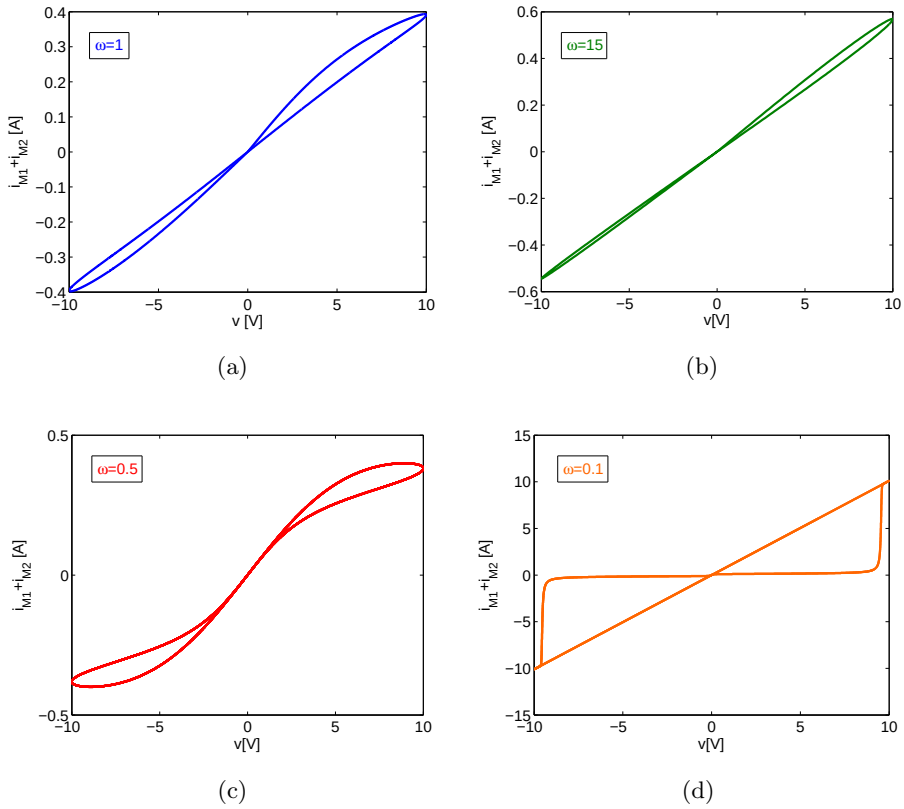

Fig. 2.3. Behavior in the $v-i$ plane of a configuration of two HP memristors in antiparallel subjected to a sinusoidal input of amplitude $A = 10V$ and frequency ω: (a) $\omega = 1$; (b) $\omega = 15$; (c) $\omega = 0.5$; (d) $\omega = 0.1$.

2.3 The HP memristor-based Chua's oscillator

In this section the chaotic oscillator, obtained starting from the Chua's oscillator by replacing the Chua's diode with the parallel between a negative conductance and the two HP memristors connected in the configuration introduced in section 2.2, is described. The circuit, shown in Fig 2.4, consists of eight elements, namely one inductor, two capaci-

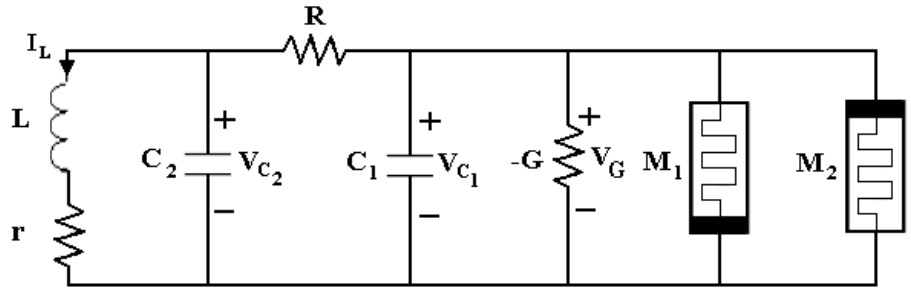

Fig. 2.4. HP memristor-based Chua's oscillator.

tors, two resistors, a negative conductance and the two HP memristors in antiparallel.

The circuit dynamics is described by the following set of differential equations:

$$\begin{cases} \frac{dv_{C_1}}{dt} = \frac{1}{C_1}(\frac{v_{C_2}-v_{C_1}}{R} + Gv_{C_1} - \frac{v_{C_1}}{R_1(w_1)} - \frac{v_{C_1}}{R_2(w_2)}) \\ \frac{dv_{C_2}}{dt} = \frac{1}{C_2}(\frac{v_{C_1}-v_{C_2}}{R} - i_L) \\ \frac{di_L}{dt} = \frac{1}{L}(v_{C_2} - ri_L) \\ \frac{dw_1}{dt} = \frac{\eta_1 \mu R_{ON}}{D} F(\frac{w_1}{D}) \frac{v_{C_1}}{R_1(w_1)} \\ \frac{dw_2}{dt} = \frac{\eta_2 \mu R_{ON}}{D} F(\frac{w_2}{D}) \frac{v_{C_1}}{R_2(w_2)} \end{cases} \tag{2.3}$$

where

$$R_i(w_i) = R_{ON}\frac{w_i}{D} + R_{OFF}(1 - \frac{w_i}{D}) \tag{2.4}$$

and $\eta_1 = -\eta_2 = 1$.

We now consider the following scaling:

$$\begin{aligned} &X = v_{C_1}/v_0,\ Y = v_{C_2}/v_0,\ Z = i_L/i_0, \\ &W_1 = w_1/D, W_2 = w_2/D, \tau = t/t_0 \end{aligned} \tag{2.5}$$

with

$$\begin{aligned} &v_0 = 1V,\ i_0 = v_0/R_{ON},\ t_0 = D^2/\mu v_0 \\ &C_0 = \tfrac{D^2}{\mu v_0 R_{ON}},\ L_0 = \tfrac{D^2 R_{ON}}{\mu v_0} \end{aligned} \tag{2.6}$$

so that Eqs. (2.3) become:

$$\begin{cases} \frac{dX}{d\tau} = \frac{C_0}{C_1}(\frac{R_{ON}}{R}Y - \frac{R_{ON}}{R}X + GR_{ON}X - \frac{X}{\hat{R}_1(W_1)} - \frac{X}{\hat{R}_2(W_2)}) \\ \frac{dY}{d\tau} = \frac{C_0}{C_2}(\frac{R_{ON}}{R}X - \frac{R_{ON}}{R}Y - Z) \\ \frac{dZ}{d\tau} = \frac{L_0}{L}(X - \frac{r}{R_{ON}}Z) \\ \frac{dW_1}{d\tau} = \eta_1 F(W_1)\frac{X}{\hat{R}_1(W_1)} \\ \frac{dW_2}{d\tau} = \eta_2 F(W_2)\frac{X}{\hat{R}_2(W_2)} \end{cases} \tag{2.7}$$

where $\hat{R}_i(W_i) = W_i + \frac{R_{OFF}}{R_{ON}}(1 - W_i)$.

We have taken into account the following typical values for the HP memristor parameters: $R_{ON} = 100\Omega$, $R_{OFF}/R_{ON} = 100$, $D = 10nm$ and $\mu = 10^{-14}cm^2s^{-1}v^{-1}$. This leads to $i_0 = 10mA$ and $t_0 = 10ms$. For such parameters, if we set $\frac{C_1}{C_0} = 0.2564$, $\frac{C_2}{C_0} = 0.75$, $\frac{L}{L_0} = 0.2$, $GR_{ON} = 0.6$, $\frac{R}{R_{ON}} = 2.7$ and $\frac{r}{R_{ON}} = 0.01$, the circuit exhibits the chaotic attractor shown in Fig. 2.5.

As it can be noticed in the rescaled Eqs. (2.7), the technological parameters of the memristor (such as R_{ON} or μ) only affect the normalization of the circuit components, with the unique exception of the technological parameter β, defined as $\beta = R_{OFF}/R_{ON}$. Hence, the dynamical behavior of the HP memristor-based Chua's oscillator is now studied with respect to this parameter. The bifurcation diagram with respect to β and the corresponding Lyapunov spectrum are reported in

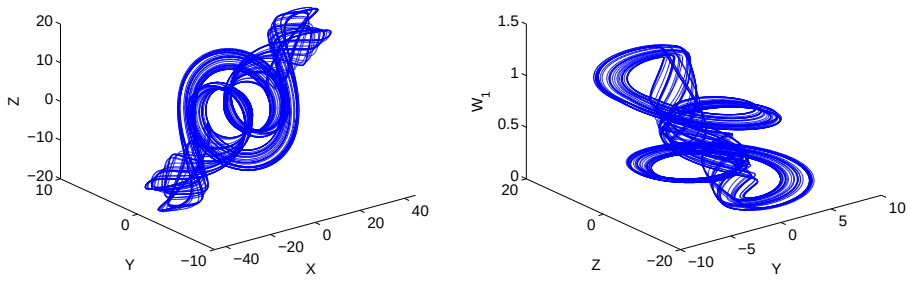

(a) (b)

Fig. 2.5. Chaotic attractor of the HP memristor-based Chua's oscillator: (a) $X - Y - Z$, and (b) $Y - Z - W_1$ phase space.

Fig. 2.6. The bifurcation diagram has been obtained by plotting the local maxima of the state variable Y. It can be observed that the chaotic behavior of the circuit is preserved for a wide range of values of β.

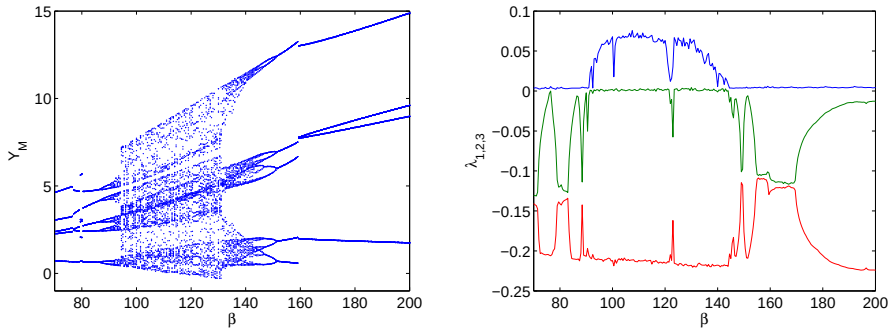

(a) (b)

Fig. 2.6. (a) Bifurcation diagram and (b) Lyapunov spectrum of the HP memristor-based Chua's oscillator with respect to β. For sake of clarity the first three Lyapunov exponents λ_1 (in blue), λ_2 (in green) and λ_3 (in red) are only reported.

The circuit exhibits a rich dynamical repertoire also when the other circuital parameters (C_1, C_2, L or G) are changed. As an example of the different dynamical behaviors generated by the circuit, we restrict our analysis to changes in the parameter $\frac{C_2}{C_0}$. The bifurcation diagram and the corresponding Lyapunov spectrum with respect to this parameter are shown in Fig. 2.7. Windows of chaotic behaviors and periodic behaviors appear in the bifurcation diagram as it is also evident from the analysis of the Lyapunov spectrum.

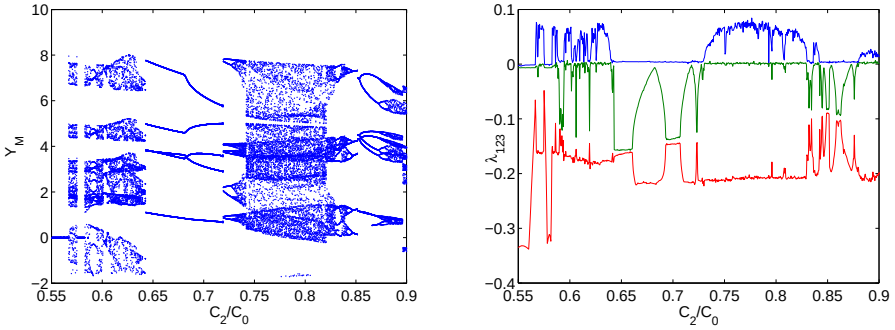

(a) (b)

Fig. 2.7. (a) Bifurcation diagram and (b) Lyapunov spectrum of the HP memristor-based Chua's oscillator with respect to $\frac{C_2}{C_0}$. For sake of clarity, the first three Lyapunov exponents λ_1 (in blue), λ_2 (in green) and λ_3 (in red) are only reported.

Following the approach described in [25], a realization of the HP memristor-based Chua's oscillator without inductor is obtained by exploiting the well-known Wien bridge configuration. The circuit, reported in Fig. 2.8, consists of a resistor, a capacitor, a Wien bridge circuit, and the nonlinear active element realized through a negative

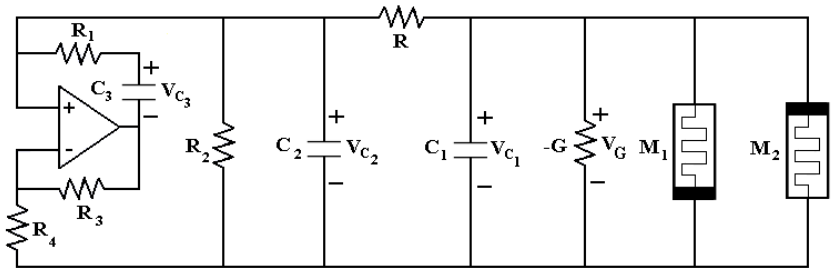

Fig. 2.8. A realization of the HP memristor-based Chua's oscillator based on Wien bridge configuration.

conductance in parallel to the two HP memristors. Applying the Kirchhoff's laws to the circuit, we obtain the following set of differential equations:

$$\begin{cases} \frac{dv_{C_1}}{dt} = \frac{1}{C_1}(\frac{v_{C_2}-v_{C_1}}{R} + Gv_{C_1} - \frac{v_{C1}}{R_1(w_1)} - \frac{v_{C1}}{R_2(w_2)}) \\ \frac{dv_{C_2}}{dt} = \frac{1}{C_2}(-\frac{v_{C_3}}{R_1} + (\frac{R_3}{R_4R_1} - \frac{1}{R2})v_{C_2} - \frac{v_{C_2}-v_{C_1}}{R}) \\ \frac{dv_{C_3}}{dt} = \frac{1}{C_3}(-\frac{v_{C_3}}{R_1} + \frac{R_3}{R_4R_1}v_{C_2}) \\ \frac{dw_1}{dt} = \frac{\eta_1\mu R_{ON}}{D}F(\frac{w_1}{D})\frac{v_{C_1}}{R_1(w_1)} \\ \frac{dw_2}{dt} = \frac{\eta_2\mu R_{ON}}{D}F(\frac{w_2}{D})\frac{v_{C_1}}{R_2(w_2)} \end{cases} \tag{2.8}$$

By applying the same scaling reported in Eqs.(2.5), Eqs. (2.8) can be scaled as follows:

$$\begin{cases} \frac{dX}{d\tau} = \frac{C_0}{C_3}(\frac{R_{ON}}{R}Y - \frac{R_{ON}}{R}X + GR_{ON}X - \frac{X}{\hat{R}_1(W_1)} - \frac{X}{\hat{R}_2(W_2)}) \\ \frac{dY}{d\tau} = \frac{C_0}{C_2}(-\frac{R_{ON}}{R_1}Z + (\frac{R_{ON}R_3}{R_4R_1} - \frac{R_{ON}}{R_2})Y - \frac{R_{ON}}{R}Y + \frac{R_{ON}}{R}X) \\ \frac{dZ}{d\tau} = \frac{C_0}{C_1}(-\frac{R_{ON}}{R_1}Z + \frac{R_{ON}R_3}{R_4R_1}Y) \\ \frac{dW_1}{d\tau} = \eta_1 F(W_1)\frac{X}{\hat{R}_1(W_1)} \\ \frac{dW_2}{d\tau} = \eta_2 F(W_2)\frac{X}{\hat{R}_2(W_2)} \end{cases} \tag{2.9}$$

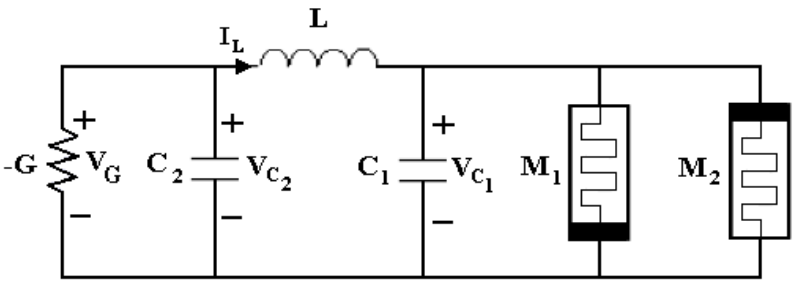

Fig. 2.9. HP memristor-based canonical Chua's oscillator.

where we have assumed that the parameters have the same value of the circuit in Fig. 2.4. The behavior of this circuit is perfectly analogous to the HP memristor-based Chua's oscillator, but the circuit avoids the use of inductors.

2.4 The HP memristor-based canonical Chua's oscillator

The second nonlinear circuit presented in this thesis is derived from the canonical Chua's oscillator by replacing the nonlinear resistor with a negative conductance in parallel to the two HP memristors. The circuit is shown in Fig. 2.9 and is governed by the following equations:

$$\begin{cases} \frac{dv_{C_1}}{dt} = \frac{1}{C_1}(i_L - \frac{v_{C_1}}{R_1(w_1)} - \frac{v_{C_1}}{R_2(w_2)}) \\ \frac{di_L}{dt} = \frac{1}{L}(v_{C_2} - v_{C_1}) \\ \frac{dv_{C_2}}{dt} = \frac{1}{C_2}(Gv_{C_2} - i_L) \\ \frac{dw_1}{dt} = \frac{\eta_1 \mu R_{ON}}{D} F(\frac{w_1}{D}) \frac{v_{C_1}}{R_1(w_1)} \\ \frac{dw_2}{dt} = \frac{\eta_2 \mu R_{ON}}{D} F(\frac{w_2}{D}) \frac{v_{C_1}}{R_2(w_2)} \end{cases} \tag{2.10}$$

By applying the scaling as in Eqs. (2.5), the following dimensionless equations are obtained:

$$\begin{cases} \frac{dX}{d\tau} = \frac{C_0}{C_1}(Y - \frac{X}{\hat{R}_1(W_1)} - \frac{X}{\hat{R}_2(W_2)}) \\ \frac{dY}{d\tau} = \frac{L_0}{L}(Z - X) \\ \frac{dZ}{d\tau} = \frac{C_0}{C_2}(-Y + GR_{ON}Z) \\ \frac{dW_1}{d\tau} = \eta_1 F(W_1) \frac{X}{\hat{R}_1(W_1)} \\ \frac{dW_2}{d\tau} = \eta_2 F(W_2) \frac{X}{\hat{R}_2(W_2)} \end{cases} \tag{2.11}$$

Also in this case, we have observed that the circuit is able to generate chaotic behavior for a wide range of the parameters. For instance, if here the parameters of the HP memristor are chosen as in the previous section and $\frac{C_1}{C_0} = 0.25$, $\frac{C_2}{C_0} = 1/3$, $\frac{L}{L_0} = 1.6$, $GR_{ON} = 0.14$, the chaotic attractor shown in Fig. 2.10 is obtained. The behavior of the circuit with respect to the technological parameter β is illustrated in Fig. 2.11. Both the bifurcation diagram and the corresponding Lyapunov spectrum clearly indicate that the onset of chaos can be observed even in presence of large variations of β from the value assumed in our simulations.

Fig. 2.12 reports an example of the behavior of the circuit with respect to one of the other circuit elements. In particular, the parameter

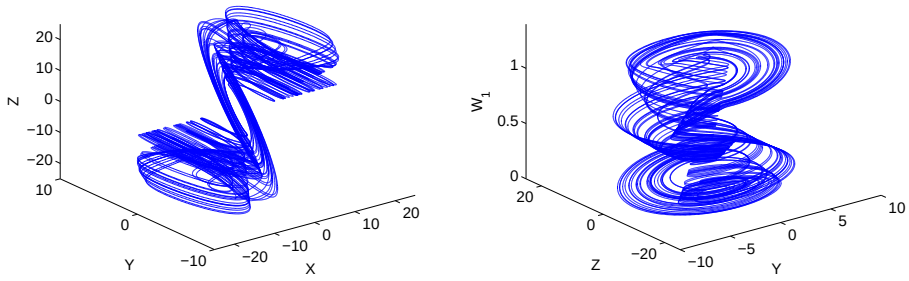

(a) (b)

Fig. 2.10. Chaotic attractor of the HP memristor-based canonical Chua's oscillator: (a) $X-Y-Z$, and (b) $Y-Z-W_1$ phase space.

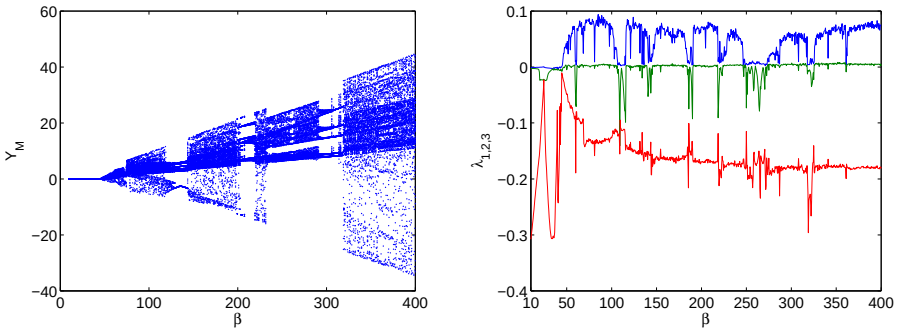

(a) (b)

Fig. 2.11. (a) Bifurcation diagram and (b) Lyapunov spectrum of the HP memristor-based canonical Chua's oscillator with respect to β. The first three Lyapunov exponents λ_1 (in blue), λ_2 (in green) and λ_3 (in red) are reported.

$\frac{C_1}{C_0}$ has been varied. The analysis of the bifurcation diagram, in accordance with the corresponding Lyapunov spectrum, allows to assess the presence of several windows of chaotic behavior and of limit cycles of different periodicity.

It is also interesting to note that the circuit shows a multistable behavior in several regions of the parameter space, which is not evident in the bifurcation diagram of Fig. 2.12, obtained for a fixed set of initial conditions. To illustrate this, we have calculated the trajectory of the system for different initial conditions. In particular, we restricted our analysis to the hyperplane with $Z(0) = 0.2$, $W_1(0) = 0.1$ and $W_2(0) = 0.9$, while we varied $X(0)$ and $Y(0)$. The result of this analysis is summarized in the map shown in Fig. 2.13, where each point of the color-coded map represents the number of different local maxima found for the state variable Y calculated at the corresponding pair of initial condition $X(0)$ and $Y(0)$. Four distinct attractors coexist for this set of parameters: the large green area indicates the chaotic attractor reported in Fig. 2.10, while the areas in the different blue tones indicate two limit cycle attractors (one of period-2 and one of period-3) and a stable equilibrium point $\begin{bmatrix} 0 & 0 & 0 & 0.09 & 0.97 \end{bmatrix}$.

2.5 The HP memristor-based hyperchaotic Chua's oscillator

The third example of HP memristor-based oscillators is derived by introducing an additional inductor, indicated as L_2, in the HP memristor-based canonical Chua's oscillator discussed in Section 2.4. L_2 is introduced in parallel to the negative conductance G, so that the circuit shown in Fig. 2.14 is obtained.

The equations governing the circuit are the following:

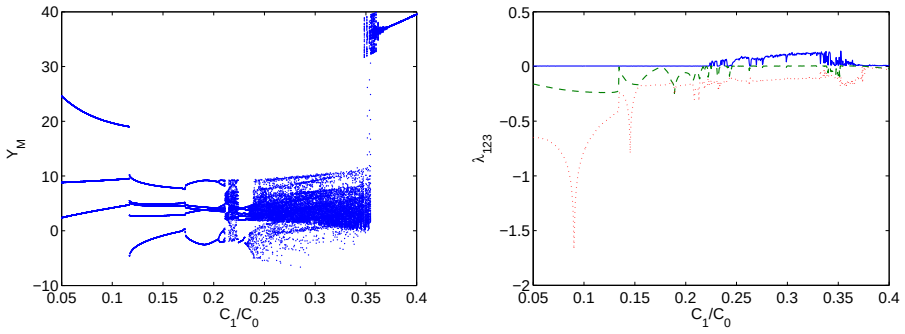

(a) (b)

Fig. 2.12. (a) Bifurcation diagram and (b) Lyapunov spectrum of the HP memristor-based canonical Chua's oscillator with respect to $\frac{C_1}{C_0}$. For sake of clarity the first three Lyapunov exponents λ_1 (in blue), λ_2 (in green) and λ_3 (in red) are only reported.

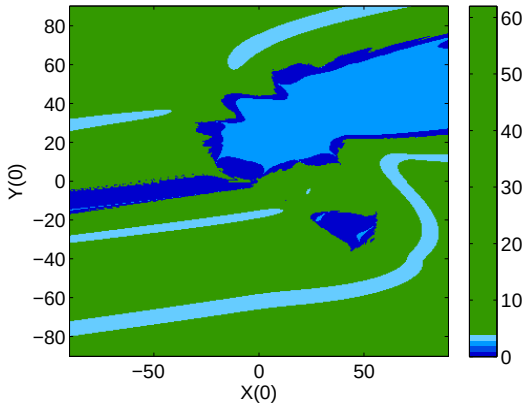

Fig. 2.13. Color-coded map of the HP memristor-based canonical Chua's circuit with respect to different initial conditions $X(0)$ and $Y(0)$ (with $Z(0) = 0.2$, $W_1(0) = 0.1$ and $W_2(0) = 0.9$), illustrating one example of multistability in the circuit.

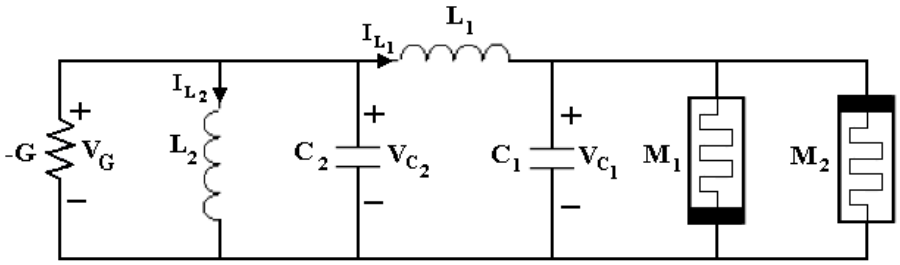

Fig. 2.14. HP memristor-based hyperchaotic Chua's oscillator.

$$\begin{cases} \frac{dv_{C_1}}{dt} = \frac{1}{C_1}(i_{L_1} - \frac{v_{C_1}}{R_1(w_1)} - \frac{v_{C_1}}{R_2(w_2)}) \\ \frac{dv_{C_2}}{dt} = \frac{1}{C_2}(Gv_{C_2} - i_{L_1} - i_{L_2}) \\ \frac{di_{L_1}}{dt} = \frac{1}{L_1}(-v_{C_1} + v_{C_2} - Ri_{L_1}) \\ \frac{di_{L_2}}{dt} = \frac{1}{L_2}v_{C_2} \\ \frac{dw_1}{dt} = \frac{\eta_1 \mu R_{ON}}{D} F(\frac{w_1}{D}) \frac{v_{C_1}}{R_1(w_1)} \\ \frac{dw_2}{dt} = \frac{\eta_2 \mu R_{ON}}{D} F(\frac{w_2}{D}) \frac{v_{C_1}}{R_2(w_2)} \end{cases} \tag{2.12}$$

Eqs. (2.12) can be scaled according to the scaling reported in Eqs.(2.5), with the additional dimensionless variable $\Omega = i_{L_2}/i_0$, as follows:

$$\begin{cases} \frac{dX}{d\tau} = \frac{C_0}{C_1}(Z - \frac{X}{\hat{R}_1(W_1)} - \frac{X}{\hat{R}_2(W_2)}) \\ \frac{dY}{d\tau} = \frac{C_0}{C_2}(GR_{ON}Y - Z - \Omega) \\ \frac{dZ}{d\tau} = \frac{L_0}{L_1}(-X + Y - \frac{R}{R_{ON}}Z) \\ \frac{d\Omega}{d\tau} = \frac{L_0}{L_2}Y \\ \frac{dW_1}{d\tau} = \eta_1 F(W_1) \frac{X}{\hat{R}_1(W_1)} \\ \frac{dW_2}{d\tau} = \eta_2 F(W_2) \frac{X}{\hat{R}_2(W_2)} \end{cases} \tag{2.13}$$

We notice that system (2.12) is able to show a transition from torus to chaos and, then, to hyperchaos when the bifurcation parameter is $\frac{L_2}{L_0}$. In fact, for the parameter values reported in Fig. 2.15, different attractors can be observed for increasing values of $\frac{L_2}{L_0}$: a torus (Figs. 2.15(a) and 2.15(b)); a chaotic attractor (Fig. 2.15(c)) and an hyperchaotic attractor (2.15(d)). The complete scenario with respect to changes in the parameter $\frac{L_2}{L_0}$ is illustrated in Fig. 2.16, which allows to detect the transition from torus to chaos occurring approximately at $\frac{L_2}{L_0} \simeq 1.9$ and that from chaos to hyperchaos at $\frac{L_2}{L_0} \simeq 3.2$.

The analysis of the behavior of the system when the technological parameter β is varied has been carried out by considering the circuit in the hyperchaotic region (i.e. $\frac{L_2}{L_0} = 3.6$). The bifurcation diagram and the Lyapunov spectrum shown in Fig. 2.17 allow to conclude that the hyperchaos can be obtained in the interval $\beta \in [88 \div 194]$, whereas outside this interval either chaos or periodic behavior appears.

2.6 The driven HP memristor based chaotic circuit

The circuit proposed by Murali, Lakshmanan and Chua [26], in the following referred to as the MLC circuit, is a dissipative non-autonomous circuit, made by an inductor, a capacitor, a resistor and a Chua's diode. In this circuit the nonlinearity is modeled with a three-segment characteristic. The circuit is driven by an external sinusoidal signal of amplitude A and frequency ω. By varying the amplitude of the forcing signal, the circuit exhibits a variety of dynamical behaviors, from limit cycle

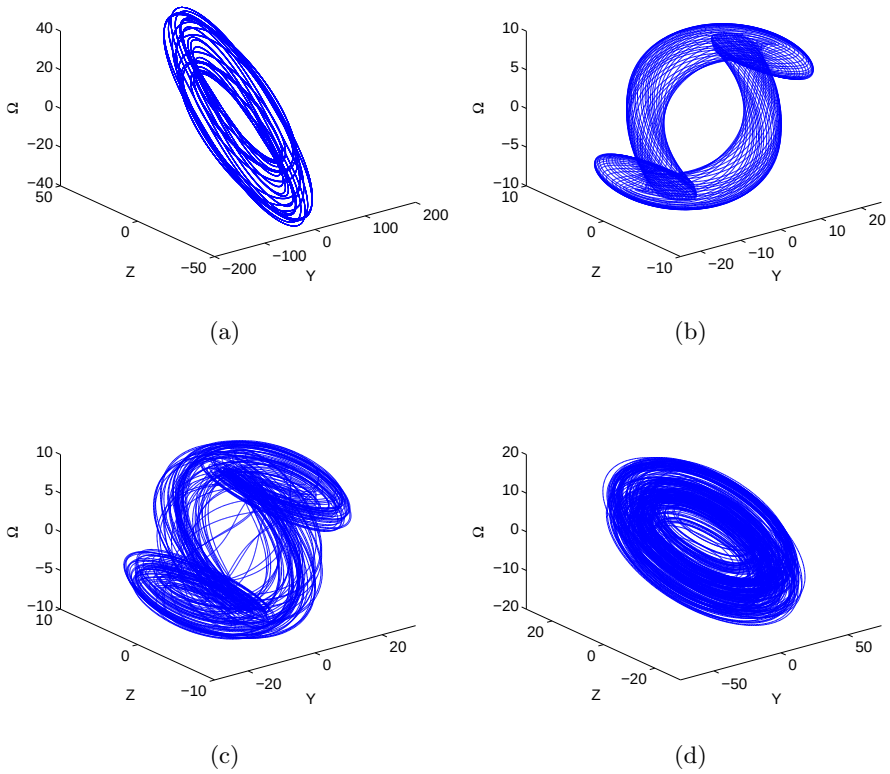

Fig. 2.15. Attractors of the HP memristor-based hyperchaotic Chua's oscillator in the $Y - Z - \Omega$ phase space. Parameter values are $\frac{C_1}{C_0} = 0.25$, $\frac{C_2}{C_0} = 1/3$, $\frac{L_1}{L_0} = 1.6$, $GR_{ON} = 0.192$, and (a) $\frac{L_2}{L_0} = 1.3$ (torus), (b) $\frac{L_2}{L_0} = 2.8$ (torus), (c) $\frac{L_2}{L_0} = 3.2$ (chaos), and (d) $\frac{L_2}{L_0} = 3.6$ (hyperchaos).

to chaotic attractors. A memristive MLC circuit built by substituting the Chua's diode with a PWL flux controlled memristor has been proposed in [27] and, recently, this system has been modeled as a piecewise smooth system of second order with two discontinuous boundaries and deeply numerically studied by Ishaq Ahamed and Lakshmanan [28], who have shown that it exhibits a wide range of chaotic behaviors in-

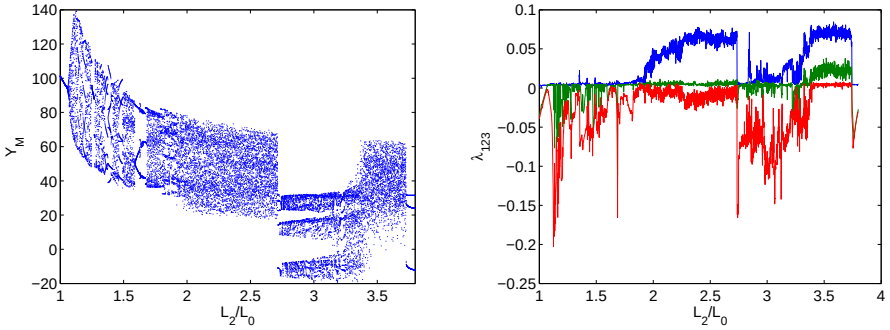

(a) (b)

Fig. 2.16. (a) Bifurcation diagram and (b) Lyapunov spectrum with respect to $\frac{L_2}{L_0}$. For sake of clarity the first three Lyapunov exponents λ_1 (in blue), λ_2 (in green) and λ_3 (in red) are only reported.

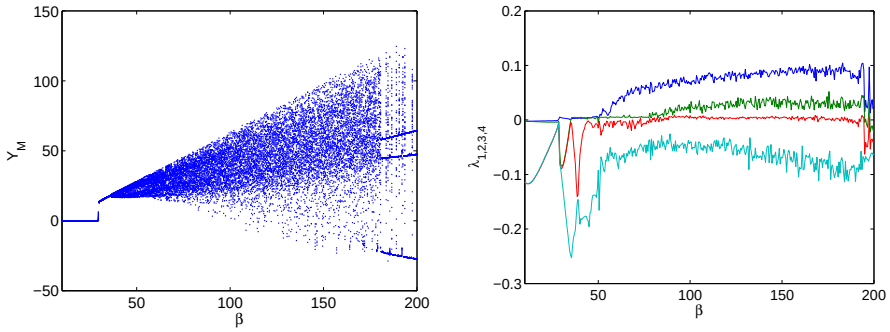

(a) (b)

Fig. 2.17. (a) Bifurcation diagram and (b) Lyapunov spectrum of the HP memristor-based hyperchaotic canonical Chua's oscillator with respect to β. For sake of clarity the first four Lyapunov exponents λ_1 (in blue), λ_2 (in green), λ_3 (in red) and λ_4 (in cyan) are only reported.

cluding transient hyperchaos and hyperchaotic beats. In this work we want to realize a non-autonomous chaotic circuit using a different model for the memristor, that is, a model adopted to mimic the behavior of the real memristor realized in the HP laboratories.

Starting from the MLC topology, we show how a new driven memristive chaotic circuit can be obtained by replacing the Chua's diode with our fundamental brick in parallel with a negative resistor. The proposed chaotic circuit is shown in Fig. 2.18.

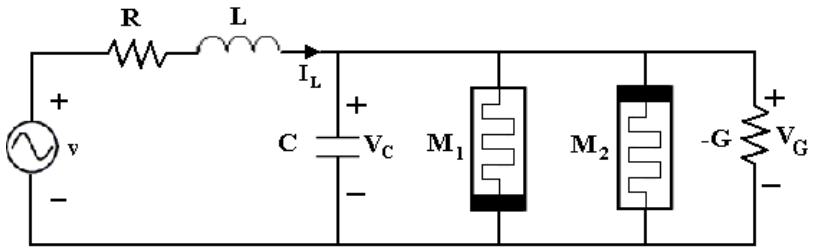

Fig. 2.18. The non-autonomous memristive chaotic circuit.

The circuit dynamics is described by the following set of differential equations:

$$\begin{cases} \frac{dv_C}{dt} = \frac{1}{C}(i_L - \frac{v_C}{R_1(w_1)} - \frac{v_C}{R_2(w_2)} + Gv_C) \\ \frac{di_L}{dt} = \frac{1}{L}(-ri_L - v_C + A\sin\omega t) \\ \frac{dw_1}{dt} = \frac{\eta_1 \mu R_{ON}}{D} F(\frac{w_1}{D}) \frac{v_C}{R_1(w_1)} \\ \frac{dw_2}{dt} = \frac{\eta_2 \mu R_{ON}}{D} F(\frac{w_2}{D}) \frac{v_C}{R_2(w_2)} \end{cases} \tag{2.14}$$

where A and ω are the amplitude and the frequency of the external signal.

A dimensionless form of Eqs. (2.14) is derived by considering the same scaling proposed for the previous circuits:

$$\begin{cases} \frac{dX}{d\tau} = \frac{C_0}{C}(Y - \frac{X}{\hat{R}_1(W_1)} - \frac{X}{\hat{R}_2(W_2)} + GR_{ON}X) \\ \frac{dY}{d\tau}\frac{L_0}{L}(-\frac{R}{R_{ON}}Y - X + A\sin\omega t) \\ \frac{dW_1}{d\tau} = \eta_1 F(W_1)\frac{X}{\hat{R}_1(W_1)} \\ \frac{dW_2}{d\tau} = \eta_2 F(W_2)\frac{X}{\hat{R}_2(W_2)} \end{cases} \tag{2.15}$$

Eqs. (2.15) have been widely investigated through numerical simulations with different values of the parameters. Chaos is obtained for different sets of parameters. Two examples of chaotic attractors are reported in Fig. 2.19, showing the projection of the attractors on the $X-Y$ plane, obtained fixing the following set of parameters: $\frac{C}{C_0} = 0.8$, $\frac{L}{L_0} = 0.44$, $GR_{ON} = 0.7$, $\frac{R}{R_{ON}} = 1.8$, and changing the value of the amplitude A and of the frequency ω of the input signal.

A more comprehensive picture of the behavior of the circuit as a function of the parameters of the input signal is shown in Fig. 2.20. Each point of the bifurcation map is a color coded representation of the number of different local maxima for the state variable X corresponding to a pair of values (A, ω). The map allows to visualize periodic behavior along with their periodicity and chaotic behavior which corresponds to points with a high number of different local maxima. In the map, colors towards red correspond to higher values of this number, thus coding for chaotic behavior. Simulations have been performed by considering fixed initial conditions $(X(0) = 0.1, Y(0) = 0.4, W_1(0) = 0.1, W_2(0) = 0.2)$ for each pair of values (A, ω).

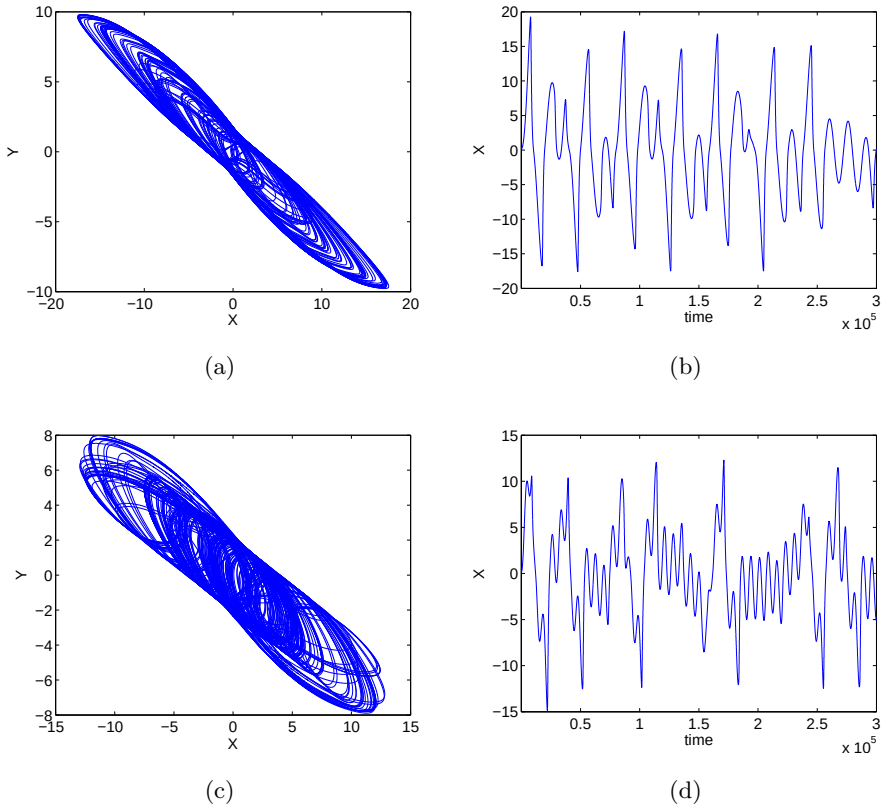

Fig. 2.19. Chaotic behavior of the non-autonomous memristive circuit driven by a sinusoidal signal with different parameters: (a-b) $\omega = 0.4, A = 2.4$,(c-d) $\omega = 0.86, A = 3.3$. (a,c) Projection of the attractor on the $X - Y$ plane. (b,d) Trend of the state variable $X(t)$. The other parameters of the circuit are fixed to $\frac{C}{C_0} = 0.8$, $\frac{L}{L_0} = 0.44$, $GR_{ON} = 0.7$, $\frac{R}{R_{ON}} = 1.8$.

Different windows of chaotic behaviors appears as one of the parameters (either A or ω) is fixed and the other is changed. To better illustrate an example of this, we considered a section of the map obtained for $\omega = 0.54$ and reported in Fig. 2.21 the bifurcation diagram

with respect to the parameter A. Windows of chaotic behaviors alternated to windows of periodic behaviors can be observed.

We also carried out an analysis of the behavior of the circuit when the other parameters (C, L, G, R) are changed. From the bifurcation diagrams with respect to these parameters, we found that different chaotic regions can be obtained, eventually by tuning the values of the amplitude and frequency of the input signal.

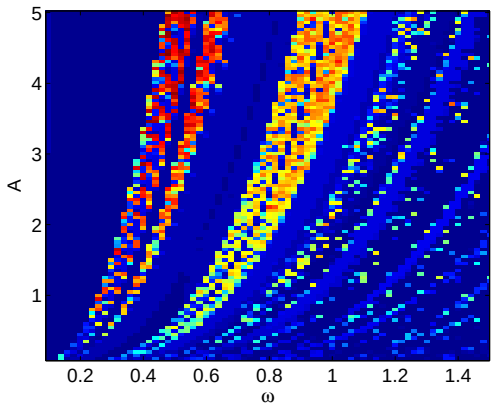

Fig. 2.20. Color-coded map of the driven memristive circuit with respect to the two parameters A and ω.

In this Chapter, we have considered the problem of designing memristor-based chaotic circuits under the assumption that the dynamics of the memristor is given by the physical model introduced in [4]. This model has been successfully used to capture the characteristics of the TiO_2 memristor fabricated in the HP laboratories, but is quite different from other ideal curves often used in memristor-based oscillators. We demonstrated that, if two such memristors are used in an

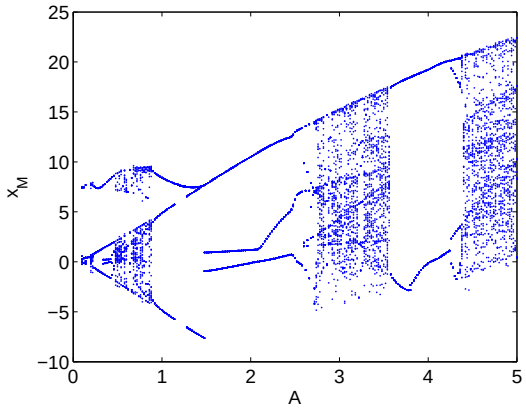

Fig. 2.21. Bifurcation diagram with respect to the amplitude A of the applied input signal.

antiparallel configuration, a symmetrical nonlinearity can be obtained and suitably used in chaotic circuit topologies such as the Chua's oscillator and the canonical Chua's oscillator.

We presented a gallery of nonlinear circuits derived from Chua's oscillators, including the MLC circuit, by replacing Chua's diodes with two HP memristors in antiparallel.

All the topologies investigated have a rich dynamic behavior as shown by the examples of attractors reported and by the numerical bifurcation diagrams and maps presented. Furthermore, an important analysis has been carried out with respect to one constitutive parameter of the memristor, β, in view of implementations based on real devices which may have parameters different from process to process. The conclusion is that very often the chaotic behavior is preserved when this parameter is varied. The results also demonstrate that the topologies investigated are paradigmatic not only in the sense that they can be

used to generate a wide spectrum of chaotic attractors and nonlinear behaviors, but also because the Chua's diode can be easily substituted by physical models of real devices.

3

Experimental characterization of memristors

The memristor performance is influenced by the fabrication technique and by the materials used, for the electrodes and the switching layer, both important to create a cost-effective device. For this reason new materials and techniques for memristor are currently explored. In this chapter the steps process in the fabrication of the memristor, and the characterization of the devices, will be discussed.

3.1 Introduction

The typical memristor has a simple structure, consisting of a switching layer interposed between two electrodes. The important characteristic of the device is the hysteretic behavior that has been attributed to the movement of the oxygen vacancies.

After the first physical realization of the memristor in HP labs, the titanium dioxide, TiO_2 has become the most used switching material for the fabrication of the memristors. Due to the variety of applications

and to the great interest raised by these new generation devices, other materials and methods for its fabrication have been explored.

Currently, there are few known methods for the fabrication of the memristor. The most widely used are the nano-imprint lithography (NIL) and atomic layer deposition (ALD), both of these processes require annealing step at high temperature, and are very expensive. Recently new methods, typical of the printing industry, such as screen printing or ink-jet printing, have been investigated for the realization of these devices. In the memristive device proposed in [5] the platinum electrodes were deposited by electron-beam evaporation at room temperature and the TiO_2 films were fabricated either by sputter deposition or atomic layer deposition (ALD) methods.

In [29] the fabrication of memristor device ($Ag/TiO_2/Cu$) is reported, the electrodes, bottom and top, and the active layer, were patterned using the electrohydrodynamic (EHD) printing technique. EHD jet printing is a method of creates patterns directly to the surface of a substrate without lithography, using electric field energy to eject the liquid from the nozzle.

A breakthrough in the memristors manufacturing was the fabrication of a device by spinning a titanium isopropoxide solution on the flexible plastic substrate [30]. This process is less expensive, in fact it requires no annealing to form the active layer and the deposition of the electrodes is made by thermal evaporation through shadow mask. Choi et al. in [31] proposed the fabrication of memristive device with a zinc oxide layer between two silver electrodes, using EHD printing

technology for electrodes deposition and spin coating for the active layer.

Other switching materials have been used as active layer for the memristors. For example tantalum oxide TaO_x memristors have demonstrated superior endurance with respect to other nanoscale devices in terms of write/erase switching cycles and high switching speed [32]. Different behaviors have been obtained also by changing the thickness or the materials for the electrodes fabrication, for example by using silver, aluminium or copper instead of platinum used in the HP memristor [33], or by using glass and ITO-glass as substrate for the device [34].

In this chapter the results of the characterization of two different types of memristor will be presented. The first device is a printed memristor, that has been realized within the framework of the FP7 APOSTILLE project. The second memristor is a drop-coated $Al - TiO_2 - Al$ memristor realized at University of West England, Bristol.

3.2 Printed memristors

The aim of this Section is to illustrate the study and the issues related to the realization of an organic memristive device with a printed technology, in particular the results obtained in collaboration with the Faculty of Technical Sciences (FTS) of Novi Sad, Serbia.

Initial attempts were performed in order to analyze the suitable substrates, materials and the methods for the characterization of the mem-

ristive device. Three different types of substrate have been analyzed: glass, ITO-glass and Kapton foil, cleaned by absolute ethanol. For the electrodes the silver ink, ink-jet printed by using a piezoelectric, drop on demand, ink-jet printer, has been used. The substrate used for the first experiments was a square of Kapton with a thickness of $50\mu m$. Deposition and patterning were performed with ink-jet Fujifilm Dimatix DMP 3000 (Fig. 3.1(a)), a fluid deposition system for printing different functional fluids. A cartridge of 16 nozzle printhead with a capacity of $1.5mL$ has been used. The printhead and the substrate were placed on the platen and, after that, the software initialization was performed. By a pattern editor the user can create or modify the drop pattern for printing. In our case simple patterns were created, usually square or rectangular patterns of different dimensions.

Before each printing session, depending on the result of the drop watcher testing (Fig. 3.1(b)), some cleaning cycles were run, for example purge cycle, to force air out of the fluid path and to clear several clogged nozzles, blot cycle, to remove excess fluid from the nozzles plate bringing an absorbent medium in close proximity of the nozzles plate, or a flush cycle, similar to the purge but with longer duration. The substrate temperature was maintained constant during the ink-jet printing process resulting in better surface properties and film uniformity. Ink-jetting conditions were optimized to obtain a highly conductive layer by controlling the waveform voltage, the cartridge temperature, the ink drop velocity and the fire frequency considering silver ink properties. The drop formation characteristics of the ink were studied by means

of built-in stroboscopic camera and interaction with substrate was observed by an optical microscope. During the preliminary testing period the optimal printing conditions were defined. With the drop watcher camera system the users can view directly the jetting nozzles, in particular the jetting of the fluid. In this way the users can turn off the blocked nozzles, the jetting of the fluid is controlled by adjusting the voltage of the single nozzle (deforming the piezoelectric actuator) in order to change the drop velocity.

The drop watcher also allows to have images with drops frozen in flight, so that the voltage amplitude, firing frequency and waveforms may be selected to optimize the printing quality. Meniscus pressure control, the low level vacuum which is applied to the ink reservoir to prevent ink from flowing out of the cartridge nozzle, could also be changed depending on the properties of the used ink. The voltage waveform can be changed by the user by setting some parameters such as the slew rate, the pulse amplitude or the pulse duration to reach the best performance.

The number of activated nozzles influences the duration of the printing process. The duration of the printing process is also influenced by the position and the form of the pattern to be printed, because the printhead moves only in vertical direction during printing, so vertically lines would be printed more rapidly and more accurately than horizontal ones.

A SunTronic U5603 ink, which has a silver content of $20wt\%$, was used. This ink is especially designed for piezoelectric ink-jet print-

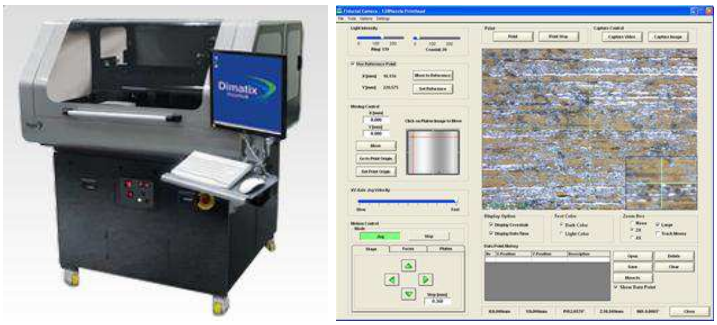

(a) (b)

Fig. 3.1. (a) The ink-jet Fujifilm Dimatix DMP 3000, and (b) an image from the drop watcher .

ing. The average diameter of the silver nanoparticles is approximately $20nm$. The silver ink were loaded into a syringe and after that the cartridge was filled, without filtering. The silver ink was printed with a drop velocity of about $7m/s$ and a drop spacing (from center to center) of $25\mu m$. These two parameters determine thickness and width of the silver electrodes. After the gate electrode was printed, the substrate was annealed at 200°C for 30 min in a convection oven. The material used for the fabrication of the active layer of the memristor is titanium dioxide. Titanium dioxide (TiO_2) is a semiconductor, and in its pure state it is highly resistive. The Degussa $P25$ titania is bought in form of nanopowder. From these powders there is not yet standard technique to create an ink suitable for Dimatix printing. Aqueous TiO_2 colloid prepared by the hydrolysis of titanium butoxide was used. A colloid containing $60g/L$ TiO_2 solid was obtained. The TiO_2 colloidal ink was

finally formed by dissolving 1.8%(w/w) of carbowax into the above TiO_2 colloid [35].

An important parameter that must be selected is the concentration of the TiO_2 ink. A too high TiO_2 concentration blocks the printer nozzle easily and may lead to the aggregation of TiO_2 nanoparticles. The realized ink was then tested and the distribution of the particle size was measured.

A major problem of the TiO_2 powders is the big size of the particles. The presence of the big particles may cause two problems: they can clog up the nozzles, because these particles don't pass through the nozzles; even not blocked nozzles act as a filter for the big particles, thus resulting in an ink with a lower real concentration. The problem can be resolved using a filter before filling the cartridge. Suspensions containing different volumes of titanium dioxide powder dispersed in distilled water were prepared, only the one containing a $60g/L$ of TiO_2 was suitable for printing. During the first printing of titanium dioxide an ink with too low concentration was produced, the printed region showed that the particles are not well dissolved in the solution. Printing was repeated up to 4 times to obtain different thicknesses of the resulting TiO_2 layers. The TiO_2 ink has a pH equal to 7; after a week the same ink previously analyzed was more stable.

The titanium dioxide layer after deposition was heated in vacuum at temperature of 300°C, with a pressure of $1.2mbar$ for an hour. This process could create a layer with a different concentration of oxygen vacancy. After this process the TiO_2 layer became brown. Another layer

of TiO_2 was then printed on top of the previous one. The device was let about 30 minutes to oxygen in air. The second silver electrode was then deposited on the titanium layer and heated following the same procedure of the first electrode.

Different devices were created with the same procedure, by changing the area of the electrodes or the time and the temperature of the heating process. The characterization of these devices have shown no memristive properties, due to the fact that the active layer was probably formed without the desired gradient of oxygen vacancy. To overcome the problem occurred in the creation of the active layer the final device was fabricated at LTP/EPFL, where the TiO_2 was heated under controlled conditions.

The memristor consists of three layers as shown in Fig. 3.2: a substrate (ITO glass), an active layer (thin TiO_2 film) and a top silver electrode.

Memristors have been fabricated using the Fujifilm Dimatix DMP 3000 ink-jet printer on commercial indium tin oxide coated glass substrate (703184 Sigma-Aldrich) with surface resistivity of 30-60 Ω/sq. For the active layer a TiO_2 ink is used, synthesized at LTP/EPFL labs. The layer of TiO_2 ink was deposited with printing frequency of $1kHz$, piezoelement actuation amplitude of $26V$ and drop spacing resolution of $20\mu m$, with the Fujifilm Dimatix DMP 3000 ink-jet printer at room temperature. Reduced layer containing oxygen vacancies was created by heating TiO_2 layer in nitrogen atmosphere for $6h$ with maximum temperature of $200°C$. Afterwards top Ag electrode (SunTronic U5603

ink) was printed with $25\mu m$ drop spacing resolution and platen temperature of $60°C$ in order to avoid unwanted spreading of silver layer and sintered for 45min at $200°C$ for degradation of organic coating over silver nanoparticles. A detailed discussion on the device fabrication and physical characterization is reported in [36] [37].

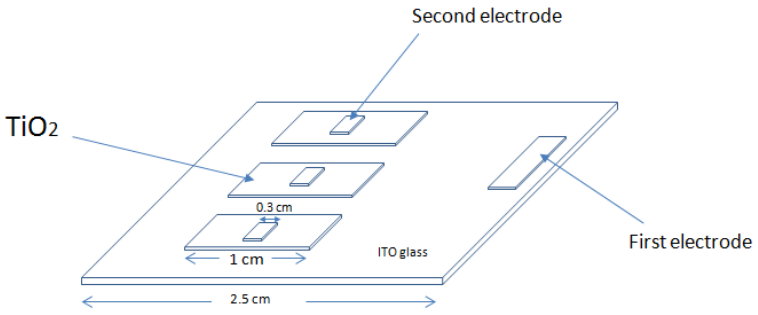

Fig. 3.2. Scheme of the TiO_2 printed memristor.

3.3 Drop-coated memristor

The second type of memristive device was realized at the University of the West of England, Bristol, in the group of Prof. Adamatzky and Dr. Gale, and the details of the fabrication process are reported in [33]. The memristor has a structure of $Al - TiO_2 - Al$, the sol-gel preparation is based on [30], and the aluminium electrodes were sputter-coated on PET substrate.

Despite other more expensive techniques for the fabrication of the active layer, the drop coated memristor was created with simple steps,

and without the forming step. In fact, the drop coated memristor naturally has a region with oxygen vacancies.

The area of the resulting device is $16mm^2$, and the electrodes of width of $4mm$ are crossed at $90°C$ each other. The top and bottom electrodes were realized by sputtering aluminium on plastic substrate via a mask; the sol-gel solution was spun at $33r/s$ for $60s$ and left for an hour to hydrolyze, before the deposition of the second electrode.

Three different types of memristor have been realized, by changing the material used for the electrodes: in particular those with bottom and top electrodes made with gold, those with the bottom electrode of aluminium and the top made of gold, and those with aluminium for both electrodes. The memristors have been labeled as R series if were left in clean room to hydrolyze, V series if they were put in vacuum, D series if were hydrolyzed under vacuum and the size of the top electrode is varied from $1mm$ to $5mm$.

The memristors with gold electrodes, instead of aluminium, have shown ohmic low resistance, the mixed one, when gold is the anode or when aluminium is the anode. In both cases they have shown bad memristive properties. So that the aluminium electrodes are important for the memristive behavior, also in terms of repeatability and stability of the memristive behavior. All the memristor devices can be grouped based on their behavior and on their current range, into two groups, type A or curved, and type B or triangular $i - v$ profiles.

In the following Section the characterization of the two types of memristor, the printed memristor and the drop coated memristor with aluminium electrodes is discussed.

3.4 Experimental characterization

The characterization of the memristive devices has been performed in two different ways, by measuring the current with the Keithley 2602 sourcemeter, or by using the circuital scheme reported in Fig. 3.3.

For the measurement of the $v - i$ characteristic of the device with the circuital scheme in Fig. 3.3, a sine waveform with low frequency, in the order of magnitude of Hz, and an amplitude of $1V$ was applied to the device; the value of the resistor used for the measurement of the current flowing through the device was varied from 1Ω to $1k\Omega$.

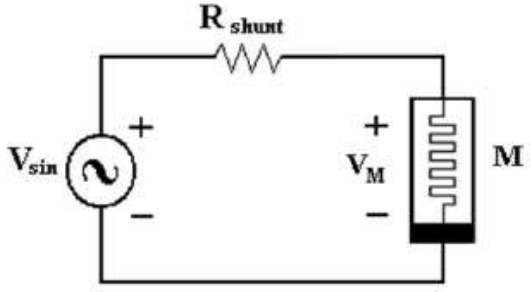

Fig. 3.3. Circuit for the measurement of the $v - i$ characteristics of the memristor.

For a more systematic analysis the sourcemeter has been used. It was set in order to run a voltage sweep from $0V$ to V^+ (the higher

value of the voltage applied on the device), from V^+ to $0V$, from $0V$ to V^- (the lower value of the voltage applied) and from V^- to $0V$.

For the tests, we have acquired from 20 to 50 points (typically 50) in each of the four curves; the amplitude of the voltage applied is different for all the devices analyzed, usually in the range [-1,1], or [-2.5,2.5]. Only in a specific case we have tested the memristor with $V^+ = 9.5$ and $V^- = -9.5$.

3.4.1 Characterization of the printed memristors

In order to investigate the behavior of the printed memristors different experiments have been done. For each device a set of $v-i$ measurements has been performed, in particular by varying the amplitude of the voltage applied across the device, the number of acquired points, and the settling time, that is, the delay period after which the measurement is made.

Some of the devices analyzed have been found to be short circuited, other ones instead of the pinched hysteresis loop exhibited a very low current and a straight line profile. For the samples with memristive behavior, the amplitude of the voltage was set to $V^+ = 1$ and $V^- = -1$, the settling time was varied from $0.01s$ to $2s$, the number of points in each sweep was varied from 20 to 50 (from 80 to 200 points for each hysteresis loop).

For all measurements the test script builder, an application to communicate with Keithley products, has been used.

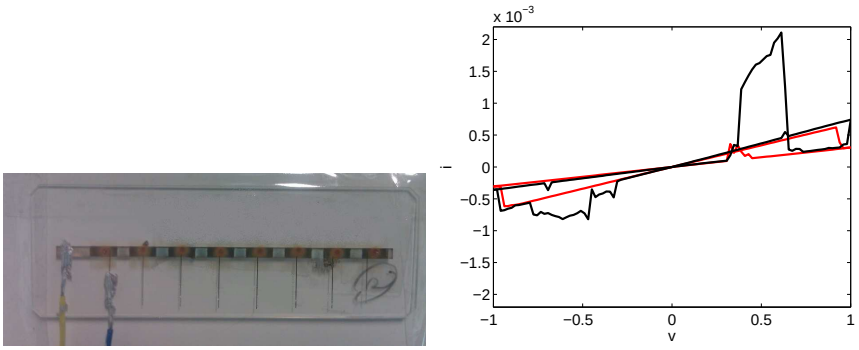

(a) (b)

Fig. 3.4. (a) A photo of an array of eight TiO_2 printed memristor on glass, labeled as $2.1, 2.2, \ldots, 2.8$, and (b) two pinched hysteresis loops of the device 2.1.

In Fig. 3.4 the device and the $v-i$ characteristics of one of the memristor analyzed are reported. The same device shows different pinched hysteresis loops (Fig. 3.4(b)), the memristor changes its state during the measurements.

The second group of memristors, reported in Fig. 3.5(a), was tested with a voltage sweep with $V^+ = 9.5V$ and $V^- = -9.5V$. An example of the resulting characteristics is reported in Fig. 3.5, obtained at different times with the same memristor.

3.4.2 Characterization of the drop coated memristors

The drop coated memristors have been characterized by using the same protocol of the printed memristors. In Fig. 3.6 two pinched hysteresis loops of the $R32$ memristor are reported. This device has been characterized with $V^+ = 2.5$ and $V^- = -2.5$. The behavior of another memristor, $R37$, is reported in Fig. 3.7.

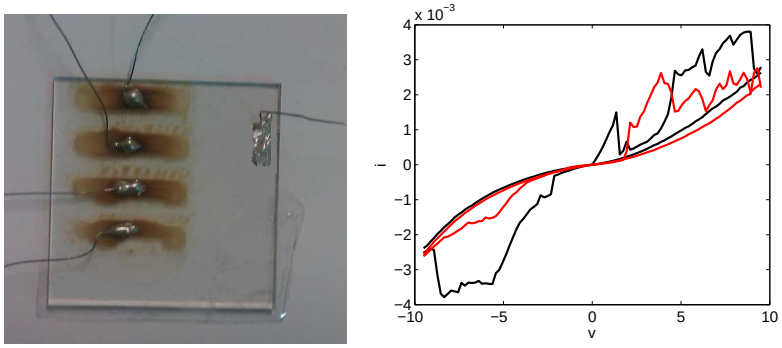

(a) (b)

Fig. 3.5. (a) A photo of an array of four TiO_2 printed memristors on ITO-glass, labeled as device 3.1, 3.2, 3.3, 3.4; (b) two pinched hysteresis loops of the 3.1 memristor.

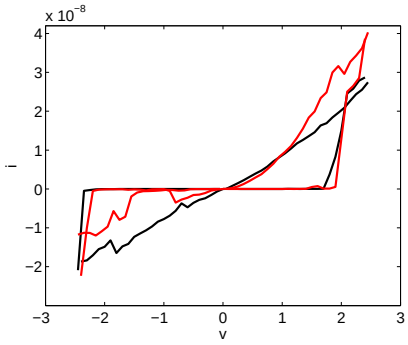

Fig. 3.6. An example of $v - i$ characteristic for the drop coated memristor $R32$.

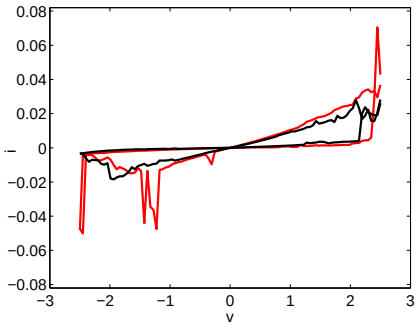

Fig. 3.7. The $v - i$ characteristic for the drop coated memristor $R37$.

3.5 A data driven model of TiO_2 printed memristors

After the fabrication of several devices showing memristive switching behavior, recently a growing interest to the realization of dynamical nonlinear circuits based on memristors has been manifested. Currently, many memristor circuits have been mostly conceived on the basis of theoretical memristor models. However, in order to analyze the dynamical behavior of memristor circuits with real components and to implement them, the characteristics of the fabricated devices have to be included in the models used. To this aim, we have proposed a compact data-driven model. The model is based on neural networks and is derived starting from experimental measurements performed on printed TiO_2 memristors.

For the applications of memristors currently under investigations, the availability of models of the device behaviors and CAD tools is fundamental, since many properties of memristors-based systems, architectures and solutions have to be tuned taking into account the peculiarities of these new devices. Given the variety of techniques and materials employed for their fabrication, the number of models developed is also large. The basic model explaining memristive behavior is the linear drift model [4], already discussed in details in Chapter 1. The model has been then extended to include nonlinear drift in [13, 14]. However, a fully detailed description of the physical effects that control memristor switching requires more complex models including the

types of transport and dynamics occurring in the device. To this aim the physics based models described in Section 1.3 were developed [15].

Starting from the analysis of the printed memristors (see Section 3.2), a neural networks based model, able to reproduce the $i - v$ characteristics experimentally observed, is proposed. The model is derived starting from an experimental campaign of measurements and using the data to train a neural network. The methodology is however independent of the fabrication technology.

3.5.1 Analysis and results

The device was tested by using a Keithley 2602 programmable sourcemeter. The measurements used for the model were performed by applying a voltage sweep from $-9.5V$ to $9.5V$, and viceversa, with step size of $0.2V$ and a settling time equal to $0.1s$ to the terminals of the device, and recording the current through the device. After that, the $i - v$ curve is plotted. The method allows to recover the main feature of the memristive behavior, that is, an hysteresis pinched loop in the $i - v$ plane.

Fig. 3.8 reports three hysteresis cycles, obtained at different times but under the same nominal working conditions. Despite the qualitatively similar behavior, the area of the hysteresis is different in the three cases and in one of them a large peak in the response is observed.

Furthermore, a significant variability of the device response which may be due to the technology used for memristor fabrication, still at

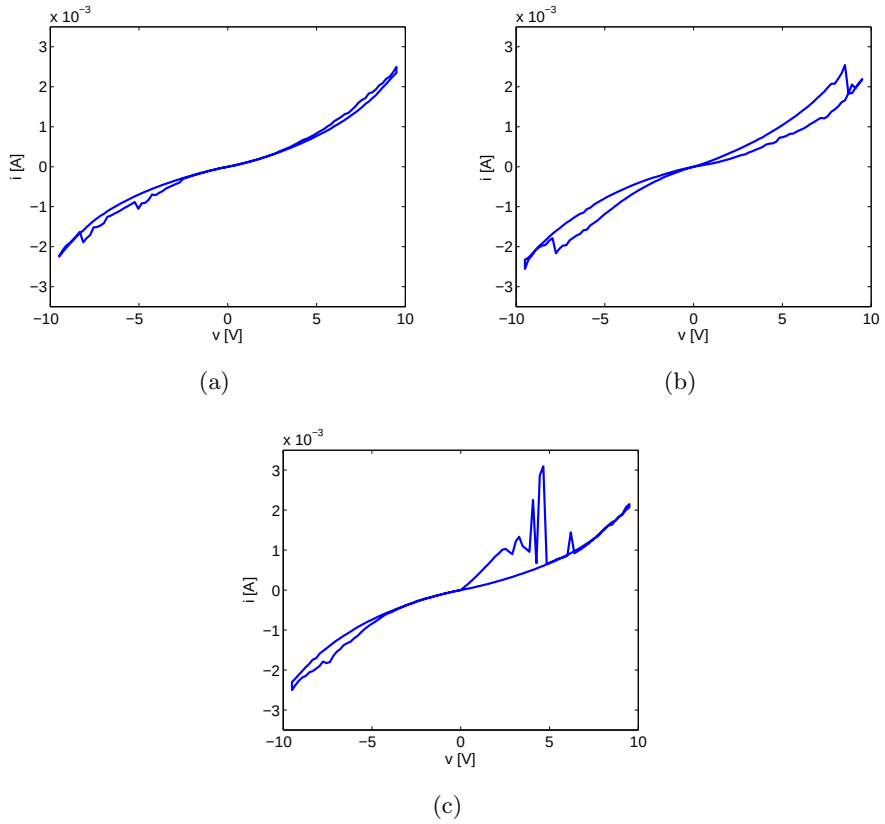

Fig. 3.8. Experimental results. Three different pinched hysteresis loops under nominally equal initial conditions are shown in (a), (b) and (c).

an early stage, and that our neural networks based model is able to capture, has been observed.

The tests have been repeated several times (up to 20-30 different trials) on the same device and on different devices. The same behavior has been found for all the trials and devices tested. We also note that peaks in the response of memristors have been recorded in other independent experiments [39].

We have first compared the results of our experimental characterization with a model fit based on the nonlinear drift model proposed in [4], including different window functions [14, 13], but we have found that these models do not accurately describe the $i - v$ characteristics of our memristor, and, in particular, the great variability of the experimental behavior under nominally identical conditions. For this reason, we have developed a simple data-driven model based on neural networks.

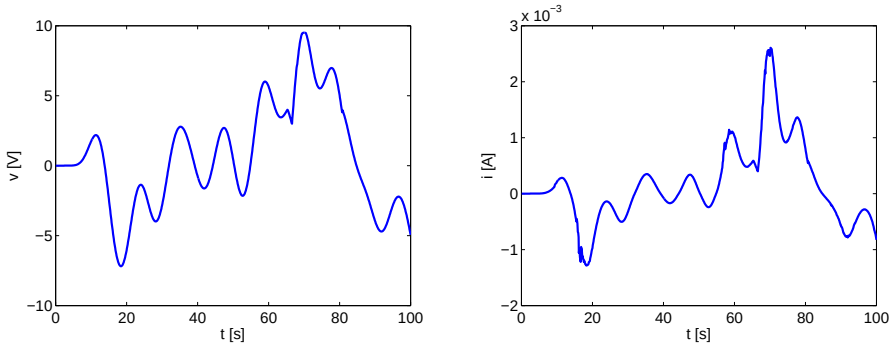

(a) (b)

Fig. 3.9. Data used for training: (a) input (waveform of the voltage applied to the memristor); (b) output (waveform of the memristor current).

Due to the characteristics of the memristors, the most appropriate assumption for the model is to consider a NARMAX (nonlinear autoregressive moving average with exogenous inputs) model. Considering the applied voltage on the memristor as the input, $u(t) \in \mathcal{R}$, and the current as the output, $y(t) \in \mathcal{R}$, and indicating as n the system order, the NARMAX model is described by:

$$y(t_k) = f(y(t_{k-1}), ..., y(t_{k-n}), u(t_k), ..., u(t_{k-n})) \tag{3.1}$$

where $t_k - t_{k-1} = \Delta T$ is the sampling time. The NARMAX model considered here is based on one hidden layer multilayer perceptron trained by using the Levenberg-Marquardt algorithm with early stopping strategy to avoid overlearning [40].

The first phase in model derivation dealt with the acquisition of the appropriate measures for learning and validating the model. We run a campaign of measurements devoted to acquire the response of the memristor to the input waveform shown in Fig. 3.9(a). The response of the memristor to this waveform is also shown in Fig. 3.9(b). Additional data (used for validation) are the hysteresis pinched loops reported in Fig. 3.8. All data used for model derivation have been normalized to be in the range of $[-1, 1]$.

The data have been divided into data for learning, for test and for validation. The data reported in Fig. 3.9 have been used for the training phase (70% for learning, 15% for testing and 15% for validation). Data have been first shuffled so that their order is randomized.

Based on the a priori knowledge on the memristor dynamics and previously reported models, the system order was fixed as $n = 1$, while the number of units in the hidden layer was determined by using a trial and error strategy. After this, a structure with 5 hidden neurons has been selected as the one showing the best results.

After training, a further validation was carried out on the set of data, most significant from the point of view of memristor analysis, that is, the series of pinched hysteresis loops of Fig. 3.8(a)-3.8(c). The main re-

sults of this validation step are shown in Fig. 3.10, which demonstrates how the obtained neural network is able to reproduce the variability in the hysteresis loop of the device. In particular, the neural network based model is able to fit the hysteresis loops in Fig. 3.10(a)-3.10(c) which correspond to the experimental data reported in Fig. 3.8(a)-3.8(c). This shows how the variability can be explained by taking into account the different initial condition of the memristor internal state.

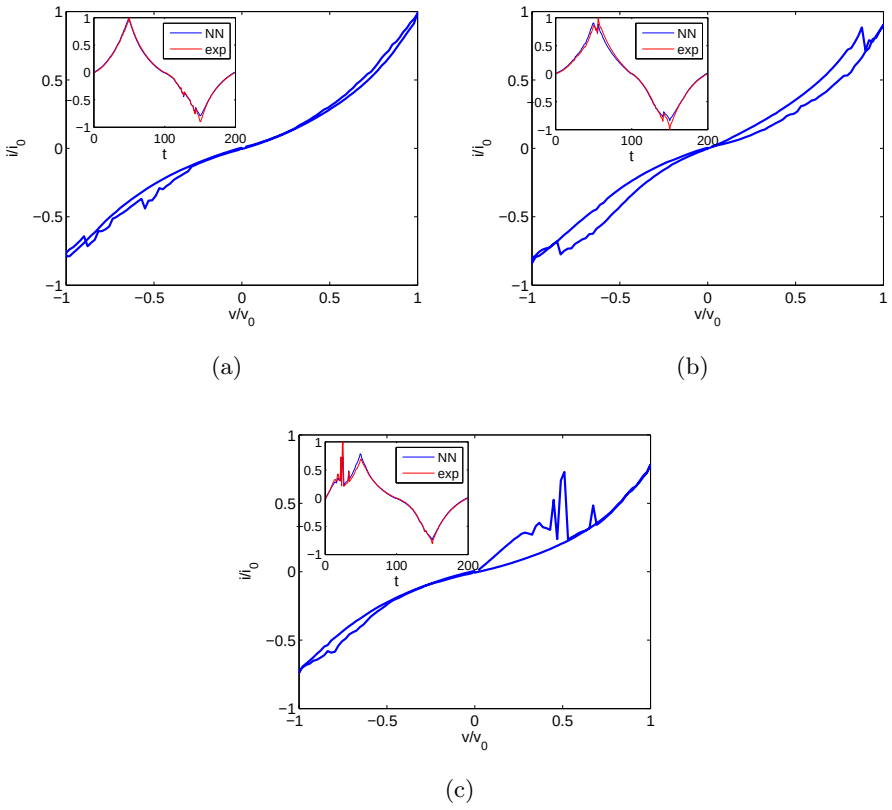

(a) (b)

(c)

Fig. 3.10. Pinched hysteresis loop obtained by the neural networks based model.

3.6 An hybrid chaotic circuit based on memristor

The circuits discussed in Chapter 2 are all based on a configuration of two memristors in antiparallel. The idea, illustrated here and originating from the experimental approach for characterization discussed in the previous Sections, is to realize a chaotic system exploiting the nonlinearity of only one memristor with a very simple experimental setup.

As previously mentioned the characterization is performed by using a Keithley 2602 programmable sourcemeter. Measurements are performed by applying a voltage waveform and recording the current through the device (usually, a sinusoidal input to recover the hysteresis pinched loop in the $i - v$ plane, or pulse functions to investigate the time response of the memristor). Looking more in detail at the voltage waveform applied to the memristor through the sourcemeter, this is a sweep of steps of programmable amplitude and duration. The measurement is then made at each step after a specified delay period (the sampling time ΔT). We used steps with fixed duration, so that the applied waveform is a continuous-time signal generated by the conversion of a discrete-time signal through a zero-order hold.

We have investigated the effect of establishing a relationship between the measured current and the next sample of the applied voltage signal, that is, we drive the memristor on the basis of the current flowing through it. This is particularly simple to realize since it only requires a memristor and a programmable sourcemeter.

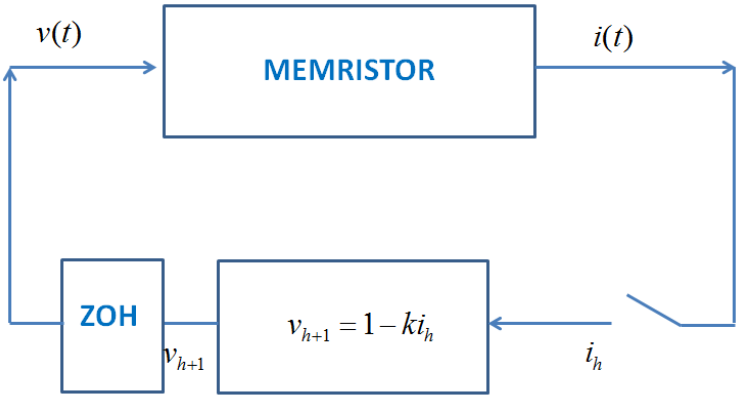

Fig. 3.11. The memristor based hybrid circuit.

The scheme adopted is illustrated in Fig. 3.11, where $v(t)$ indicates the voltage applied to the memristor, that is, an ADC converted signal. The current of the memristor, indicated with $i(t)$, is sampled into a sequence of samples i_h. Each sample i_h is used to generate the next voltage sample v_{h+1} through the relation:

$$v_{h+1} = 1 - ki_h \tag{3.2}$$

where k is a constant parameter. The sequence of samples v_h is converted into the analog signal $v(t)$ through the zero-order hold (ZOH), so that:

$$v(t) = v_h, t_h \leq t < t_{h+1} \tag{3.3}$$

with $t_h = h\Delta T$. The sampling of $i(t)$ occurs immediately before the sweep of the voltage from v_h to v_{h+1}, that is, $i_h = i(t)|_{t=t_{h+1}^-}$. The sampler, the processor implementing Eq. (3.2) and the ZOH are all

implemented in the sourcemeter. We notice that Eq. (3.2) are linear, so that the only nonlinearity in the system is given by the memristor.

We first discuss numerical results, obtained by substituting the memristor with its constitutive equations according to the model in Eqs. (1.7). The resulting scheme is shown in Fig. 3.12.

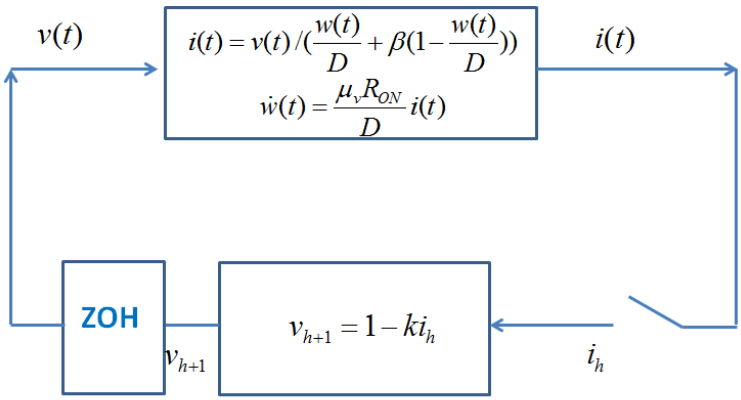

Fig. 3.12. Scheme used for numerical analysis of the memristor based hybrid circuit.

We have analyzed the system with respect to the parameters k and β and we have found that there are several regions in the parameter space for which chaotic behavior arises. An example is reported in Fig. 3.13 where the time evolution of the variables $v(t)$, $w(t)$ and $i(t)$ are shown for $k = 10$ and $\beta = 100$. In Fig. 3.14 the bifurcation diagram with respect to k (for $\beta = 100$) is illustrated, it shows alternating regions of periodic behavior and chaos. The bifurcation diagram with respect to β is reported in Fig. 3.15 (for $k = 10$), showing how chaos is preserved for a wide range of values of the constitutive parameter β. Since β may vary in real memristors due to technology, fabrication process and

device characteristics, the robustness with respect to this parameter is particularly significant.

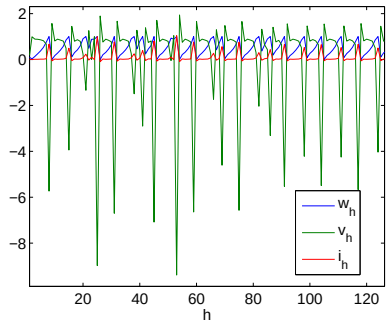

Fig. 3.13. Trend of voltage, current and doped region width of the memristor based hybrid system for $k = 10$ and $\beta = 100$.

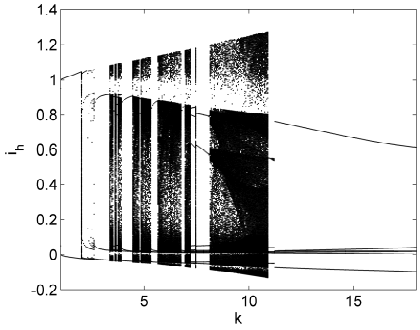

Fig. 3.14. Bifurcation diagram of the memristor based hybrid system with respect to k ($\beta = 100$).

Experimental results have been obtained by using the scheme of Fig. 3.11 and the printed TiO_2. The time evolution of $i(t)$ and $v(t)$ for $k = 3000$ is reported in Fig. 3.16.

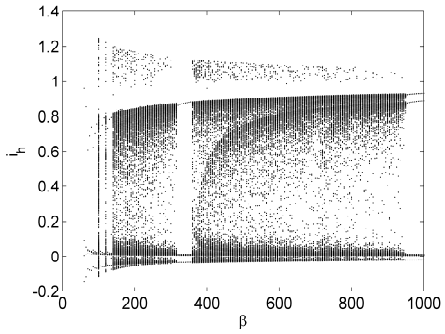

Fig. 3.15. Bifurcation diagram of the memristor based hybrid system with respect to β ($k = 10$).

We observe that the numerical results have been obtained with a rescaled set of equations, so that, during experimental tests the value of k has been rescaled. We notice that experiments confirm the irregularity of the behavior of the hybrid circuit and therefore the suitability of this simple approach to generate chaos. However, the appearance in the experiments of peaks not observed in simulations indicates that the simplified mathematical model of Eqs. (1.7) is able to capture the general behavior of the system, but not the details of the waveforms observed in the experiments.

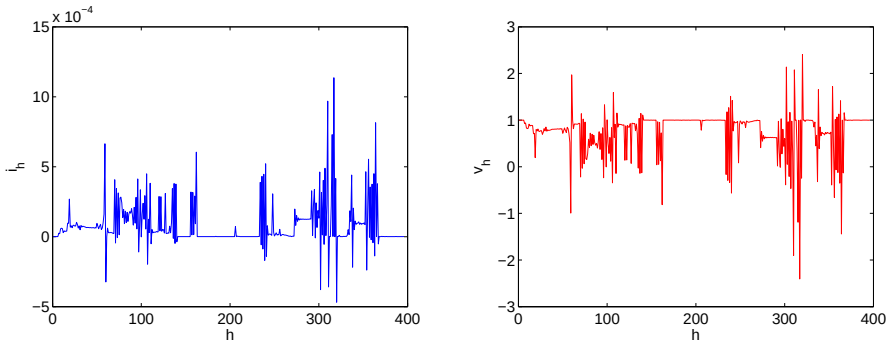

(a) (b)

Fig. 3.16. Experimental results: time evolution of current and voltage in the memristor based hybrid circuit for $k = 3000$.

Part II

Complex networks

4

Remote synchronization

In the second part of the thesis we have focused on complex networks and, in particular, on the study of remote synchronization in complex networks. Remote synchronization is a new kind of synchronization that was found in star-like motifs of coupled periodic oscillators, where the central hub is characterized by a frequency mismatch with the peripheral nodes of the network. In such network a regime, in which the peripheral nodes are synchronized while the hub is not, has been numerically and experimentally observed. We show here that remote synchronization is quite common in Erdős-Rényi and scale-free networks. Although a straightforward generalization of the remote synchronization appearing in star-like networks can be observed in networks having a structure where star-like motifs are abundant, the phenomenon is more general as RS links commonly appear in networks with arbitrary structures. In such more general cases we have found either a single node that remotely synchronizes with another

node or an entire community of synchronized nodes that remotely synchronizes with another community of synchronized nodes. Furthermore, the passage of information needed for remote synchronization occurs either through hubs or low-degree nodes.

4.1 Introduction

Synchronization constitutes one of the most paradigmatic examples of emergence of collective behavior in natural, social and man-made systems [41, 42, 43]. Its ubiquity relies on the general framework in which it occurs: the interaction between two or more nonidentical dynamical units that, as a consequence, adjust a given property of their motion. As coupling between units increases, synchronization shows up as a collective state in which the units behave in a coordinated way. Synchronization phenomena span across many life scales, ranging from the development of cognitive tasks in neural systems [44] to the onset of social consensus in human societies [45].

The ubiquity of synchronization in real systems together with the recent discovery [46, 47, 48, 49, 50] of their real architecture of interactions has motivated its study when units are embedded in a complex network [51]. In this way, each unit is represented as a node of a network while it only interacts with those adjacent units, *i.e.* those directly coupled via an edge. In the last decade many studies have unveiled the

impact that diverse interaction topologies have on the onset of synchrony [52, 53, 54, 55, 56] and its stability [57, 58, 59, 60].

The former studies mainly rely on the study of coupled phase oscillators, such as the Kuramoto model [61, 62], which produces globally synchronized systems as a result of the direct interaction of pairs of adjacent units. However, it has been recently found [63] that, for more general oscillator models (in which both amplitude and phase are dynamical variables) such as the Stuart-Landau (SL) model [42], two oscillators, that are not directly linked but are both connected to a third unit, can become synchronized even if the third oscillator does not synchronize with them. This novel phenomenon, termed *remote synchronization* (RS), relies on the modulation of the amplitude parameter of an intermediary node allowing the passage of information between two of its neighbors for their synchronization, even when the former is not synchronized with them.

Remote synchronization has been found to occur in very specific and simple topologies such as star-like networks in which the central node has a natural frequency different from that of the leaves. Within this particular setting it was numerically and experimentally shown [63] that leaves become mutually synchronized without the need of the synchronization of the central node. In this Chapter, we briefly recall the main features of RS in star-like networks, discuss the role of amplitude in the onset of RS in these networks, and, then, show that RS is not limited to the particular configuration of a star-like motif or a tight specification of the node frequencies. To this end, we introduce

a general procedure for detecting remote synchronization in arbitrary networks and then discuss the results of our analysis on arbitrary complex networks.

4.2 Remote synchronization in star-like networks

We first consider a star-like network of N coupled Stuart-Landau oscillators [42]. The dynamics of each node i is governed by the following equations:

$$\begin{aligned} \dot{x}_i &= (\alpha - x_i^2 - y_i^2)x_i - \omega_i y_i + \tfrac{\lambda}{k_i}\textstyle\sum_{j=1}^{N} a_{ij}(x_j - x_i) \\ \dot{y}_i &= \omega_i x_i + (\alpha - x_i^2 - y_i^2)y_i + \tfrac{\lambda}{k_i}\textstyle\sum_{j=1}^{N} a_{ij}(y_j - y_i) \end{aligned} \tag{4.1}$$

where $\sqrt{\alpha}$ and ω_i are respectively the amplitude and the (natural) frequency of oscillator i when uncoupled. The last term on the right accounts for the coupling of the dynamics of node i with its k_i neighbors. The strength of the coupling is controlled by λ ($\lambda = 0$ in the uncoupled limit) while $\mathcal{A} = \{a_{ij}\}$ represents the adjacency matrix of the network defined as: *(i)* for $i \neq j$, $a_{ij} = 1$ when nodes i and j are connected while $a_{ij} = 0$ otherwise, and *(ii)* $a_{ii} = 0$. In this Section, we restrict the analysis to star-like networks, that is, we define node 1 as the hub and nodes $i = 1, \ldots, N$ as the leaves. So, $a_{ij} = 1$ only if $i = 1$ or $j = 1$.

To study the synchronization properties of system (4.1) we work with the phase variable of each oscillator, defined as $\theta_i = \tan^{-1}(y_i/x_i)$. Then, we measure the degree of synchronization of a pair of oscillators by means of the time averaged order parameter:

$$r_{ij} = |\langle e^{\iota[\theta_i(t)-\theta_j(t)]}\rangle_t| \ , \tag{4.2}$$

where $\langle\cdot\rangle_t$ means an average over a large enough time interval and $\iota = \sqrt{-1}$. To monitor the onset of RS, two parameters have been defined in [63]: the coherence of the peripheral cluster is measured through

$$r^{indirect} = \frac{1}{(N-1)(N-2)} \sum_{n=2}^{N} r_{nm} \tag{4.3}$$

and that of the hub with the rest of the network through

$$r^{direct} = \frac{1}{(N-1)} \sum_{n=2}^{N} r_{1n} \tag{4.4}$$

Fig. 4.1 reports the evolution of the two parameters $r^{indirect}$ and r^{direct} for a star-like network of $N = 5$ nodes when the coupling coefficient λ is varied from 0 to 1.5. In Fig. 4.1(a) $\alpha = 1$ has been considered, while in Fig. 4.1(b) $\alpha = 100$. In the first case, for intermediate values of the coupling coefficient the synchronization level among the leaves (measured with $r^{indirect}$) is higher than that between the hub and the leaves (measured with r^{direct}), thus revealing the onset of RS. In the second case, the transition in $r^{indirect}$ and r^{direct} occurs at the same value of λ.

In fact, when $\alpha >> 1$ the SL model transforms into a network of Kuramoto oscillators, so that the amplitude of the oscillators become decoupled and stationary. Under these conditions the amplitude of the hub cannot anymore transmit the information needed by the leaves to

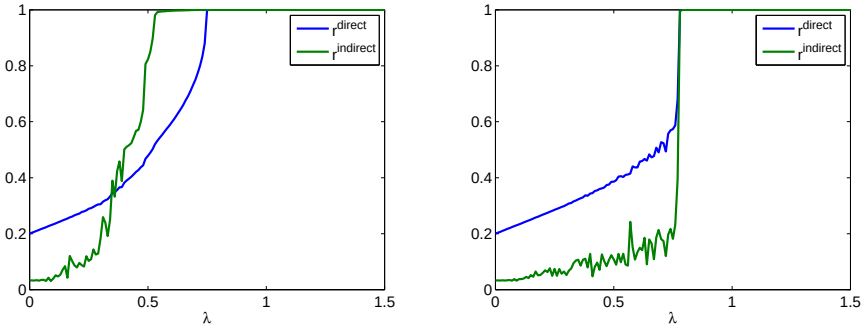

(a) (b)

Fig. 4.1. Evolution of $r^{indirect}$ and r^{direct} for a star-like network of $N = 5$ nodes. The natural oscillation frequencies are fixed as $\omega_1 = 2.5$, $\omega_2 = ...$ ...., and α as $\alpha = 1$ (a) and $\alpha = 100$ (b). For $\alpha = 1$ and for intermediate values of the coupling coefficient the synchronization level among the leaves (measured with $r^{indirect}$) is higher than that between the hub and the leaves (measured with r^{direct}), thus revealing RS which, however, disappear for $\alpha = 100$.

synchronize, thus inhibiting the mechanism underlying RS. We consider Eqs. (4.1) in polar coordinates:

$$\begin{aligned} \dot{\rho}_i &= \alpha\rho_i - \rho_i^3 + \frac{\lambda}{k_i}\sum_{j=1}^{N} a_{ij}(\rho_j \cos(\theta_j - \theta_i) - \rho_i) \\ \dot{\theta}_i &= \omega_i + \frac{\lambda}{k_i}\sum_{j=1}^{N} \frac{\rho_j}{\rho_i} a_{ij} \sin(\theta_j - \theta_i) \end{aligned} \tag{4.5}$$

where $\rho_i e^{\iota\theta_i} = x_i + \iota y_i$. Defining $R_i = \frac{\rho_i}{\sqrt{\alpha}}$, where $\sqrt{\alpha}$ is the value of the amplitude at the equilibrium, Eqs.(4.5) can be rewritten as follows:

$$\begin{aligned} \dot{R}_i &= \alpha R_i - \alpha R_i^3 + \frac{\lambda}{k_i}\sum_{j=1}^{N} a_{ij}(R_j \cos(\theta_j - \theta_i) - R_i) \\ \dot{\theta}_i &= \omega_i + \frac{\lambda}{k_i}\sum_{j=1}^{N} \frac{R_j}{R_i} a_{ij} \sin(\theta_j - \theta_i) \end{aligned} \tag{4.6}$$

In the first equation we can rescale time according to $dT = \alpha dt$ (while the second equation remains unchanged).

$$\begin{aligned} \frac{dR_i}{dT} &= R_i - R_i^3 + \frac{\lambda}{\alpha k_i} \sum_{j=1}^{N} a_{ij}(R_j \cos(\theta_j - \theta_i) - R_i) \\ \dot{\theta}_i &= \omega_i + \frac{\lambda}{k_i} \sum_{j=1}^{N} \frac{R_j}{R_i} a_{ij} \sin(\theta_j - \theta_i) \end{aligned} \tag{4.7}$$

Now as $\alpha \to \infty$ the coupling term in the amplitude equation vanishes, and from the analysis of the first equation we derive that $R_i \to 1$ for all i (in fact $R_i = 1$ is the only equilibrium and the dynamics evolve very fast as $dT = \alpha dt$ and α is large). In the second equation $R_i \to 1$ leads to $\frac{R_i}{R_j} = 1$ and thus the second equation becomes:

$$\dot{\theta}_i = \omega_i + \frac{\lambda}{k_i} \sum_{j=1}^{N} a_{ij} \sin(\theta_j - \theta_i) \tag{4.8}$$

Therefore, as $\alpha \to \infty$, we recover the model of Kuramoto purely phase oscillators coupled into a network. In this limit, we observe that the amplitude equation plays no role. In this case (Fig. 4.1(b)) RS disappears (we note that for $\alpha = 100$ the network of Stuart-Landau oscillators is already a good approximation of the network of Kuramoto purely phase oscillators). The inhibition of the modulation of amplitude of the hub in the case of $\alpha = 100$ is evident in the bifurcation diagram reported in Fig. 4.2, where the local maxima of the normalized amplitude variable $A = \sqrt{\frac{x_1^2 + y_1^2}{\alpha}}$ are reported. When $\alpha = 1$, the amplitude of the hub is modulated until the leaves become synchronized, while when $\alpha = 100$ the amplitude is constant and RS is not possible. The onset of RS can be thus monitored through the variance of parameter A, that is $\sigma^2(A)$. For example, Fig. 4.3 shows, for a network of $N = 5$

nodes $\sigma^2(A)$ as a function of λ and α, revealing the region where RS appears.

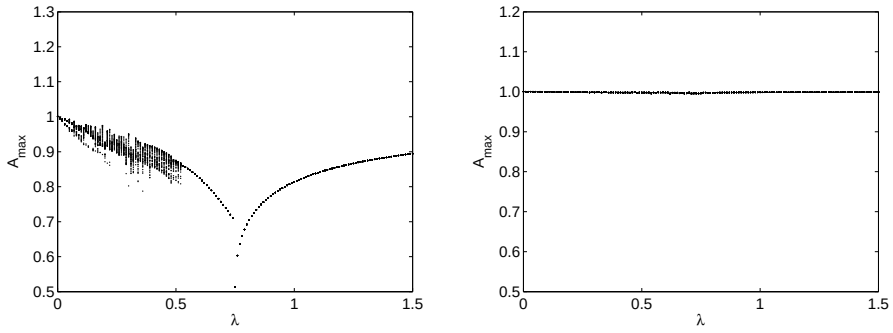

Fig. 4.2. Bifurcation diagram of the amplitude of the hub with respect to the coupling parameter for $\alpha = 1$ (a) and $\alpha = 100$ (b) for a star-like network of $N = 5$ nodes with frequency distribution as in Fig. 4.1.

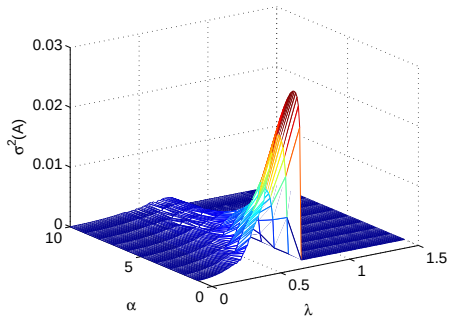

Fig. 4.3. Bifurcation diagram of $\sigma^2(A)$ with respect to λ and α for a star-like network of $N = 5$ nodes with frequency distribution as in Fig. 4.1.

4.3 Measures of remote synchronization in complex networks

In Section 4.2, where star motifs were dealt with, RS is detected by monitoring $r^{indirect}$ and r^{direct}. Such measures are not applicable to the general case of arbitrary topologies, since they are based on an a priori analysis of the network structure which allows one to establish which nodes can remotely synchronize. Therefore, in this Section we introduce a general procedure for detecting remote synchronization in arbitrary networks and then show ubiquity and robustness of remote synchronization in the general case of complex networks.

To this end, we now consider in Eqs. (4.1) a generic topology $\mathcal{A}$. We measure the degree of synchronization of any connected or not pair of oscillators by r_{ij} and consider two nodes as synchronized when $r_{ij} > \delta$, where δ is a constant threshold that we fix to $\delta = 0.8$.

Once two nodes i and j are classified as mutually synchronized we label their relationship according to the following three situations: *(i)* i and j are directly connected ($a_{ij} = a_{ji} = 1$), *(ii)* there is a path of mutually synchronized nodes between them, and *(iii)* neither of the former two situations hold. While the first two cases are similar, as both are examples of synchronization through *physical links*, the third case is analogous to the observed remote synchronization in a star-like network, but in the more general context of a complex network. Thus, we define that two nodes i and j are remotely synchronized (RS) when

they are synchronized ($r_{ij} > \delta$) and they are not connected by either a direct link or a path of synchronized nodes.

To quantify systematically the extent of remote synchronization we count the number of RS nodes, defined as the number N_{RS} of nodes that appear RS with at least another node in the network. This allows us to introduce the following order parameter: $n_{RS} = N_{RS}/N$, representing the normalized number of RS nodes with respect to the total number of nodes N.

Finally, to quantify the importance that remote synchronization has on the dynamics of the system we also measure the global level of synchronization through the usual Kuramoto-like order parameter:

$$r = \frac{1}{N^2} \sum_{i,j=1}^{N} r_{ij} \ . \tag{4.9}$$

Note that r takes into account the contribution of both synchronized ($r_{ij} > \delta$) and not synchronized ($r_{ij} \leq \delta$) nodes.

4.4 Results

As two well-known paradigmatic network topologies we have analyzed both Erdős-Rényi (ER) and Scale-free (SF) graphs. The former type of networks is characterized by a Poisson distribution $P(k)$ for the probability of finding a node with k contacts while SF graphs show a power-law distribution, $P(k) \sim k^{-\gamma}$. Thus, while in ER graphs most of the nodes are close to the mean connectivity $\langle k \rangle$, SF networks display a large heterogeneity in the number of contacts per node as revealed from

the existence of hubs having $k_i \gg \langle k \rangle$. For their construction we have made use of the model introduced in [64] that allows one to control the mean connectivity of both networks in order to be exactly the same. In the analyzed networks the size and mean connectivity are fixed to $N = 100$ and $\langle k \rangle = 2$ respectively. The SF networks generated with this model have $\gamma = 3$.

We have considered a bimodal distribution for the natural frequencies of the oscillators so that nodes with high degree (those analogous to the central nodes in a star graph) present a larger frequency, ω_h, than that, ω_l, of less connected (the ones playing the role of leaves in the star topology). In particular, we labeled as hubs those nodes having $k_i > k^*$ (the value of k^* is set so that the percentage of hubs is around the 20% of the total number of nodes in the network) and assigned them $\omega_i = \omega_h + \xi_i \omega_h$ while, for the rest of nodes $\omega_i = \omega_l + \xi_i \omega_l$. In the former expressions ξ_i is a random variable uniformly distributed between -0.025 and 0.025.

In Fig. 4.4 we show the emergence of remote synchronization as a function of the two relevant parameters: the coupling strength λ and the frequency mismatch of the network hubs $\Delta\omega = \omega_h - \omega_l$. In particular, we report the behavior of the global synchronization, r, [panels 4.4(a) and 4.4(c)] and the fraction of RS nodes, n_{RS}, [panels 4.4(b) and 4.4(d)] for SF (top) and ER (bottom) networks. The results are averaged over 50 different network instances and, for each network we average the results over 10 different realizations of the distribution of natural frequencies.

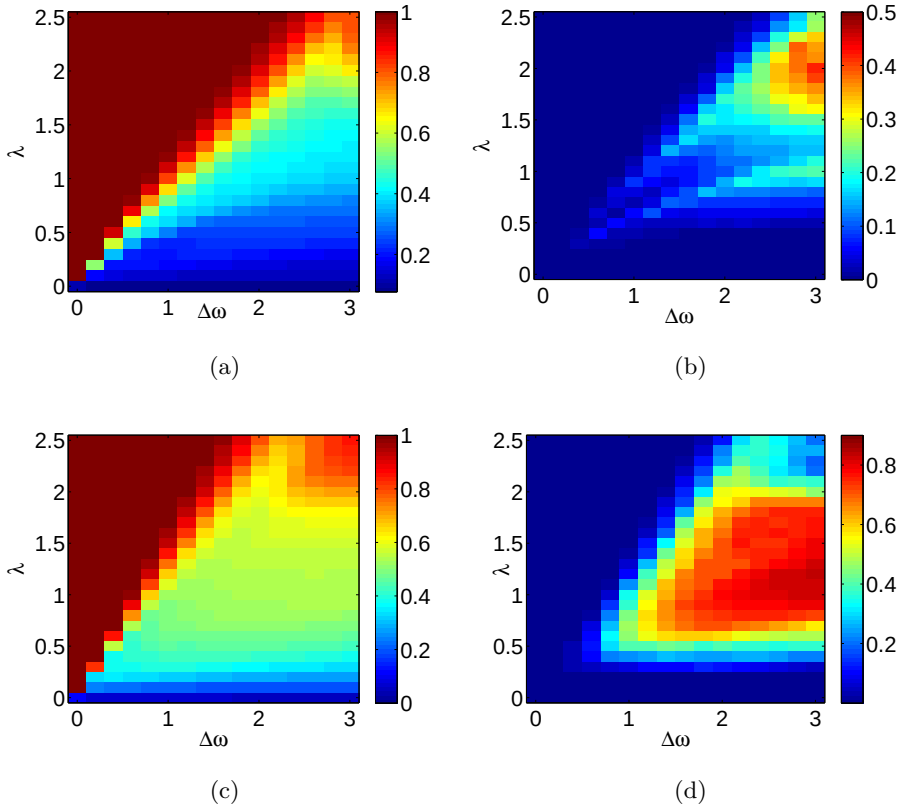

Fig. 4.4. Evolution of the degree of global synchronization r [panels (a) and (c)] and the number of remotely synchronized nodes n_{RS} [panels (b) and (d)] for SF (upper panels) and ER (bottom panels) networks as a function of the coupling strength λ and the frequency mismatch $\Delta\omega$. In both cases the networks have $N = 100$ and $< k >= 2$. The other relevant parameters are fixed to $\alpha = 1$, $\omega_l = 1$. Remote synchronization (high values of n_{RS}) is found for strong frequency mismatch $\Delta\omega$ and moderate coupling λ, while, for low values of the coupling parameter, nodes cannot synchronize (r and n_{RS} have low values), and, for large values of λ, the network is fully synchronized ($r \simeq 1$).

We find that remote synchronization occurs in both types of networks in a region of parameters characterized by a strong frequency mismatch $\Delta\omega$ and moderate coupling λ. In fact, for low values of the coupling parameter, nodes cannot synchronize (either in a direct or remote way) as observed from the low values of r and n_{RS}. On the contrary, for large values of λ the network is fully synchronized ($r \simeq 1$) and, accordingly, n_{RS} assumes values close to zero since all the nodes are mutually synchronized with their neighbors. As panels 4.4(a) and 4.4(c) reveal, the onset of full synchronization requires greater values of the coupling as the frequency mismatch increases. In fact, a large frequency mismatch together with values of coupling under the threshold for complete synchronization favors the onset of remote synchronization, as observed from the behavior of n_{RS} in panels 4.4(b) and 4.4(d).

Compared to SF networks, the values of n_{RS} in ER networks are greater, thus indicating that remote synchronization in ER networks involves a larger number of nodes. Moreover, in ER networks the onset of remote synchronization occurs for lower values of λ. ER and SF networks also show qualitative differences in the appearance of remote synchronization: by keeping fixed $\Delta\omega$ and increasing the value of λ, we find that n_{RS} in SF networks show two peaks, while for ER networks it shows a rise-and-fall behavior.

In both (ER and SF) cases remote synchronization appears as an intermediary state before full synchronization is achieved. However, from the analysis of panels 4.4(a) and 4.4(c) one observes that the behavior of r *vs.* λ for a fixed value of $\Delta\omega$ is qualitatively different in SF and ER

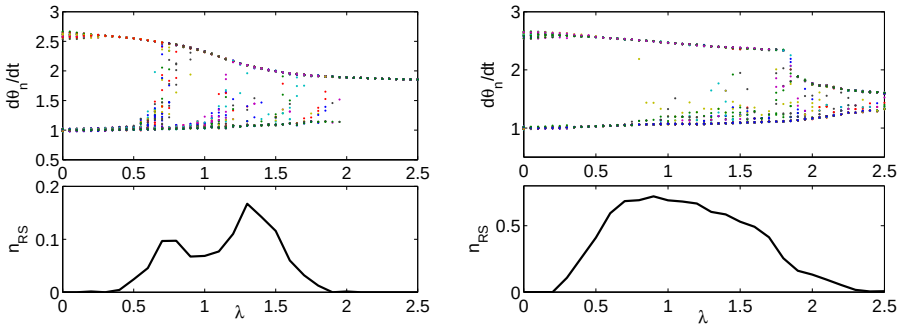

(a) (b)

Fig. 4.5. Evolution of the average oscillation frequency of each oscillator and n_{RS} as a function of λ for SF (a) and ER (b) networks. The mismatch of natural frequencies is $\Delta\omega = 1.5$ while the rest of parameters are the same as in Fig. 4.4. The average oscillation frequencies, which for $\lambda = 0$ start from a bimodal distribution as dictated by the configuration for the natural frequencies, as λ is increased tend towards a common value, characterizing full synchronization. The strong reorganization of the frequencies (characterized by a spread of the oscillation frequencies between the two extreme values) corresponds to the values of coupling for which n_{RS} is peaked.

networks. In particular, in ER networks (panel 4.4(c)) a large plateau around $r \simeq 0.5$ is set in the region where remote synchronization shows up. In this region, the increase of λ does not contribute to the overall synchronization level, but to a redistribution of the average oscillation frequencies of the network nodes.

This is evident in Fig. 4.5, where the average values (over the simulation time T) of the instantaneous frequency of each oscillator are reported along with the parameter n_{RS}. The results are obtained by increasing λ adiabatically from $\lambda = 0$ so that the system starts from a bimodal distribution as dictated by the configuration for the natural

oscillations. As λ increases, the gap between the two main frequency values of the bimodal distribution decreases until the network reaches full synchronization and the nodes oscillate at a common frequency. The readjustment of frequencies reveals that, for some values of the coupling, the system undergoes a strong reorganization, as shown by the spread of the oscillation frequencies between the two extreme values. This readjustment coincides with the peaks displayed by n_{RS} in both SF and ER networks. However, the readjustment seems to occur faster in SF networks for which the plateau of r is not observed.

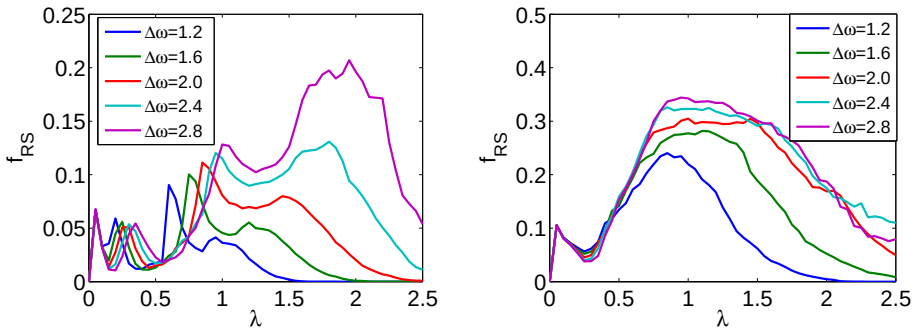

Fig. 4.6. Evolution of the fraction of RS links, f_{RS}, in SF (a) and ER (b) networks as a function of the coupling strength λ, and for different values of $\Delta\omega$. The remaining parameters are set as in Fig. 4.4. The fraction of RS links first increased as λ is increased, with one (in ER networks) or two peaks (in SF networks) as observed for the evolution of n_{RS}, and then falls as networks recruit physical (instead of RS) links to get synchronized.

To gain more insight into the relation between the regime of remote synchronization and the onset of global synchrony we now consider

the analysis of all synchronized pairs and its partition into those corresponding to remote synchronization and those for which a synchronized physical connection (either a direct link or a path of synchronized nodes) exists. To this aim, we define $\eta_{ij} = 1$ if nodes i and j are connected either by a physical link or by a path of synchronized nodes and $\eta_{ij} = 0$, otherwise. We then introduce the following quantities:

$$f_P = \frac{\sum_{i,j=1}^{N} \eta_{ij} H(r_{ij} - \delta)}{\sum_{i,j=1}^{N} H(r_{ij} - \delta)}\,, \tag{4.10}$$

and

$$f_{RS} = \frac{\sum_{i,j=1}^{N} (1 - \eta_{ij}) H(r_{ij} - \delta)}{\sum_{i,j=1}^{N} H(r_{ij} - \delta)}\,, \tag{4.11}$$

where $H(x)$ is the Heaviside function. Thus, f_P and f_{RS} represent the fraction of synchronized links due to a physical or remote connection, respectively. Obviously, as $f_P + f_{RS} = 1$, it is enough to report the behavior of f_{RS}.

In Fig. 4.6 we show the evolution of f_{RS} vs. λ for several values of $\Delta\omega$. The presence of two peaks in the evolution of f_{RS} in SF networks reveals a similar behavior to that found for n_{RS}. As $\Delta\omega$ increases, the percentage of RS links increases and the two peaks shift towards increasing values of λ. On the other hand, for ER networks the percentage of RS links is higher than in SF networks and f_{RS} shows, as in the case of n_{RS}, a rise-and-fall trend. The fall in the number of RS links points out that the network is able to recruit physical links to get synchronized and thus those regions that appeared as RS become merged into a single component made of physically synchronized links.

To visualize the progressive substitution of RS links by physical ones in the path towards full synchronization we show in Fig. 4.7 for an ER network (with $\Delta\omega = 2.8$) snapshots of both remotely and physically synchronized links for two values of the coupling λ. In Figs. 4.7(a) and 4.7(c) we plot two networks corresponding to physically and remotely synchronized links respectively when $\lambda = 1.65$. In this case the network is divided into several clusters of physically synchronized nodes (the color of the nodes corresponds to the cluster of physically synchronized links they belong to) and some nodes of these clusters appear remotely synchronized with nodes belonging to different clusters [as shown in Fig.4.7(c)]. When λ is increased to $\lambda = 1.70$, two of these clusters merge together [Fig. 4.7(b)] through two physically synchronized links that connect each cluster to a new node synchronized to each of them. Thus, at $\lambda = 1.70$ two communities, that were remotely synchronized at $\lambda = 1.65$, fuse into a single one and, as a consequence, those RS links between the nodes of the two communities reported for $\lambda = 1.65$ in Fig. 4.7(c) disappear at $\lambda = 1.70$ [Fig. 4.7(d)]. We note that the choice of the threshold δ may impact on which nodes are assigned to which groups, although we have observed qualitatively similar results when the threshold is changed. In fact, the evolution of communities remains the same, although the value of λ at which they merge may be slightly different.

Although the original discovery of remote synchronization was restricted to a rather particular setup, a star graph, the analysis carried out, through the introduction of appropriate indicators, reveals that

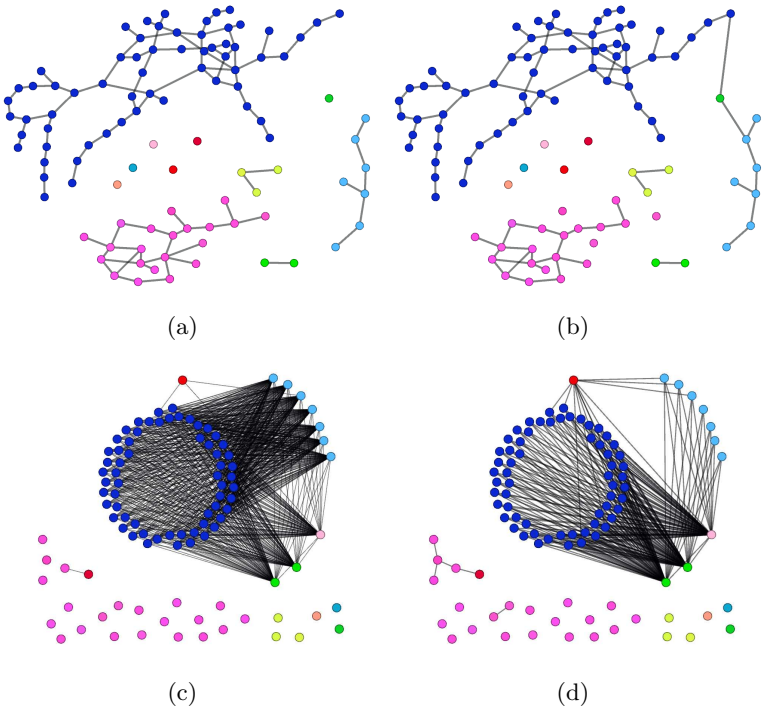

Fig. 4.7. Evolution of components of physically (a)-(b) and remotely (c)-(d) synchronized nodes in an ER network with $\Delta\omega = 2.8$, when λ is increased by adiabatic continuation from $\lambda = 1.65$ (a)-(c) to $\lambda = 1.70$ (b)-(d). Nodes are colored according to the physically synchronized component they belong to when $\lambda = 1.65$, *i.e.* in (a). The remaining parameters are the same as in Fig 4.4. At $\lambda = 1.70$ two communities (the one with blue nodes and the one with cyan nodes), that were remotely synchronized at $\lambda = 1.65$, fuse into a single one and, as a consequence, the RS links between the two communities existing for $\lambda = 1.65$ disappear at $\lambda = 1.70$.

remote synchronization is common in general complex networks such as Erdős-Rényi and Scale-free graphs of coupled oscillators having amplitude and phase as dynamical variables. The addition of amplitude as a dynamical variable, in contrast with the typical framework of networks of coupled phase-oscillators, provides the observation of remote

synchronization and elucidates an important role played by it. In fact, we have found that remote synchronization constitutes a mechanism anticipating synchronization by physical links in networks with heterogeneous distribution of natural frequencies. Our results indicate that, in these networks, communities of nodes synchronized through RS links appear for values of coupling just lower than those allowing the merging of these communities through physical links. As synchronization is ubiquitous in natural and man-made systems, we retain that this can be an important mechanism to explain the emergence of communities of synchronized nodes, not connected by physical links.

Remote synchronization appears as a rather robust state prior the onset of global synchronization since for a wide range of coupling strengths almost all the nodes are remotely synchronized with, at least, another one while the level of global synchronization remains small. Thus, our results open the door for experimental observations of this novel state in which the existence of a synchronized pair cannot be associated to a given physical interaction through a single link of the network and highlight the important difference between the real (*i.e.* associated with physical links) and the functional (*i.e.* emerging from synchronization) connectivity of a network.

5

Mechanism of remote synchronization

In Chapter 4 we have shown that remote synchronization appears in complex networks with a heterogeneous distribution of natural frequencies of the nodes. Here, we further investigate the phenomenon, elucidating the mechanisms underlying it. We start from the analysis of the same kind of distribution of frequencies considered in Chapter 4, namely a bimodal distribution, and extend the analysis to other distributions.

5.1 Networks with a bimodal frequency distribution

We consider a network of N coupled Stuart-Landau oscillators as in Eqs. (4.1) and the measures for the study of RS defined in Section 4.3. To investigate the mechanism underlying the occurrence of RS in complex networks, we introduce an approach inspired to structural robustness analysis of complex networks, where, starting from the original topology, an increasing fraction of nodes or links is removed and the

changes of a characteristic parameter are monitored. In our case, we start from a homogeneous network, that is, we fix $\omega_i = \omega_l \pm 5\%$, for all network nodes, $\forall i = 1, \ldots, N$, and change the natural frequency of a fraction f of nodes so that the resulting network becomes now heterogeneous with: $\omega_i = \omega_h \pm 5\%$ $\forall i = 1, \ldots, [fN]$, and $\omega_i = \omega_l \pm 5\%$ $\forall i = [fN] + 1, \ldots, N$. Borrowing the terminology from structural robustness analysis, we indicate as an *attacked node* a node whose frequency has been changed from $\omega_l \pm 5\%$ to $\omega_h \pm 5\%$ (see Fig. 5.1). Rather than affecting the structure of the network, our attack affects the natural dynamics of the network nodes.

We define a *homogeneous path* as a path which contains only nodes at the same natural frequency and *heterogeneous* as a path which is not homogeneous. Then, we say that, when two nodes are connected only by heterogeneous paths, there is a *potential RS link* between them. In fact, attacking a node may lead to the formation of heterogeneous paths. In this paper, we relate the presence of RS to the existence/formation in the networks of heterogeneous paths. From another point of view, our approach is equivalent to the question of how to maximize the RS, given a network, a bimodal frequency distribution and a fraction f of attacked nodes.

Analogously to structural robustness analysis, nodes can be removed according to several topological criteria, e.g., they are removed on the basis of to their degree, betweenness, or selected into a random order. In our case, since the idea underlying an attack is to create the maximum number of potential RS links or, equivalently, to eliminate the

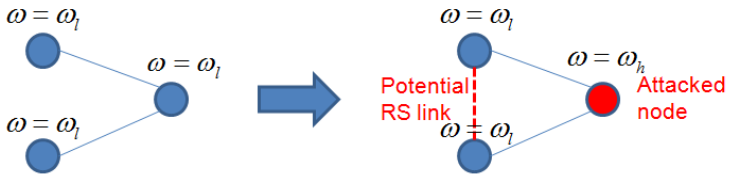

Fig. 5.1. Schematic illustration of the birth of a potential RS link when a node of the network is attacked.

maximum number of homogeneous paths (by transforming them into heterogeneous ones), we attack nodes on the basis of their betweenness centrality, that is, nodes with high betweenness centrality have to be attacked first. As far as an increasing fraction of nodes is attacked, we monitor the number of RS links, indicated as L_{RS}, and that of potential RS links, indicated as $\bar{L}_{RS}$.

We first discuss a toy model, for which we exactly calculate the number of potential RS links, and then consider the more general case of ER and SF networks. The toy example is represented by the network shown in Fig. 5.2 which has fifteen nodes with degree one, three nodes with degree six, and one node with degree three. For this toy example, we consider $f = 1/N$, that is, we attack one node of the network. It suffices to examine two cases: the case in which node 1 is attacked (that is, $\omega_1 = \omega_h \pm 5\%$ and $\omega_i = \omega_l \pm 5\%$ for $i = 2, \ldots, 19$) and the case in which node 2 is attacked (that is, $\omega_2 = \omega_h \pm 5\%$ and $\omega_i = \omega_l \pm 5\%$ for $i = \{1, 3, \ldots, 19\}$). Nodes 3 and 4 have exactly the same properties of node 2, and nodes $5, \ldots, 19$, having degree one, if attacked do not lead to any heterogeneous path.

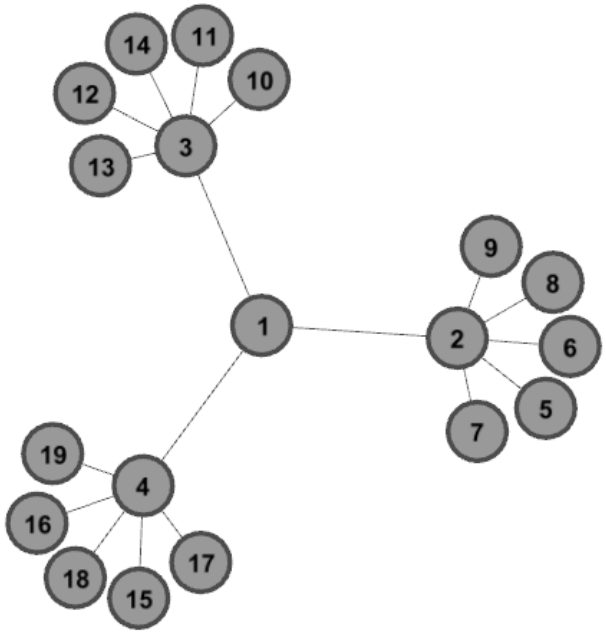

Fig. 5.2. Toy example used to illustrate the criterion to attack nodes for RS analysis.

For the first case, attacking node 1 leads the network to be split into three communities (each formed by six nodes) which are connected only by heterogeneous paths passing through the attacked node (node 1). Thus, potential RS links are created from each node of one of these communities to the nodes of the other communities. The number of potential RS links is given by: $\bar{L}_{RS} = 6 \cdot 6 \cdot 3 = 108$. In the second case, attacking node 2 leads to potential RS links among nodes $5, \ldots, 9$ and between nodes $5, \ldots, 9$ and nodes 1, 3, 4, 10, ..., 19. The number of potential RS links is given by: $\bar{L}_{RS} = \frac{5 \cdot 4}{2} + 5 \cdot 13 = 75$. We notice that

$\bar{L}_{RS}$ is higher in the first case, which corresponds to an attack to the node with highest betweenness.

In Fig. 5.3 we show the RS links appearing in the network. Fig. 5.3 refers to the value of λ which maximizes L_{RS}. For case 1 L_{RS} is exactly equal to $\bar{L}_{RS}$, while for case 2 $L_{RS} < \bar{L}_{RS}$. In case 1 (Fig. 5.3(a)), as expected, three communities form: the nodes within each of these communities (for example, nodes 2, 5-9) are synchronized through physical links; nodes among the three communities are instead synchronized through remote links. In case 2 two communities form, one made by nodes 5-9, and one by nodes 1,3,4,10-19. However, the two communities are not synchronized each other, and, therefore, remote links appear only among nodes 5-9 ($L_{RS} = \frac{5 \cdot 4}{2} = 10$). In fact, remote links do not appear between the nodes of the two communities, since nodes 5-9 oscillate at a frequency equal to 1.24, while nodes 1,3,4,10-19 at a frequency equal to 1.

In fact, $\bar{L}_{RS}$ is calculated by taking into account the distribution of the natural oscillation frequencies (that is, the analysis is purely structural), but the real oscillation frequencies depend on λ. Although for $\lambda = 0$ two nodes have the same oscillation frequency (the natural one) and thus may form RS links, when $\lambda \neq 0$ the scenario may be different and the nodes can oscillate at different frequencies. This is the reason for which the number of RS links is less or equal to the number of potential RS links. To better illustrate this scenario, we consider the network in Fig. 5.4 with $\omega_2 \simeq \omega_3$, $\omega_4 \simeq \omega_5$ and $\omega_1 \neq \omega_2 \neq \omega_4$. This represents an hypothetical distribution of the oscillation frequencies

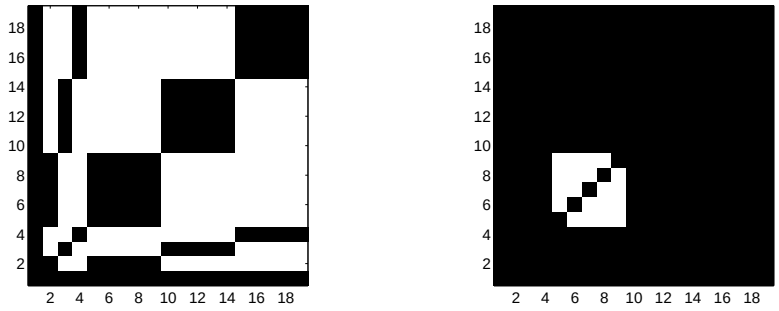

(a) (b)

Fig. 5.3. RS links when node 1 (a) or node 2 (b) of the toy model is attacked. The presence of a RS link between i and j is indicated as a white pixel in the $i-j$ matrix. (a) $\omega_1 = 2.5$, $\omega_i = 1 \pm 5\%$ $\forall i = 2, \ldots, 19$, $\lambda = 1$; (b) $\omega_2 = 2.5$ and $\omega_i = 1 \pm 5\%$ for $i = \{1, 3, \ldots, 19\}$, $\lambda = 0.6$.

due to a non zero coupling, in which two pairs of nodes with similar frequencies have been formed. In this condition only two RS links may form between the nodes at the same frequency, while nodes 2 and 4, for instance, cannot be remotely linked since they are at a different frequency. Furthermore, the two heterogeneous paths connecting the nodes at the same frequency pass through the same node 1. Compared to the case in which all the peripheral nodes have the same frequencies and the information to be transmitted to synchronize them is unique, here the two RS links require that node 1 is able to transmit two different information. If this is not the case, it may happen that only one RS link forms. In fact, Fig. 5.5 shows one example in which two RS links do form (Fig. 5.5(a)) and one example in which only one RS

link does (Fig. 5.5(b)). The two examples shown in Fig. 5.5 differ for the distribution of the natural frequencies.

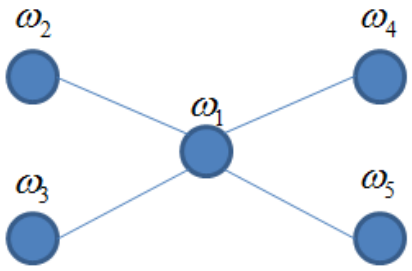

Fig. 5.4. A network of $N = 5$ nodes with $\omega_2 \simeq \omega_3$, $\omega_4 \simeq \omega_5$ and $\omega_1 \neq \omega_2 \neq \omega_4$.

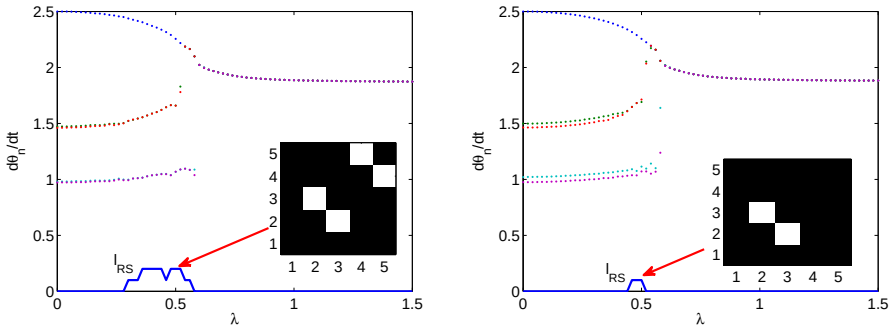

Fig. 5.5. Node oscillation frequencies vs. λ for a network of $N = 5$ nodes with: (a) $\omega_1 = 2.5$, $\omega_2 = 1.472$, $\omega_3 = 1.461$,$\omega_4 = 0.981$,$\omega_5 = 0.972$; (b) $\omega_1 = 2.5$, $\omega_2 = 1.498$, $\omega_3 = 1.463$,$\omega_4 = 1.021$,$\omega_5 = 0.975$. The inset shows the RS links appearing for $\lambda = 0.5$.

We now discuss the more general case of ER and SF networks. Fig. 5.6(a) shows the evolution of L_{RS} and $\bar{L}_{RS}$ for an increasing fraction f of attacked nodes. Nodes are attacked according to their value

of betweenness centrality. For low values of f, due to the presence of many hubs in SF networks, the number of potential RS links is greater in SF than in ER. For high values of f the two types of networks show a similar behavior in terms of $\bar{L}_{RS}$, since, once a large fraction of nodes has been attacked, the structural differences between SF and ER become smaller. Furthermore, for SF networks the peak of $\bar{L}_{RS}$ occurs for a lower value of f with respect to ER networks: this resembles what is observed in [65] where it is shown that the diameter of SF networks increases more rapidly than ER networks and the network breaks into many isolated fragments, when the most connected nodes are removed.

In terms of L_{RS}, for both types of networks, as expected from the analysis of the toy model, we found that $L_{RS} < \bar{L}_{RS}$. The values of f for which the peak of L_{RS} occurs are in good agreement with those corresponding to the peak of $\bar{L}_{RS}$. As for $\bar{L}_{RS}$, the peak of L_{RS} occurs first for SF networks. In SF networks the number of heterogeneous paths that do form is larger than in ER networks (as the evolution of $\bar{L}_{RS}$ shows), but in these networks (having more hubs) the same node is shared by more heterogeneous paths than in ER networks, a mechanism that reduces the differences in the maximum of L_{RS} in the two types of networks.

For comparison, we show in Fig. 5.6(b) the result of a random selection of the attacked nodes. The strategy used for node selection leads to the same behavior for both networks and to a much lower level of RS than in the case of attacks based on betweenness centrality. In fact, attacking the nodes according to their betweenness centrality allows

to create more heterogeneous paths than attacking randomly chosen nodes. When a node is attacked, the network is subjected to structural changes which depend on both the topology of the network and the node properties.

The analysis carried out shows an analogy with the error and attack tolerance properties investigated in [65]. In fact, removing a node from a network breaks all the paths passing through it. Similarly, changing the natural frequency of a node breaks all the homogeneous paths passing through it and may fragment the network into clusters of nodes having the same oscillation frequency. The number of clusters and their size are affected by the initial topology of the network and by the choice of the node removed/attacked: since RS is favored by the presence of heterogeneous paths, a higher level of RS is observed when the attack is targeted to most connected nodes and for SF network the fraction of nodes to be attacked is smaller than in ER networks.

The analysis discussed refers to a specific value of λ. The behavior with respect to λ has been investigated by repeating the analysis at different values of the coupling parameter. So, for each value of λ an increasing fraction of nodes is attacked and L_{RS} is monitored. The bidimensional diagram of L_{RS} with respect to λ and f is shown in Fig. 5.7 for an attack strategy based on node betweenness and in Fig. 5.8 for an attack strategy based on a random selection of nodes. As expected for random attacks L_{RS} is smaller than for betweenness based attacks. Furthermore, in the case of random attacks the differences between SF and ER networks are almost negligible. The curves shown in Fig. 5.6(a)

(Fig. 5.6(b)) corresponds to the value of λ maximizing L_{RS} in Fig. 5.7 (Fig. 5.8).

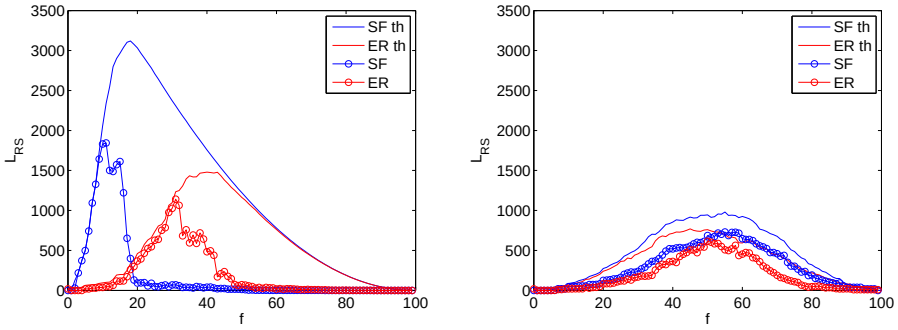

Fig. 5.6. L_{RS} (circles) and $\bar{L}_{RS}$ (solid lines) vs. f for SF and ER networks for $\lambda = 0.9$. Results are averages of 10 networks. (a) Target attack. (b) Random attack.

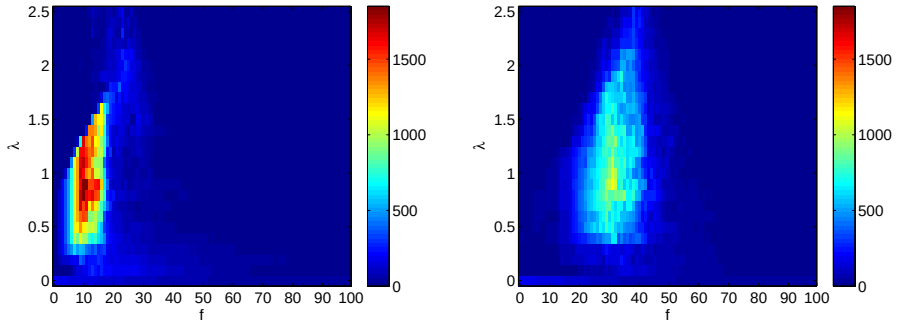

Fig. 5.7. Target attack: behavior of L_{RS} as a function of λ and f for (a) SF networks and (b) ER networks. Results are averages of 10 networks.

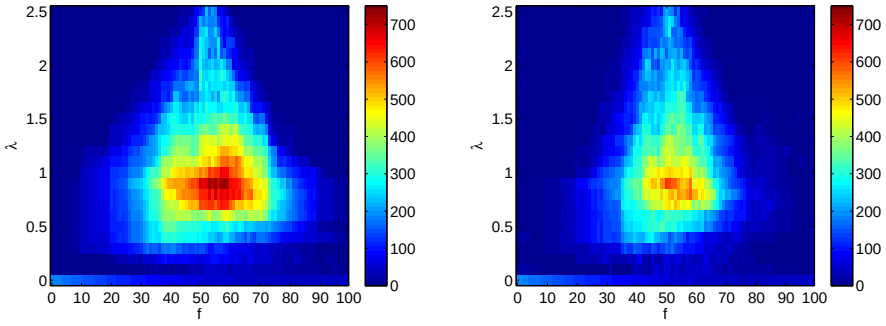

Fig. 5.8. Random attack: behavior of L_{RS} as a function of λ and f for (a) SF networks and (b) ER networks. Results are averages of 10 networks.

5.2 Networks with arbitrary frequency distribution

In this Section we show that RS is not limited to networks with bimodal distribution, but also occurs when other frequency distributions are used. The condition for the appearance of RS in a more general framework is the extension of the considerations analyzed in Sec. 5.1 for networks with bimodal distributions. Arbitrary frequency distributions may be considered provided that they allow the formation of heterogeneous paths between network nodes. In particular, we have considered i) networks with a correlation between frequencies and node degrees, and ii) networks with a correlation between frequencies and link weights. For the first case we have considered two different frameworks: networks where, fixed the structure, the oscillator natural frequencies are set according to their degree; and networks where a spontaneous frequency-degree correlation is the result of the network construction process, that is, frequency gap-conditioned (FGC) random networks.

In the second case, fixed a distribution of the frequency, we consider weighted networks where the link weight is proportional to the oscillator natural frequency.

5.2.1 Frequency-degree correlated networks

Frequency-degree correlated networks have been constructed starting from a given topology and then assigning the oscillator natural frequency on the basis of the network degree distribution, that is:

$$\omega_i = k_i(1 + \xi_i) \tag{5.1}$$

where $i = 1, \ldots, N$ and ξ_i is a random variable uniformly distributed between -0.025 and 0.025, introduced to generate for each set of nodes having the same degree an uniform distribution of natural oscillation frequencies centered around the node degree itself. We have considered both SF and ER networks with $N = 100$ nodes and reported in Fig. 5.9 the parameters n_{RS} and L_{RS}. In particular, Figs. 5.9(a) and 5.9(b) refer to SF networks, while Figs. 5.9(c) and 5.9(d) to ER networks. The results show that the level of RS is larger in case of SF networks, while the level is very low for ER networks.

5.2.2 FGC random networks

FGC random networks [66] are built with the following algorithm: given N oscillators, the natural frequencies ω_i are chosen from a given distribution $p(\omega)$ (random uniform distribution in the interval $[1, 2]$). Links

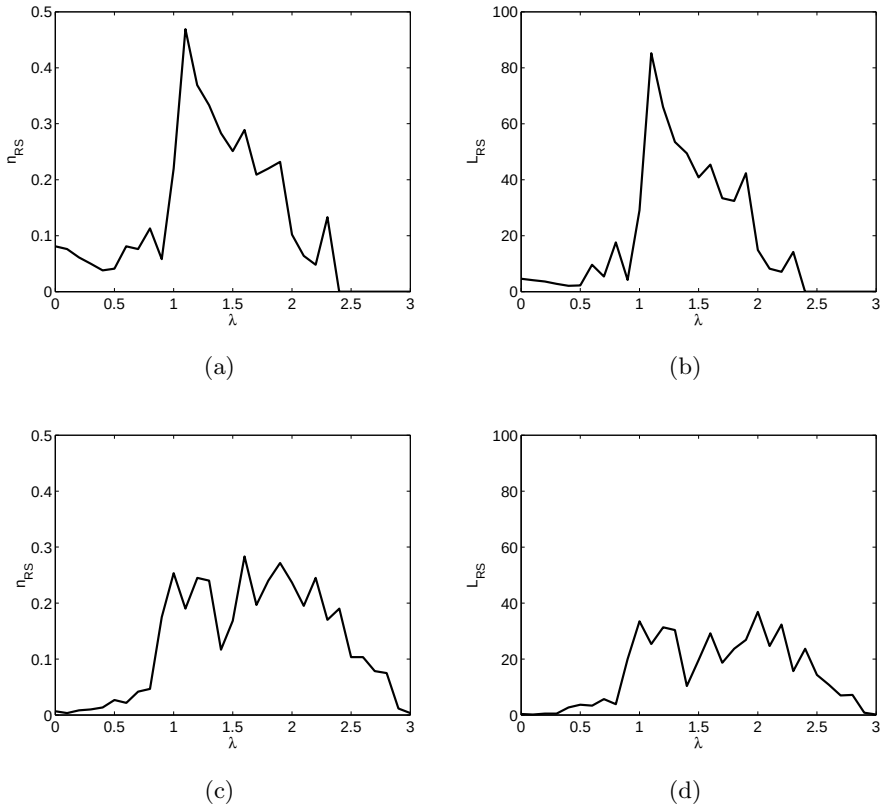

Fig. 5.9. Remote synchronization in frequency-degree correlated networks: (a) n_{RS} for SF networks; (b) L_{RS} for SF networks; (c) n_{RS} for ER networks; (d) L_{RS} for ER networks. Results are averages of 5 networks, each for 5 different distributions of frequencies.

are established in an iterative way until the desired number of links L is reached, by randomly picking a pair (i, j) of oscillators, and checking if $|\omega_i - \omega_j| > \gamma$, where γ is the gap. The procedure may eventually lead to disconnected networks, that are discarded. The resulting network has an ER topology with an average degree $< k >= \frac{2L}{N}$.

To investigate remote synchronization in FGC random networks, we generated three different sets of networks, each one formed by 20

networks with a fixed value of γ ($\gamma = 0$, $\gamma = 0.2$ and $\gamma = 0.4$), and monitored the parameters n_{RS} and L_{RS}.

The three case studies allows to compare networks where a frequency-degree correlation is established with those where the frequency of a node does not depend on the degree. In fact, according to the algorithm used for the network construction, a correlation is established only when $\gamma = 0.4$. This is shown in Fig. 5.10 where the node frequency vs. the node degree is reported for three networks corresponding to the cases of $\gamma = 0$ (Fig. 5.10(a)); $\gamma = 0.2$ (Fig. 5.10(b)) and $\gamma = 0.4$ (Fig. 5.10(c)).

The parameters n_{RS} and L_{RS} are reported in Fig. 5.11. Remote synchronization appears for the set of networks generated with $\gamma = 0.4$, that is, networks with a frequency-degree correlation induced by an high value of γ ($\gamma = 0.4$). On the contrary, in networks generated with $\gamma = 0$ or $\gamma = 0.2$ the degree is not correlated with the frequency and remote synchronization does not appear. In fact, for such networks both the parameters n_{RS} (Fig. 5.11(a)) and L_{RS} (Fig. 5.11(b)) are significantly lower than in the case of $\gamma = 0.4$.

5.2.3 Frequency-weighted networks

In the previous Sections we have shown that remote synchronization can occurs in different ways by changing the distribution of the natural frequencies of the oscillators. Also in the case investigated here, a correlation between the natural frequency and a structural property of the network is considered, but the new settling differs for the structural

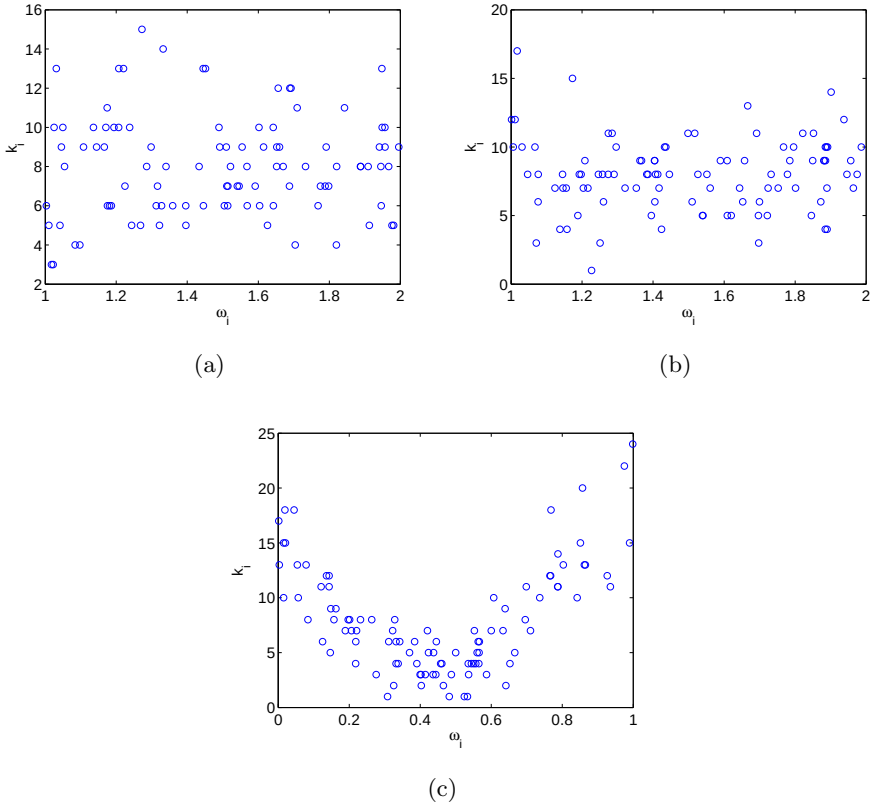

Fig. 5.10. Correlation between frequency and degree in a FGC network with $N = 100$ nodes for: (a) $\gamma = 0$; (b) $\gamma = 0.2$; (c) $\gamma = 0.4$.

property considered. Here, weighted networks, where the link weights are proportional to the absolute value of the natural frequency of the oscillators, are taken into account. The model is the following:

$$\begin{aligned} \dot{x}_i &= (\alpha - x_i^2 - y_i^2)x_i - \omega_i y_i + \tfrac{\lambda}{k_i}|\omega_i| \textstyle\sum_{j=1}^{N} a_{ij}(x_j - x_i) \\ \dot{y}_i &= \omega_i x_i + (\alpha - x_i^2 - y_i^2)y_i + \tfrac{\lambda}{k_i}|\omega_i| \textstyle\sum_{j=1}^{N} a_{ij}(y_j - y_i) \end{aligned} \tag{5.2}$$

This framework was used to demonstrate the onset of explosive synchronization in general complex networks [67]. Following the approach

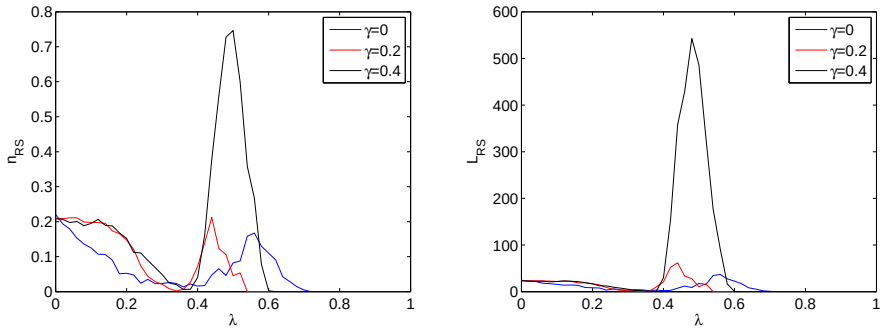

(a) (b)

Fig. 5.11. Remote synchronization in FGC networks with $N = 100$ nodes: (a) n_{RS}; (b) L_{RS}. Remote synchronization appears for networks generated with $\gamma = 0.4$. Results are averages of 20 networks.

proposed in [67], we start from a symmetric distribution of the natural frequencies, where, in particular, the frequencies are chosen from a Gaussian distribution with mean $\mu = 0$ and variance $\sigma^2 = 1$. In our analysis we consider the case of SF and ER networks of Stuart-Landau (SL) oscillators, including the limit case of $\alpha \to \infty$, for which, as discussed in Chapter 4, we recover the model of Kuramoto oscillators. The evaluation of the two order parameters n_{RS} and L_{RS}, that is, the fraction of remotely synchronized nodes and the number of links between remotely synchronized nodes, shows the appearance of remote synchronization for $\alpha = 1$ (SL oscillators), which however disappear when $\alpha \to \infty$ (Kuramoto oscillators). In this latter case, a first-order phase transition has been found, so that we have also computed forward and backward continuation in λ of the Kuramoto order parameter (Eq. 4.9).

We have simulated SF and ER networks with $N = 500$ nodes and different values of the average degree (ranging from $\langle k \rangle = 2$ to $\langle k \rangle = N-1$, that is the case of all-to-all networks). In Fig. 5.12 we report the results for the SF (upper panels) and ER (bottom panels) networks of SL oscillators with $\langle k \rangle = 4$, $\langle k \rangle = 8$ and $\langle k \rangle = 32$. Figs. 5.12(a) and 5.12(c) show the behavior of the n_{RS}, while Figs. 5.12(b) and 5.12(d) the behavior of L_{RS}. Remote synchronization is observed for low values of $\langle k \rangle$, while it progressively disappears when $\langle k \rangle$ increases as the number of homogeneous paths does. Remote synchronization clearly also disappears when $\alpha \to \infty$ as the amplitude is no more a free parameter.

The analysis of the Kuramoto order parameter reveals different transitions for SL or Kuramoto oscillators. For $\alpha = 1$ the transition is second-order, for $\alpha \to \infty$ the type of transition depends on $\langle k \rangle$. For low values of $\langle k \rangle$ a second-order transition has been observed, while for greater values of $\langle k \rangle$ the transition becomes first-order. This is shown in Fig. 5.13, where the synchronization diagram is reported.

The same model (Eqs. 5.2) shows both remote and explosive synchronization. The two phenomena appear in different region of the parameter space: remote synchronization is found for low $\langle k \rangle$ and α (it gradually decreases when $\langle k \rangle$ increases as shown in Fig. 5.14), while a sharp transition (signature of explosive synchronization) appears for large α with an hysteresis area increasing with $\langle k \rangle$ (Fig. 5.14).

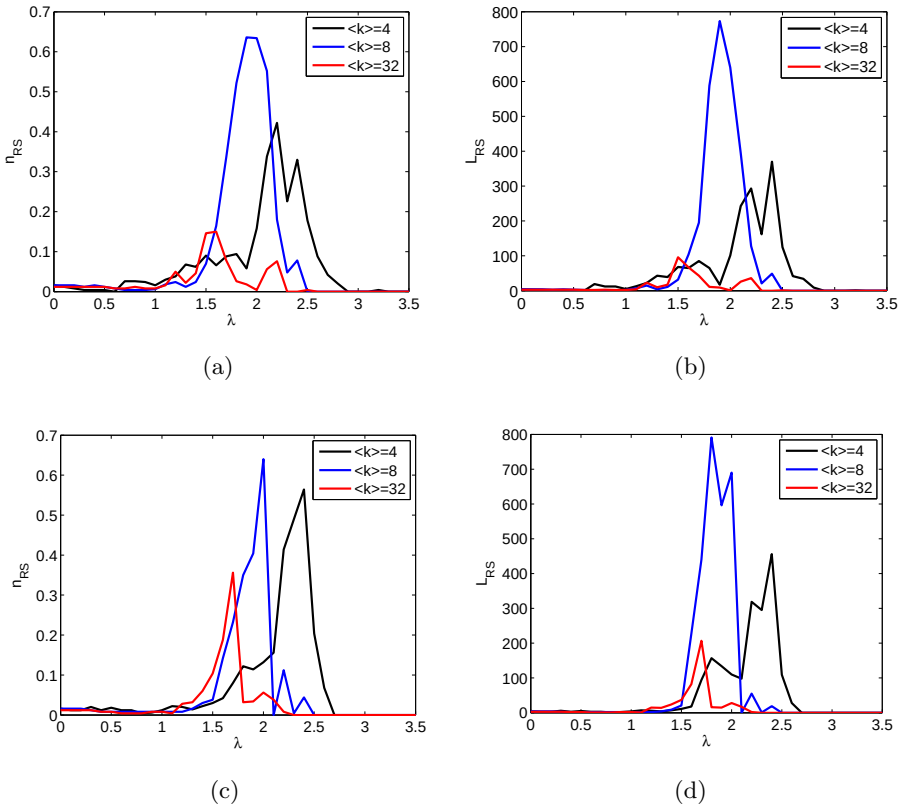

Fig. 5.12. Remote synchronization in a frequency-weighted network of SL oscillators with $\langle k\rangle = 4$, $\langle k\rangle = 8$ and $\langle k\rangle = 32$: (a) n_{RS} and (b) L_{RS} for SF networks; (c) n_{RS} and (d) L_{RS} for ER networks. Results are averages of 5 different distributions of frequencies.

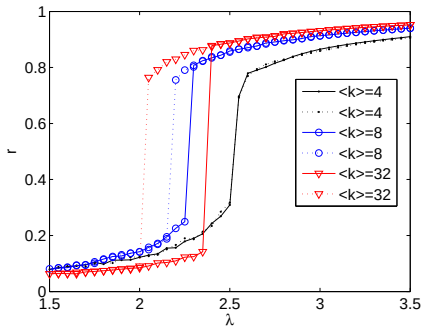

Fig. 5.13. Forward and backward continuation in λ for the Kuramoto order parameter r in networks of Kuramoto oscillators for different values of $\langle k \rangle$. The transition is second-order for $\langle k \rangle = 4$, while first-order for greater values of $\langle k \rangle$.

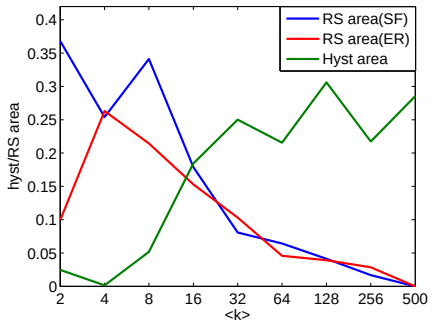

Fig. 5.14. Hysteresis area for networks of Kuramoto oscillators and area underlying n_{RS} for networks of SL oscillators vs. $\langle k \rangle$.

Part III

Memristors in complex networks

6

The memristor as a synapse for complex networks

In this Chapter we show the use of memristors as a synapse in a complex network of chaotic circuits. The memristors allows to implement an adaptive law driving the network towards synchronization. At the same time, the complexity of the implementation at the circuit level is kept very low, as only two memristors are needed to implement the adaptive law.

6.1 The memristor as a synapse

An application of memristors that has gained increasing attention is their use as synapse in artificial neural networks for neuromorphic processing. Due to their intrinsic properties, memristors can be viewed as resistors in which the internal conductance is modulated by an external signal with the possibility to remember the previous state. This behavior is closely related to the functionality of the synapses, in fact the synaptic weight modulates how signals are transmitted between neurons and is adjusted by the ionic flow through the synapse.

The most difficult step in the implementation of artificial neural networks is the realization of synapses, which often require a large number of transistors. In fact, while there are several realizations of a electronic neurons, synapses are not simple to realize in nanoscale dimensions. For this reason, the recent demonstration of the memory effect in memristors suggested a possible realization of synapses with low power consumption and small size, thereby the idea to implement a neuromorphic chip with dimensions comparable to the one of the human brain. An example of an experimental implementation of synaptic functions in nanoscale silicon-based memristors has been proposed in [68], where, in particular, the focus is on the possibility of implementing the synaptic time dependent plasticity with a particular circuit in which the synapses are realized with a nanoscale memristor.

Further exploiting the analogy within a memristor and a synapse led Pershin and coauthors to formulate a model of amoeba learning based on a memristor [69]. The electronic circuit proposed in [69] is made only of passive components, where biological oscillations are simulated with a LC circuit, the dissipation inside the amoeba is represented by a resistor R, and the mechanism of memory is recovered by using a voltage controlled memristor. Other examples of bio-inspired networks coupled with a memristor are reported in [70],[71], where the dynamic behavior and the synchronization properties of two FitzHugh-Nagumo and two Hindmarsh-Rose neurons are studied. The main findings of these works is that memristor dynamics influences the behavior of the networks and the memristor ability to model the plasticity of a biological synapse.

In this Chapter we explore the idea of using memristors as a synapse in a complex network to take advantage of the dynamics introduced by them. In fact, recently new adaptive strategies for network synchronization have been proposed. According to these strategies, and in particular to those *edge-based* [72], each pair of coupled oscillators negotiates the strength of their mutual coupling which is now a time-dependent variable. If the dynamics of the coupling is made dependent on the difference between the states of the coupled oscillators, synchronization emerges as the result of an adaptive process of the network. In this Chapter we show that this strategy can be implemented at the circuit level with a pair of HP memristors connected in antiparallel.

6.2 Coupling a pair of nonlinear circuits with memristors

In this Section we study the dynamic behavior of a pair of Chua's oscillators coupled through the configuration, already discussed in Chapter 2, consisting of two HP memristors in antiparallel. Memristors are simulated according to Eqs. (1.7), (1.9) and a Biolek's window (1.14) with $p = 1$.

We first consider a pair of Chua's circuits coupled as in Fig. 6.1. In terms of dimensionless equations the circuit is described by the following equations:

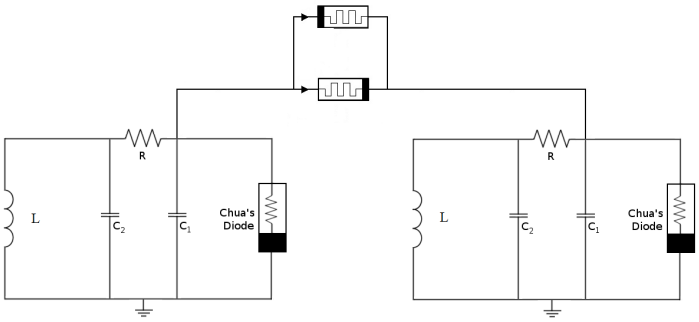

Fig. 6.1. Scheme of two Chua's circuits coupled through two memristors in antiparallel.

$$\begin{cases} \dot{x}_{1,1} = \tau(\alpha_C x_{1,2} - \alpha_C h(x_{1,1}) + k(x_{2,1} - x_{1,1})(1/\bar{M}_{12} + 1/\bar{M}_{21})) \\ \dot{x}_{1,2} = \tau(x_{1,1} - x_{1,2} + x_{1,3}) \\ \dot{x}_{1,3} = \tau(-\beta_C x_{1,2}) \\ \dot{x}_{2,1} = \tau(\alpha_C x_{2,2} - \alpha_C h(x_{2,1}) + k(x_{1,1} - x_{2,1})(1/\bar{M}_{21} + 1/\bar{M}_{12})) \\ \dot{x}_{2,2} = \tau(x_{2,1} - x_{2,2} + x_{2,3}) \\ \dot{x}_{2,3} = \tau(-\beta_C x_{2,2}) \end{cases} \tag{6.1}$$

where we have labelled the state variables of the first circuits as $x_{1,1}$, $x_{1,2}$, and $x_{1,3}$, and, analogously those of the second circuit as $x_{2,1}$, $x_{2,2}$, and $x_{2,3}$. The nonlinearity is $h(x_{i,1}) = (m_1+1)x_{i,1}+0.5(m_0-m_1)(|x_{i,1}+1|-|x_{i,1}-1|)$ with $i = \{1, 2\}$. The memristances have been indicated as M_{12} (the memristor with $\eta = 1$) and M_{21} (the memristor with $\eta = -1$) and with w_{12} and w_{21} the corresponding memristor internal variables, governed by

$$\begin{aligned} \dot{\bar{w}}_{12}(t) &= F(\bar{w}_{12}(t), i_{12}(t))i_{12}(t) \\ \dot{\bar{w}}_{21}(t) &= F(\bar{w}_{21}(t), i_{21}(t))i_{21}(t) \end{aligned} \tag{6.2}$$

with $i_{12}(t) = \frac{x_{2,1}-x_{1,1}}{M_{12}}$ and $i_{21}(t) = \frac{x_{1,1}-x_{2,1}}{M_{21}}$. In Eqs. (6.1) we have introduced a parameter τ, scaling the time unit of the Chua's circuit in order to perform an analysis taking into account that memristors and Chua's circuit may have different time scales. More in detail, we investigate the system behavior with respect to the parameters k, that is, the coupling coefficient, and τ, by monitoring two parameters. The first is the synchronization error defined as:

$$E = \langle \left(\sum_{h=1}^{3} (x_{2,h} - x_{1,h})^2 \right)^{\frac{1}{2}} \rangle_t \tag{6.3}$$

The second parameter is

$$\sigma_T^2 = \sigma^2[w_{12}] + \sigma^2[w_{21}] \tag{6.4}$$

where $\sigma^2[w_{ij}]$ is the variance of w_{ij}. σ_T^2 allows to track the changes in w_{12} and w_{21}, thus monitoring when the internal variables do oscillate or reach a steady-state. The bifurcation diagram is shown in Fig. 6.2, where we show the behavior of the synchronization error and the total variance of the memristor variables.

In Fig. 6.2(a) the white region represents the region of unstability of the Chua's circuit, while the blue one synchronization of the network. When τ increases, synchronization becomes more difficult to achieve as it requires larger values of k. Fig. 6.2(b) shows how the total variance of the memristor variables depends on τ and k. From the bifurcation diagram it appears that the configuration proposed may be used to implement an adaptive law for the coupling weights so that the val-

ues of the coupling leading to synchronization can be obtained in an automatic way.

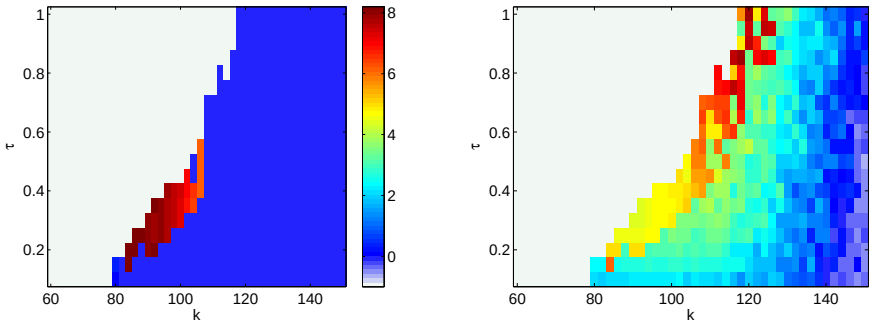

(a) (b)

Fig. 6.2. Bifurcation diagram with respect to k and τ for a system of two coupled Chua's circuits: (a) synchronization error; (b) total variance of the memristor variables.

6.3 Memristor-based synapses in a complex network of Chua's circuits

In this Section we investigate the use of the synapse introduced above in a complex network. The model consists of a network of N Chua's circuits coupled through pairs of memristors. Each pair of Chua's circuits i and j is connected by two memristors with opposite polarity (Fig. 6.1), so that in the network there are $N(N-1)$ memristors. We indicate the state variables of the memristors connecting node i and j as w_{ij} and w_{ji} and the corresponding memristances as $M_{ij} = M(w_{ij})$ and $M_{ji} = M(w_{ji})$.

The dimensionless equations of the network are:

$$\begin{cases} \dot{x}_{i,1} = \tau(\alpha_C x_{i,2} - \alpha_C h(x_{i,1}) + k \sum_{j=1}^{N} (x_{j,1} - x_{i,1})(1/\bar{M}_{ij} + 1/\bar{M}_{ji})) \\ \dot{x}_{i,2} = \tau(x_{i,1} - x_{i,2} + x_{i,3}) \\ \dot{x}_{i,3} = \tau(-\beta_C x_{i,2}) \end{cases} \tag{6.5}$$

for $i = 1, \ldots, N$, and

$$\dot{\bar{w}}_{ij}(t) = F(\bar{w}_{ij}(t), i_{ij}(t)) i_{ij}(t) \tag{6.6}$$

with $i_{ij}(t) = \frac{x_{j,1} - x_{i,1}}{M_{ij}}$.

Numerical results refer to a network of $N = 4$ Chua's circuits. Initial conditions are fixed in a random way for the state variables of the Chua's circuits. Zero initial conditions are assumed for the memristor variables $w_{i,j}$. For $k = 0$ the circuits are uncoupled and thus not synchronized; the memristor variables oscillate between their extreme values, 0 and 1 (Fig. 6.3). For a sufficiently high value of k the Chua's circuits are synchronized; correspondingly, the memristor variables converge to a stationary steady-state (Fig. 6.4, $k = 70$). The steady-state depends on the value of k: the larger the value of k the smaller is the excursion of the memristor variables. For small coupling, the network is not able to synchronize; in particular, the Chua's circuits become unstable.

The results suggest the possibility to use a pair of memristors to implement a synapse with adaptive capabilities. In fact, the memristors provide a dynamics in the link weight which, in pair of oscillators, can

drive the link towards a value leading to the synchronization and, in a network, to a structure supporting synchronization.

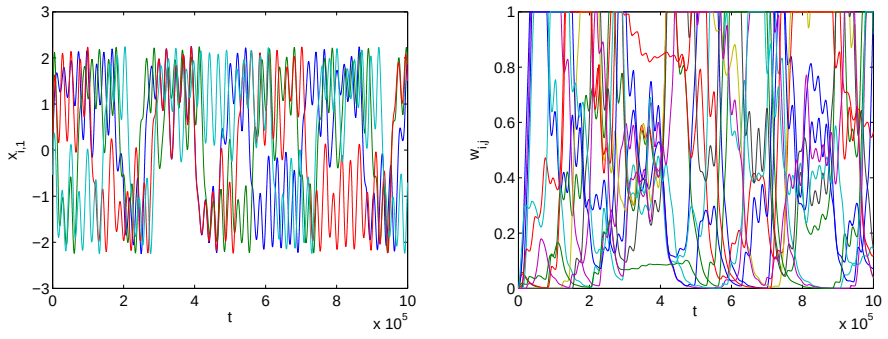

(a) (b)

Fig. 6.3. Behavior of four Chua's circuits coupled through memristors for $k = 0$ and $\tau = 0.1$: (a) waveforms of the state variables $x_{i,1}$; (b) trend of memristor variables $w_{i,j}$.

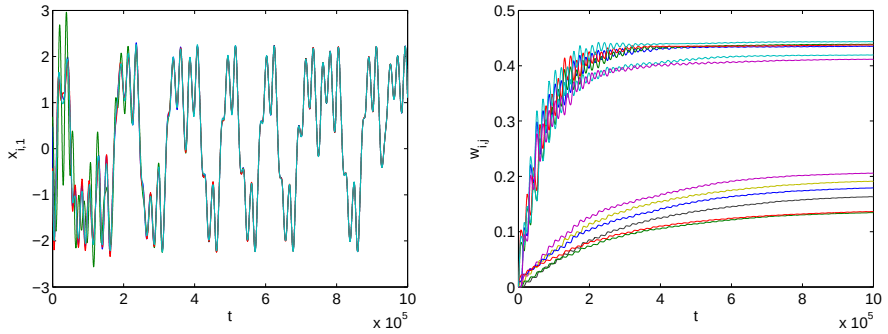

(a) (b)

Fig. 6.4. Behavior of four Chua's circuits coupled through memristors for $k = 70$ and $\tau = 0.1$: (a) waveforms of the state variables $x_{i,1}$; (b) trend of memristors variables $w_{i,j}$.

7

Concluding remarks

This thesis dealt with two aspects of complexity, the dynamics of a single unit of a complex network and the interaction among the units. In particular, our attention focused on the study of the memristor, a new component able to act as the only nonlinearity of a chaotic circuit and as connection between two nodes in a network. The memristor, described by the so-called nonlinear ionic drift model, has been analyzed from the theoretical point of view for the implementation of a gallery of circuits, able to show chaos, based on it. The analysis led to the conclusion that a suitable configuration for chaotic circuit design is the antiparallel connection of two memristors. This configuration was used to derive a series of autonomous and non-autonomous circuits with a rich dynamical repertoire, including limit cycles of different periods, chaotic orbits, multistability and different bifurcation scenarios. To fill the gap, still existing between theoretical approaches and experimental ones in the research on chaotic circuits based on memristors, an analysis of memristor devices from a more practical point of view has been also carried on two different types of memristors. We have shown that

the use of different materials and of different fabrication techniques in the realization of memristor reveals different properties and behavior of the device. On the one hand, this opens the possibility of using the memristor in various ways, and on the other hand this may require the development of compact models for the specific device and application. One possible approach that has been explored is the use of artificial neural networks. Based on the result of the experimental analysis and on the actual performance of the examined devices, a hybrid approach towards the design of chaotic circuits based on memristors was envisaged.

In the second part of this PhD thesis the study of the phenomenon of the so-called remote synchronization in a complex network has been carried out. After the analysis of remote synchronization in general complex networks, the mechanism underlying this phenomenon has been taken into account, revealing that different settlings, such as bimodal distributions of natural frequencies, frequency-degree correlations or frequency-weighted structures, may be used to induce or enforce remote synchronization in complex networks. Furthermore, it was found that, under certain conditions, the network of Stuart Landau oscillators investigated becomes a network of Kuramoto purely phase oscillators, where the remote synchronization vanishes and is replaced by another type of synchronization, characterized by an abrupt transition to synchronization.

The last part of the thesis aimed at exploring the idea to use the memristor as the link in a complex network, by using its properties of

nonlinear and memory element. Also in this case, the key configuration is provided by the antiparallel connection of two memristors. A synapse made in this way implements a dynamics in the link weight which, starting from a configuration where synchronization is not possible, is able to reconfigure the link weights in such a way that synchronization is obtained.

8

Acknowledgements

"a piece of infinity
is still infinity"

Part of the research presented in this thesis has been carried out in collaboration with Faculty of Technical Sciences of Novi Sad, under supervision of Prof. Goran Stojanovic, and with the Departamento de Fisica de la Materia Condensada at the University of Zaragoza, Spain, under supervision of Prof. Jesus Gomez-Gardenes. The results obtained on drop coated memristors have been possible thanks to the collaboration of Dr. Ella Gale and Prof. Andrew Adamatzky at University of West England, Bristol.

I would like to thank Prof. Luigi Fortuna for his support during these three years and for the opportunity he gave to me.

I want also thank Prof. Salvatore Graziani, for the fruitful discussions.

I thank Dr. Arturo Buscarino, for his support and help, he was for me a colleague and a real friend.

I want to thank Prof. Mattia Frasca, my tutor, for his guidance throughout the period of my PhD studies, his expertise was essential for the realization of all my works.

At the end a special thanks goes to my family and to Vittorio, for their support and constant love.

Publications

Journal publications

1. L. V. Gambuzza, A. Cardillo, A. Fiasconaro, L. Fortuna, J. Gomez-Gardenes, M. Frasca, "Analysis of Remote Synchronization in Complex Networks", *Chaos*, vol. 23, 043103 (2013).
2. A. Buscarino, L. V. Gambuzza, M. Porfiri, L. Fortuna, M. Frasca, "Robustness to noise in synchronization of complex networks", *Scientific Reports*, vol. 3, no. 2026 (2013).
3. A. Buscarino, L. Fortuna, M. Frasca, L. V. Gambuzza, "A gallery of chaotic oscillators based on HP memristor", *Int. Journal of Bif. and Chaos*, vol.23, no.5, pp.1330015-1-1330015-14 (2012).
4. A. Buscarino, L. Fortuna, M. Frasca, L. V. Gambuzza, "A chaotic circuit based on HP memristor", *Chaos*, vol. 22, 023136 (2012).
5. S. Bouali, A. Buscarino, L. Fortuna, M. Frasca, L. V. Gambuzza, "Emulating Complex Business Cycles by an Electronic Analog", *Nonlinear analysis: real world applications*, vol. 13, no. 6, pp. 2459-2465 (2012).

6. A. Buscarino, L. Fortuna, M. Frasca, L. V. Gambuzza, G. Sciuto, "Memristive Chaotic Circuits Based On Cellular Nonlinear Networks", *Int. Journal of Bif. and Chaos*, vol. 22, no. 3 (2012).
7. L. Fortuna, M. Frasca, L. V. Gambuzza, A. Sarra Fiore, R.S. Ali, M.T. Rashid,"Analysis of the determinism of time-series extracted from social and biological systems", *Iraqi Journal of Electrical and Electronic Engineering*, vol. 6, no. 2, pp. 180–185, (2010).

Conference publications

1. L. V. Gambuzza, N. Samardzic, S. Dautovic, M. G. Xibilia, S. Graziani, L. Fortuna, G. Stojanovic, M. Frasca, "A data driven model of TiO2 printed memristors", eleco (2013).
2. A. Buscarino, L. Fortuna, M. Frasca, L. V. Gambuzza, "A new driven memristive chaotic circuit", ECCTD 2013.
3. A. Buscarino, S. Dautovic, L. Fortuna, M. Frasca, L. V. Gambuzza, "Towards printed chaotic circuits: a topology based on memristors, *IX Symposium Industrial Electronics INDEL 2012*, Banja Luka, November 01-0.3,2012, pp. 299-302
4. A. Buscarino, L. Fortuna, M. Frasca, L. V. Gambuzza, T. V. Pham, "Chaos control in a chaotic system with only one stable equilibrium point", *AIP Conf. Proc.* 1479, 691 (2012).
5. S. Bouali, A. Buscarino, L. Fortuna, M. Frasca, and L. V. Gambuzza, "A Chaotic Circuit Based on Boualis Equations", *AIP Conf. Proc.* 1389, 1035 (2011).

6. L. Fortuna, M. Frasca, L. V. Gambuzza, "Organic chaotic circuits for traceability", *16th International Symposium on Power Electronics (Ee2011)*, Novi Sad, Serbia, October 26-28, 2011, SpS-2.6, pp. 1-4.
7. A. Buscarino, L. Fortuna, M. Frasca, L. V. Gambuzza, G. Sciuto, "A new cellular nonlinear network-based memristive chaotic circuit", *IEEE Proceedings of International Symposium on Signals, Circuits and Systems (ISSCS 2011)*, Iasi, Romania, June 30-July 1, 2011, 73-76, 2011.
8. M. Frasca, L. V. Gambuzza, L. Fortuna, S. Boccaletti, "Experimental observations of synchronization interfaces in networks of oscillators", *IEEE Proceedings of International Symposium on Signals, Circuits and Systems (ISSCS 2011)*, Iasi, Romania, June 30-July 1, 2011, 69-72, 2011.
9. Fortuna L, Frasca M., L. V. Gambuzza, A. Sarra Fiore, R.S. Ali, M. T. Rashid, "Analysis of the determinism of time-series extracted from social and biological systems", *1st International Conference on Energy, Power and Control EPC-IQ'01*, Basra, Iraq, 30 Novembre - 2 Dicembre 2010, PISCATAWAY: IEEE, vol. 1, p. 176-181 2010.

References

1. L. O. Chua, " Memristor-The missing circuit element", *IEEE Trans. Circuit Theory*, Vol. 18, pp. 507–519 (1971).
2. L. O. Chua, and S. M. Kang, " Memristor devices and systems", *Proc. IEEE*, Vol. 64, pp. 209–223 (1976).
3. M. Di Ventra, Y. V. Pershin, and L. O. Chua, "Circuit elements with memory: Memristors, memcapacitors, and meminductors", *Proceedings of the IEEE*, Vol. 97(10), pp. 1717–1724 (2009)
4. D. B. Strukov, G. S. Snider, D. R. Stewart, and R. Stanley Williams, " The missing memristor found", *Nature*, Vol. 453, pp. 80–83 (2008).
5. J. J. Yang, M. D. Pickett, X. Li, D. A. A. Ohlberg, D. R. Stewart, and S. Williams, "Memristive switching mechanism for metal/oxide/metal nanodevices",*Nature Nanotechnology* Vol. 3, pp. 429-433 (2008).
6. M. Y. Chan, T. Zhang, V. Ho, and P. S. Lee, "Resistive switching effects of HfO_2 high-k dielectric", *Microelectronic Engineering*, Vol. 85, pp. 2420-2424 (2008).
7. T. H. Kim, E. Y. Jang, N. J. Lee, D. J. Choi, K.-J. Lee, J.-T. Jang, J.-S. Choi, S. H. Moon, and J. Cheon, "Nanoparticle Assemblies as Memristors",*Nano Letters*, Vol. 9, 6, pp. 2229-2233 (2009).
8. K. Nagashima, T. Yanagida, K. Oka, and T. Kawai, "Interfacial effect on metal/oxide nanowire junctions", *Applied Physics Letters*, Vol. 94, pp. 242902 (2009).
9. S. Almeida, B. Aguirre, N. Marquez, J. McClure, and D. Zubia, "Resistive Switching of SnO2 Thin Films on Glass Substrates", *Integrated Ferroelectrics*, pp. 126:117–124 (2011).

10. Y. V. Pershin, and M. Di Ventra, "Spin memory effects in semiconductor spintronics," *Physical Review B*, Vol. 78, pp. 113309–1–4 (2008).
11. X. Wang, Y. Chen, H. Xi, and D. Dimitrov, "Spintronic memristor through spin-torque-induced magnetization motion", *Electron Device Letters*, Vol. 30(3), pp.294–297 (2009).
12. X. Wang, Y. Chen, Y. Gu, and H. Li, "Spintronic memristor temperature sensor", *Electron Device Letters*, Vol. 31(1), pp.20–22 (2010).
13. Y. N. Joglekar, and S. J. Wolf, " The elusive memristor: properties of basic electrical circuits", *European Journal of Physics*, Vol. 30, pp. 661-675 (2009).
14. Z. Biolek, D. Biolek, and V. Biolkova, "SPICE Model of Memristor with Nonlinear Dopant Drift", *Radioengineering*, Vol. 18(2), pp. 210–214 (2009).
15. M. D. Pickett, D. B. Strukov, J. L. Borghetti, J. J. Yang, G. S. Snider, D. R. Stewart, and R. S. Williams "Switching dynamics in titanium dioxide memristive devices" *J. Appl. Phys.*, Vol. 106, pp. 074508-1–6 (2009)
16. J. Simmons, "Generalized formula for the electric tunnel effect between similar elecrodes separated by a thin insulating film" *J. Appl. Phys.*, Vol. 34(6) (1963)
17. E. N. Lorenz, *Deterministic nonperiodic flow*, J. Athmosph. Sc., Vol. 20, pp. 130-141 (1963).
18. M. Fadlallah, G. Billiot, W. Eccleston, D.Barclay, "Unified organic TFT Compact Modeling and Circuit Design for RFID applications", *Solid-State Electron* vol.51, pp. 1047-1051 (2007).
19. L. Fortuna, M. Frasca, and M. G. Xibilia, *Chua's circuit implementations: yesterday, today and tomorrow*, (World Scientific), Singapore (2009).
20. M. Itoh, and L. O. Chua, "Memristor Oscillators," *Int. J. Bif. Chaos*, Vol. 18, pp. 3183–3206 (2008).
21. B. Muthuswamy, and L. O. Chua, "Simplest chaotic circuit," *Int. J. Bif. Chaos*, Vol. 20, pp. 1567–1580 (2010).
22. B. Muthuswamy, "Implementing memristor based chaotic circuits," *Int. J. Bif. Chaos*, Vol. 20, pp. 1335–1350 (2010).
23. Y. V. Pershin, and M. Di Ventra, "Experimental demonstration of associative memory with memristive neural networks," *Neural Networks*, Vol. 23, pp. 881–886 (2010).

24. A. Buscarino, L. Fortuna, M. Frasca, L. V. Gambuzza, G. Sciuto, "Memristive Chaotic Circuits Based On Cellular Nonlinear Networks", *Int. J. Bif. Chaos*, Vol. 22, pp. 1250070–1–13 (2012).
25. O. Morgul, "Wien bridge based RC chaos generator," *Electronics Letters*, Vol. 31, pp. 2058-2059 (1995).
26. K. Murali, M. Lakshmanan, and L. Chua, "The simplest dissipative non-autonomous chaotic circuit", *Express Letters*, Vol. 41(6), pp. 462–463 (1994).
27. D. Wang, H. Zhao, and J. Yu, "Chaos in memristor based Murali-Lakshmanan-Chua circuit", *Int. Conf. on Communications, Circuits and Systems, ICCCAS 2009*, pp. 958–960 (2009).
28. A. Ishaq Ahamed, and M. Lakshmanan, "Nonsmooth Bifurcations, Transient Hyperchaos and Hyperchaotic Beats in a Memristive Murali-Lakshmanan-Chua Circuit", *Int. J. Bif. Chaos*, Vol. 23(6), pp. 1350098 (2013).
29. N. Duraisamy,N. M. Muhammad, Hyung-Chan Kim, Jeong-Dai Jo, and Kyung-Hyun Choi, "Fabrication of TiO2 thin film memristor device using electrohydrodynamicinkjet printing" *Thin Solid Films*, Vol. 520, pp. 50705074 (2012).
30. N. G. Hackett, B. Hamadani, B. Dunlap, J. Suehle, C. Richter, C. Hacker, and D. Gundlach, "A flexible solution-processed memristor," *IEEE Electron Device Lett.*, vol. 30, no. 7, pp. 706708 (2009).
31. K. H. Choi, M. Mustafa, K. Rahman, B. K. Jeong, and Y. H. Doh "Cost-effective fabrication of memristive devices with ZnO thin film using printed electronics technologies" *Applied Phisics A*, Vol. 106(1), pp. 165-170 (2012).
32. F. Miao, W. Yi, I. Goldfarb, J. J. Yang, M. X. Zhang, M. D. Pickett, J. P. Strachan, G. Medeiros-Ribeiro and R. S. Williams, "Continuous Electrical Tuning of the Chemical Composition of TaO_x-Based Memristors," *ACS nano*, Vol. 6(3), pp. 2312-2318 (2012).
33. E. Gale, D. Pearson, S. Kitson, A. Adamatzky, B. de Lacy Costello, "Aluminium electrodes effect the operation of titanium dioxide sol-gel memristors," *arXiv preprint*, arXiv:1106.6293 (2011).
34. O. Kavehei, K. Cho, S. Lee, S. Kim, S. Al-Sarawi, D. Abbott, and K. Eshraghian, "Fabrication and modeling of Ag/TiO2/ITO memristor" *Circuits and Systems (MWSCAS), 2011 IEEE 54th International Midwest Symposium on*, pp. 1–4 (2011).

35. M. Yang, L. Li, S. Zhang, G. Li, H. Zhao, "Preparation, characterization and sensing application of inkjet printed nanostructured TiO_2 photoanode", *Sensor and actuators B*, pp. 622-628 (2010).
36. M. Mionic, N. Samardzic, D. Damnjanovic, S. Dautovic, G. Stojanovic, "Fabrication and characterization of ink-jet printed TiO2 memristors," *in preparation.*
37. L. V. Gambuzza, N. Samardzic, S. Dautovic, M. G. Xibilia, S. Graziani, L. Fortuna, G. Stojanovic, M. Frasca "A data driven model of TiO2 printed memristors" *8th Int. Conf. on Electrical and Electronics Engineering* (2013).
38. E. Gale, R. Mayne, A. Adamatzky, B. de Lacy Costello, "Drop coated titanium dioxide memristors," *Materials Chemistry and Physics*, vol. 13, no. 2, pp. 524–529 (2014).
39. E. Gale, B. de Lacy Costello, A. Adamatzky, "Observation of Spontaneous Bursting Spike Patterns Simple Three Memristor Circuits", *Circuit Theory and Design (ECCTD), 2013 European Conference on*, pp. 1–4 (2013).
40. L. Fortuna, S. Graziani, A. Rizzo, M.G. Xibilia, "Soft Sensors for Monitoring and Control of Industrial Processes", *Springer* (2007).
41. S.H. Strogatz, "From Kuramoto to Crawford: exploring the onset of synchronization in populations of coupled oscillators," *Physica D* , **143**, pp.1-20 (2000).
42. A. Pikovsky, M. Rosenblum, and J. Kurths, "Synchronization: a Universal Concept in Nonlinear Sciences," (Cambridge University Press) (2003).
43. S. Boccaletti, "The Synchronized Dynamics of Complex Systems," (Elsevier) (2008).
44. E. Bullmore, and O. Sporns, "Complex brain networks: graph theoretical analysis of structural and functional systems," *Nature Reviews Neuroscience*, **10**, pp. 186-198 (2009).
45. A. Pluchino, V. Latora, and A. Rapisarda, "Changing opinions in a changing world: a new perspective in sociophysics," *Internat. J. Modern Phys. C* , **16**, pp. 515 (2005).
46. S. H. Strogatz, "Exploring complex networks," *Nature*, **410**, pp. 268-276 (2001)).
47. S. Boccaletti, V. Latora, Y. Moreno, M. Chavez, and D. U. Hwang, "Complex networks: Structure and dynamics," *Phys. Rep.*, **424**, pp. 175-308 (2006).
48. S. N. Dorogovtsev, A. V. Goltsev, and F. F. Mendes, "Critical phenomena in complex networks," *Rev. Mod. Phys.*, **80**, pp. 1275-1335 (2008).
49. Y. Wu, J. Xiao, G. Hu, and M. Zhan, "Synchronizing large number of nonidentical oscillators with small coupling," *Europhysics Letters*, **97**, pp. 40005-1-6 (2012).

50. S. Acharyya, and R. E. Amritkar, "Synchronization of coupled nonidentical dynamical systems," *Europhysics Letters*, **99**, pp. 40005-1-6 (2012).
51. A. Arenas, A. Diaz-Guilera, J. Kurths, Y. Moreno, and C. S. Zhou, "Synchronization in complex networks," *Phys. Rep.* , **469**, pp. 93-153 (2008).
52. Y. Moreno, and A. F. Pacheco, "Synchronization of Kuramoto oscillators in scale-free networks," *Europhysics. Letters* , **68**, pp. 603-609 (2004).
53. A. Arenas, A. Diaz-Guilera, and C. J. Pérez-Vicente, "Synchronization reveals topological scales in complex networks," *Phys. Rev. Lett.*, **96**, pp. 114102-1-4 (2006).
54. J. Gómez-Gardeñes, Y. Moreno, and A. Arenas, "Paths to Synchronization on Complex Networks," *Phys. Rev. Lett.*, **98**, pp. 034101-1-4 (2007).
55. I. Lodato, S. Boccaletti, and V. Latora, "Synchronization properties of network motifs," *Europhys. Lett.*, **78**, pp. 28001-1-5 (2007).
56. J. Gómez-Gardeñes, S. Gómez, A. Arenas, and Y. Moreno, "Explosive Synchronization Transitions in Scale-Free Networks," *Phys. Rev. Lett.*, **106**, pp.128701-1-4 (2011).
57. T. Nishikawa, A. E. Motter, Y. C. Lai, and F. C. Hoppensteadt, "Heterogeneity in oscillator networks: Are smaller worlds easier to synchronize?," *Phys. Rev. Lett.*, **91**, pp. 014101-1-4 (2003).
58. M. Chavez, D. U. Hwang, A. Amann, H. G. E. Hentschel, and S. Boccaletti, "Synchronization is Enhanced in Weighted Complex Networks," *Phys. Rev. Lett.*, **94**, pp. 218701-1-4 (2005).
59. C. Zhou, A. E. Motter, and J. Kurths, "Universality in the Synchronization of Weighted Random Networks," *Phys. Rev. Lett.*, **96**, pp. 034101-1-4 (2006).
60. D. Gfeller, and De Los Rios, "Spectral Coarse Graining and Synchronization in Oscillator Networks," *Phys. Rev. Lett.*, **100**, pp. 174104-1-4 (2008).
61. Y. Kuramoto, "Self-entrainment of a population of coupled nonlinear oscillators," *Lect. Notes in Physics* , **30**, pp. 420-422 (1975).
62. J. A. Acebrón, L. L. Bonilla, C. J. Pérez-Vicente, F. Ritort, and R. Spigler, "The kuramoto model: a simple paradigm for synchronization phenomena," *Rev. Mod. Phys.*, **77**, pp. 137 (2005).
63. A. Bergner, M. Frasca, G. Sciuto, A. Buscarino, E. J. Ngamga, L. Fortuna, and J. Kurths, "Remote synchronization in star networks," *Phys. Rev. E*, **85**, pp.026208-1-7 (2012).

64. J. Gómez-Gardeñes, and Y. Moreno, "From scale-free to Erdos- Renyi networks," *Phys. Rev. E*, **73**, pp. 056124-1-7 (2006).
65. R. Albert, H. Jeong, A. L. Barabási, " Error and attack tolerance of complex networks", *Nature*, Vol. 406, No. 6794, pp. 378–382 (2000).
66. I. Leyva, A. Navas, I. Sendiña-Nadal, J. A. Almendral, J. M. Buldú, M. Zanin, D. Papo, S. Boccaketti, " Explosive transitions to synchronization in networks of phase oscillators", *Sci. Rep.*, Vol. 3 (2013).
67. X. Zhangh, X. Hu, J. Kurths, and Z. Liu, "Explosive synchronization in a general complex network", *Phys. Rev. E*, **88**, pp. 010802-1-5 (2013).
68. S. H. Jo, T. Chang, I. Ebong, B. B. Bhadviya, P. Mazumder, W. Lu, "Nanoscale memristor device as synapse in neuromorphic systems", *Nano letters*, Vol. 10, no. 4, pp. 1297–1301 (2010).
69. Y. V. Pershin, S. La Fontaine, M. Di Ventra, "Memristive model of amoeba learning", *Phys. Rev. E*, **80**, pp. 021926-1-6 (2009).
70. F. Corinto, V. Lanza, A. Ascoli, M. Gilli, "Synchronization in netwoeks of FitzHugh-Nagumo neurons with memristor synapses", *Circuit Theory and Design (ECCTD), 2011 20th European Conference on*, pp. 608-611 (2011).
71. F. Corinto, A. Ascoli, V. Lanza, M. Gilli, "Memristor synaptic dynamics' influence on synchronous behavior of two Hindmarsh-Rose neurons", *Neural Networks (IJCNN), The 2011 International Joint Conference on*, pp. 2403-2408 (2011).
72. P. De Lellis, M. di Bernardo, and F. Garofalo, "Synchronization of complex networks through local adaptive coupling", *Chaos: An Interdisciplinary Journal of Nonlinear Science*, Vol. 18(3), pp. 037110-037110 (2008).